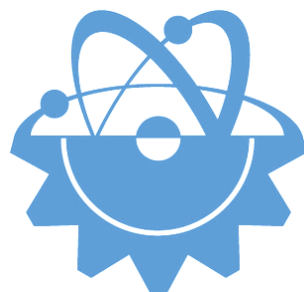


ISSN-Printed: 2536-5010
ISSN-Online: 2536-5134

Volume 9, N 1, 2019

EJT

EUROPEAN JOURNAL OF TECHNIQUE



Copyright © 2017 International Engineering, Science & Education Group

Email (for orders and customer services enquiries): info@ineseg.org, ejt@ineseg.org, ejtineseg@gmail.com

Visit our home page on www.ineseg.org or <https://dergipark.org.tr/ejt>

All Rights Reserved. No part of this publication may be reproduced, stored in a retrieval system or transmitted in any form or by any means, electronic, mechanical, photocopying, recording, scanning or otherwise, except under the terms of the Copyright, under the terms of a license issued by the Copyright International Engineering, Science & Education Group (INESEG), without the permission in writing of the Publisher. Requests to the Publisher should be addressed to the Permissions Department, International Engineering, Science & Education Group (INESEG), or emailed to info@ineseg.org

Designations used by companies to distinguish their products are often claimed as trademarks. All brand names and product names used in this journal are trade names, service marks, trademarks or registered trademarks of their respective owners. The Publisher is not associated with any product or vendor mentioned in this journal.

This publication is designed to provide accurate and authoritative information in regard to the subject matter covered. It is sold on the understanding that the Publisher is not engaged in rendering professional services. If professional advice or other expert assistance is required, the services of a competent professional should be sought.

EUROPEAN JOURNAL OF TECHNIQUE (EJT)

ISSN-Printed: 2536-5010

ISSN-Online: 2536-5134

Scope: European Journal of Technique (EJT) established in 2010. It is a peer –reviewed international journal to be of interest and use to all those concerned with research in various fields of, or closely related to, Engineering disciplines. European Journal of Technique (EJT) aims to provide a highly readable and valuable addition to the literature which will serve as an indispensable reference tool for years to come. The coverage of the journal includes all new theoretical and experimental findings in the fields of Engineering or any closely related fields. The journal also encourages the submission of critical review articles covering advances in recent research of such fields as well as technical notes.

The scopes include:

- Mechanical Engineering
- Textile Engineering
- Electrical-Electronics Engineering
- Computer and Informatics Engineering
- Civil and Architecture Engineering
- Mining Engineering
- Chemical Engineering
- Metallurgical and Materials Engineering
- Environmental Engineering
- Food Engineering
- Geological Engineering
- Industrial Engineering
- Renewable Energy

Editor-in-Chief

- Musa YILMAZ

Publisher Of Journal

- Heybet KILIÇ

ETHICS and POLICIES

European Journal of Technique (EJT) is committed to following the Code of Conduct and Best Practice Guidelines of COPE (Committee on Publication Ethics). It is a duty of our editors to follow Cope Guidance for Editors and our peer-reviewers must follow COPE Ethical Guidelines for Peer Reviewers. We expect all prospective authors to read and understand our Ethics Policy before submitting any manuscripts to our journals.

Please note that submitted manuscripts may be subject to checks using the iThenticate service, in conjunction with CrossCheck, in order to detect instances of overlapping and similar text.

The [iThenticate](#) software checks submissions against millions of published research papers, documents on the web, and other relevant sources. If plagiarism or misconduct is found, consequences are detailed in the policy.

The chief goal of our policy is threefold: to provide advice for our authors, to maintain the scholarly integrity of our journals and their content, and to detail the ethical responsibilities of EJT, our editors and authors.

We expect all authors to read and understand our ethics policy before submitting to any of our journals. This is in accordance with our commitment to the prevention of ethical misconduct, which we recognise to be a growing problem in academic and professional publications. It is important to note that most incidents of plagiarism, redundant publication, copyright infringement or similar occur because of a lack of understanding, and not through fraudulent intent. Our policy is one of prevention and not persecution.

If you have any questions, please contact the relevant editorial office, or European Journal of Technique (EJT)' ethics representative: ejtineseg@gmail.com

Download a PDF version of the Ethics and Policies [PDF,392KB].

Authors' Responsibilities

Authors should:

- Ensure that all researched work submitted is original, fully referenced and that all authors are represented accurately. The submission must be exclusive and not under consideration elsewhere.
- Provide accurate contact details for a designated corresponding author, who shall be deemed by the publisher and editor as fully responsible for the authorship of the paper and all communications concerning the ethical status and originality of the paper. This includes any queries or investigations that may arise, pre- or post publication.
- Openly disclose the source of all data and third party material, including previously unpublished work by the authors themselves. Anything that could compromise the originality of the submission should be expressly avoided and/or discussed with the editorial office in the first instance.
- Identify any third party material that they intend to include in their article, and obtain written permission for re-use in each instance from the relevant copyright holders. Such permissions should be submitted once the manuscript is accepted, or requires small changes to be accepted. For further guidance on seeking permission to use 3rd party material please see the Rights and Permissions section.
- Openly disclose any conflict of interest - for example, if publication were to benefit a company or services in which the author(s) has a vested interest.

- Expect to formally agree publication terms which defines the author and the publishers rights for the work. Visit our website for further information.
- Expect the editor to scan submissions using plagiarism detection software at [iThenticate](#) to check a paper's originality before sending out for review.
- Fully correspond and comply with the editor and publisher in any requests for source data, proof of authorship or originality in a timely manner, providing reasonable explanation for discrepancies or failures to disclose vital information.
- Fully co-operate with any consequent investigations if the editor and/or publisher are dissatisfied with the evidence available or the explanations provided.
- Expect transparency, efficiency and respect from the publisher and the editor during the submissions process.
- Remain in good communication with both the publisher and the editor.
- When necessary, submit corrigenda in a timely and responsible fashion.
- Co-operate fully with the publication of errata and with the retraction of articles found to be unethical, misleading or damaging.
- Remain in good communication with the editor(s), the publisher and any co-authors.

Editors' Responsibilities

Editors should:

- Read and understand [COPE](#) guidelines as well as EJT's ethics policy, and follow them during all editorial processes.
- Protect the reputation of their journal(s) and published work by only publishing content of the highest quality and relevance in a timely and responsible manner.
- Carry out thorough, objective and confidential peer review for original article submissions that pass the initial quality check and editorial assessment, in adherence with [COPE](#) guidelines and EJT' ethics policy.
- Detail and justify any article types which will not be peer reviewed (e.g. editorials, opinion pieces etc.).
- Provide a transparent review and publication process as far as is possible, with full respect and care paid to the author(s).
- Provide advice and give reasonable explanation and updates to authors during the submissions process and once a decision has been made.
- Allow authors the right to appeal any editorial decision.
- Only accept papers based on the original merit, quality and relevance of their content.
- Support authors in queries concerning the originality of their submissions and request the support of EJT if necessary.
- Advise the publisher of any third party material which has been included for which they do not believe sufficient permission has been cleared.

- Be ready and prepared to publish corrections, corrigenda, errata when necessary, as well as retract articles that (the editor and EJT) deem unethical, misleading or damaging.
- Remain in good communication with both the publisher and the author(s).

Reviewers' Responsibilities

Reviewers should:

- Adhere to EJT's policy of confidential peer review of their journals. This includes, but is not restricted to, keeping their identity hidden from authors and not externally distributing any work that is passed to them for their eyes only.
- Only accept invitations to review work that is relevant to their own expertise and speciality.
- Review submitted work in a responsible, impartial and timely manner.
- Report any suspected ethical misconduct as part of a thorough and honest review of the work.
- Avoid the use of unnecessarily inflammatory or offensive language in their appraisal of the work.
- Accept the commitment to review future versions of the work and provide 'follow up' advice to the editor(s), if requested.
- Seek advice from the editor if anything is unclear at the time of invitation.
- Remain in good communication with both the publisher and the editor.

EJT's Responsibilities

EJT will:

- Protect the reputation of our journals and published work by only publishing content of the highest quality and relevance in a timely and responsible manner.
- Provide detailed information concerning both our understanding of publication ethics and our implementation of the same. Emphasise a desire for prevention, not eventual detection, of ethical misconduct.
- Uphold our COPE membership (or of such similar organisations) and keep our editorial offices, publishing staff and society partners up-to-date with their guidelines and policies, adapting our own where appropriate (and publicising any update).
- When necessary, request proof of originality/accuracy from the corresponding author of any work submitted to any of our journals.
- Use plagiarism detection software when necessary for any submission to any journal at any stage of the submissions and publication process.
- Provide a transparent submissions and publication process, with full respect and care paid to the author. This includes detailed and dedicated instructions to authors for each journal, outlining referencing style, accepted article types and submission processes.

- Investigate thoroughly any suggestion of ethical misconduct detected during any stage of the submissions process. This can include, but is not restricted to, the following: plagiarism, redundant publication, fabrication or misuse of data and authorial disputes.
- When necessary, retract articles that we deem to be unethical, misleading or damaging.
- When necessary, publish errata, corrigenda and retractions in a timely and responsible fashion, detailing the decision online in an open access format and publishing in print as soon as possible.
- Remain in good communication with editors, authors, reviewers and society partners (where applicable).

Further reading

- Authorship of the paper: Authorship should be limited to those who have made a significant contribution to the conception, design, execution, or interpretation of the reported study.
- Originality and plagiarism: The authors should ensure that they have written entirely original works, and if the authors have used the work and/or words of others that this has been appropriately cited or quoted.
- Data access and retention: Authors may be asked to provide the raw data in connection with a paper for editorial review, and should be prepared to provide public access to such data.
- Multiple, redundant or concurrent publication: An author should not in general publish manuscripts describing essentially the same research in more than one journal or primary publication. EJT do not view the following uses of a work as prior publication: publication in the form of an abstract; publication as an academic thesis; publication as an electronic preprint. Information on prior publication is included within each EJT and its journal Guideline for Authors.
- Acknowledgement of sources: Proper acknowledgment.
- Disclosure and conflicts of interest: All submissions must include disclosure of all relationships that could be viewed as presenting a potential conflict of interest.
- Fundamental errors in published works: When an author discovers a significant error or inaccuracy in his/her own published work, it is the author's obligation to promptly notify the journal editor or publisher and cooperate with the editor to retract or correct the paper.
- Reporting standards: Authors of reports of original research should present an accurate account of the work performed as well as an objective discussion of its significance.
- Hazards and human or animal subjects: Statements of compliance are required if the work involves chemicals, procedures or equipment that have any unusual hazards inherent in their use, or if it involves the use of animal or human subjects.
- Use of patient images or case details: Studies on patients or volunteers require ethics committee approval and informed consent, which should be documented in the paper.

EJT has also accessed and learned from the existing policies of other publishers and leading experts as well as open access articles that detail and define ethical misconduct.

- 'Plagiarism and the law', Joss Saunders, Learned Publishing, 23:279-202: <http://www.ingentaconnect.com/content/alpsp/lp/2010/00000023/00000004/art00002>
- iThenticate Plagiarism Resources: <http://www.ithenticate.com/resources/6-consequences-of-plagiarism>

Editor-in-Chief

Musa Yilmaz, Batman University, Turkey

International Editorial Board

| | |
|---------------------------|---|
| Aayush Shrivastava | University of Petroleum and Energy Studies, Dehradun, India |
| Adelino Pereira | Engineering Institute of Coimbra, Portugal |
| Ahmad Fakharian | Islamic Azad University, Qazvin, Iran |
| Ahmed Saber | Cairo University, Egypt |
| Arvind Kumar Jain | Rustam Ji Institute of Technology, India |
| Aydogan Ozdemir | Istanbul Technical University, Turkey |
| Baseem Khan | Hawassa University, Hawassa, Ethiopia |
| Behnam Khakhi | University of California Los Angeles, US |
| Behnam Mohammadi-ivatloo | University of Tabriz, Tabriz, Iran |
| Bharti Dwivedi | Institute of Engineering & Technology, Lucknow, UP, India |
| Carlos A. Castro | University of Campinas – UNICAMP, Brasil |
| Deepak Kumar | University of Petroleum & Energy Studies (UPES), India |
| Ernesto Vazquez | University of Nuevo Leon, Mexico |
| Faisal Khan | COMSATS Institute of Information Technology, Pakistan |
| Farhad Shahnia | Murdoch University, Perth, Australia |
| Farrokh Aminifar | University of Tehran, Iran |
| Fatih Kocycigit | Dicle University, Turkey |
| Fiaz Ahmad | National University of Computer and Emerging Sciences, Pakistan |
| Furkan Emre Sahin | Maxim Integrated, San Jose, CA, US |
| Gouthamkumar Nadakuditi | V R Siddhartha Engineering College, India |
| Hafiz Ahmed | School of Mechanical, Coventry University, UK |
| Hamed Pourgharibshahi | Lamar University, US |
| Hassan Bevrani | University of Kurdistan, Iran |
| Hemant Kumar Gianey | Thapar University, Patiala, Punjab, India |
| Hessam Golmohamadi | Semnan University, Semnan, Iran |
| Hilmy Awad | Helwan University, Cairo, Egypt |
| Idris Candan | Kocaeli University, Turkey |
| Jamshed Ahmed Ansari | Sukkur IBA University, Pakistan |
| José A. Domínguez-Navarro | University of Zaragoza, Spain |
| Kalpana Chauhan | Galgotias College of Engineering and Technology, India |
| Khaled Ellithy | Qatar University, Doha, Qatar |
| Kim-Doang Nguyen | South Dakota State University, US |
| Kundan Kumar | KIIT University, India |
| Lalit Kumar | GBPIET Pauri, India |
| Leila Mokhnache | University of Batna 2, Algeria |
| Linquan Bai | ABB Inc., US |
| Md Shafiullah | King Fahd University of Petroleum & Minerals, Saudi Arabia |
| Mohamed Shaaban | Universiti Malaysia Sarawak, Malaysia |
| Mohammed Albadi | Sultan Qaboos University, Oman |

| | |
|---------------------------|---|
| Mohd Tariq | Aligarh Muslim University, India |
| Mousa Marzband | Northumbria University, Newcastle upon Tyne, United Kingdom |
| Neeraj Kanwar | Manipal University Jaipur, India |
| Nishant Kumar | Indian Institute of Technology Delhi, India |
| Nitin Kumar Saxena | Wolaita Sodo University, Ethiopia |
| Nouar Tabet | University of Sharjah, UAE |
| Omar Hafez | Umm Al-Qura University, Makkah, Saudi Arabia |
| Omveer Singh | Gautam Buddha University, India |
| Payam Teimourzadeh Baboli | University of Mazandaran (UMZ), Iran |
| Payman Dehghanian | George Washington University, US |
| Ragab A. El Sehiemy | Faculty of Engineering, Kafrelsheikh Univrsity, Egypt |
| Rajeev Kumar Chauhan | Galgotias College of Engineering and Technology, India |
| Rajiv Singh | G.B. Pant University of Agriculture & Technology, India |
| Reza Sharifi | Amir Kabir university Tehran, Iran |
| Rudranarayan Senapati | Kalinga Institute of Industrial Technology, India |
| Saleh Y. Abujarad | Universiti Teknologi Malaysia, Malaysia |
| Sanjay Dambhare | College of Engineering, Pune, India |
| Saptarshi Roy | NIT Warangal, India |
| Shailendra Kumar | Indian Institute of Technology Delhi, India |
| Shariq Riaz | The University of Sydney, Australia |
| Shengen Chen | University of Maine, US |
| Syafaruddin | Universitas Hasanuddin, Indonesia |
| T. Sudhakar Babu | VIT University, Vellore, India |
| Thamer Alquthami | King Abdulaziz University, Saudi Arabia |
| Theofilos Papadopoulos | Democritus University of Thrace, Greece |
| Uday P. Mhaskar | CSA Group, US |
| Vedat Veli Cay | Dicle University, Turkey |
| Yogesh Rohilla | K Lakshmiapat University, Jaipur, India |
| Yunfeng Wen | School of Electrical Engineering, Chongqing University, China |
| Zbigniew M. Leonowicz | Wroclaw University of Science and Technology, Poland |

Publisher of Journal

Heybet Kilic

CONTENTS

| | |
|--|---------|
| ESTIMATING BASE STATION-BASED INDOOR AND OUTDOOR ELECTRIC FIELD LEVELS BY ARTIFICIAL NEURAL NETWORKS | 1-12 |
| THE EFFECT OF HOT WATER AGEING ON THE GLASS FIBER REINFORCED EPOXY COMPOSITE | 13-24 |
| THE PROPERTIES OF CADMIUM OXIDE-CARBON NANOTUBE NANOCOMPOSITE SYNTHESIZED VIA SOL-GEL METHOD | 25-36 |
| COMPARISON OF THE PRINTING AREAS FOR COMMONLY USED FONT TYPES: EXAMPLE OF GREEN INFORMATION | 37-43 |
| A GEOLOGICAL AND PETROLOGICAL OVER VIEW OF THE HISTORY OF KIRA MOUNTAIN: AN APPROACH TO THE SIMILARITY AND DIFFERENCE OF KARACADAG | 44-51 |
| ASSESSMENT OF ENERGY PERFORMANCE BASED ON ENERGY AUDIT OF A HOTEL USING EXERGY APPROACH | 52-65 |
| ORGANIC MATERIAL POTENTIAL AND ENERGY ANALYSIS FOR BIOGAS APPLICATION OF BATMAN | 66-73 |
| APPLICATION OF DECISION TREE METHODS FOR WIND SPEED ESTIMATION | 74-83 |
| THE EFFECT OF GRAPHENE OXIDE ON THE STRUCTURAL AND ELECTRICAL PROPERTIES OF YTTRIUM FERRITE BASED NANOPOWDERS | 84-98 |
| THE EVALUATING OF WIND ENERGY POTENTIAL OF DİYARBAKIR USING WEIBUL AND RAYLEIGH DISTRIBUTION | 99-113 |
| CALCULATING ENERGY-INDUCED CARBON FOOTPRINT: BATMAN UNIVERSITY CASE | 114-120 |

ESTIMATING BASE STATION-BASED INDOOR AND OUTDOOR ELECTRIC FIELD LEVELS BY ARTIFICIAL NEURAL NETWORKS


Esin KARPAT^{1*}, Muhammed Rafet BAKCAN², Mustafa Mohamedosman Abbaker IBRAHIM³, Berkant ÇELİK⁴, Ahmed Takieddine CHABBAR⁵, Oğuzhan DOĞAN⁶


The measurement of the electric field and the magnetic field is significant in order to determine electromagnetic pollution level compared to standards. In Turkey, electric field limit value, which is emitted by base station is 13.5 V/m for one mobile communication operator. In addition, according to the regulation of medical devices, the limit of electric field value inside the hospital, where the medical devices are located, is 3 V/m. In this study, the measurement and evaluation of electromagnetic pollution inside and outside the Bursa Uludag University hospital building are performed and its compliance with national and international standards is examined. Moreover, the distribution of electric field in the environment is estimated by the artificial neural network and fuzzy logic methods considering the measurement results. The measured electric field values, estimated electric field values, and national standard values are compared.


Key words: *Electromagnetic pollution, Electrical field, artificial neural network, fuzzy logic, prediction.*

1. Introduction


In the shadow of these days, electromagnetic waves (EM) have become a complementary part of our every day life. This influences almost every aspect of our day-to-day life. However, the electromagnetic waves are radiated from natural, man-made sources such as TV, radio, wireless, Internet, cellular communication, and many other devices which are also exchanging increasing amounts of data by means of radio frequency (RF). So, this leads to installation of more base stations to cover new areas with new technology to work within the limited geographic area for unlimited


¹ Department of Electrical and Electronics Engineering, Bursa Uludag University, Bursa, Turkey, (esinoz@uludag.edu.tr)  <https://orcid.org/0000-0002-2740-8183>

² Department of Electrical and Electronics Engineering, Bursa Uludag University, Bursa, Turkey, (muhamedrbakcan@outlook.com)  <https://orcid.org/0000-0002-9427-7371>

³ Department of Electrical and Electronics Engineering, Bursa Uludag University, Bursa, Turkey, (Eng.mustafa1988s@gmail.com)  <https://orcid.org/0000-0003-1915-2349>

⁴ Department of Electrical and Electronics Engineering, Bursa Uludag University, Bursa, Turkey, (berkantcelik@hotmail.com.tr)  <https://orcid.org/0000-0001-7457-5577>

⁵ Department of Electrical and Electronics Engineering, Bursa Uludag University, Bursa, Turkey, (ahmedchabbar@gmail.com)  <https://orcid.org/0000-0002-5919-399X>

⁶ Department of Mechanical Engineering, Bursa Uludag University, Bursa, Turkey, (doganoguz@uludag.edu.tr)  <https://orcid.org/0000-0003-4203-8237>

users. That means the exposure of high levels of Electromagnetic Radiation (EMR) due to high RF power broadcasting in order to maximize the coverage of area [1-5].

Overall, EM waves, which have very wide range of frequencies, are part of non-ionizing radiation. While the operating system and frequencies can be in the range between 27 MHz – 300 GHz. In the best case, in Europe and Turkey there is over 600 MHz of spectrum available for mobile operators including the 800, 900, 1800, 2100 and 2600 MHz Frequency Division Duplex (FDD) and Time Division Duplex (TDD) bands (GSM, CDMA, UMTS, LTE respectively, or a combination of generation technologies) [6,7]. The health effects of base stations and mobile phones in Turkey are really a tender topic. In gathering the accepted limits in many countries including European Union and the USA are recommended by The International Commission on Non-Ionizing Radiation Protection (ICNIRP), which is recognized by the World Health Organization (WHO). Turkey applies the limits which are determined in accordance with ICNIRP's limits [7]. Although, many parameters can change the EMR values such as the distance from base stations, the line of side path, the weather and Geographic nature and the number of traffic in the channel or the capacity of users in one cell. Thus, measurement and statistical evaluation have a large importance in the determination of EMR limits.

In the literature, there are many studies about the effect of high-frequency electromagnetic fields on human health. These studies were carried out with some animals, especially farm animals, as well as humans [8]. Research on humans has focused on children, adults and the elderly. High-frequency electromagnetic field was applied to tissues, such as skin, brain, etc. of children of up to 10 years old, and the resultant effects were compared with the results of adults. [9].

In addition, some studies have shown that children in the womb do not have cancer risk based on base station radiation [10]. In studies on children [11], the level of the electromagnetic pollution that the children between 1-10 years old are exposed to, due to wireless communication devices, are measured and Specific Absorption Rate (SAR) values of body tissues are compared with international standards [12].

In studies about sparrows, it was found that in the regions exposed to the frequencies of 900 MHz and 1800 MHz, the male sparrows were found to be less and this would have a negative effect on semination period [13].

Exposure of electromagnetic measurement in the GSM band studies is performed in regions where the population density is excessive. The mapping in the measured region is carried out and the results are compared with the international standards, determinations to determine the regions which have a negative effect on human health [14-20].

SAR values generated in case of close proximity to indoor devices, such as wireless baby monitors, phones, wireless headphones with different output powers, are calculated, the maximum and the average exposure Electromagnetic field (EMF) values are measured and evaluated [21].

The electromagnetic pollution, in the places where the mobile network is installed, can affect the communication of new networks. New methods are used to detect and reduce pollution [22].

In studies about the estimation of electromagnetic pollution in the literature, wireless electromagnetic field value detection in the indoor environment was estimated by Artificial Neural Networks (ANN) according to the position in the region. The attenuation effect of the facility obstacles between the base station and the mobile phone is estimated by artificial neural networks according to the mobile phone communication frequencies [23].

EMR has been obtained by artificial neural networks considering the parameters, such as building materials, window dimensions, and the number of windows in places such as houses, schools, and complex buildings [24].

The aim of this study is to measure and statistically analyse the EMR limits for GSM (2G&3G) and LTE (4G&4.5G). The electric field values on specific position from the base station were measured at different times of the days. The measurements were carried out at 45 different outdoor and 33 indoor locations in Bursa Uludag University's main campus and inside and outside the Faculty of Medicine Hospital. In this study, the predicted outdoor electromagnetic pollution values by artificial neural network and fuzzy logic are presented.

2. Electromagnetic Wave Propagation

Electromagnetic waves, which are the result of time-varying electric and magnetic fields, are means of energy or information. Typical electromagnetic waves are TV signals, radar rays, and radio waves. All electromagnetic waves have their signature features; they move at high speed and spread out from the source.

Electromagnetic waves, at distances sufficiently far from sources can be approximated as uniform plane waves. The E and H field components of these waves are everywhere normal to each other and to the direction of wave propagation [25].

The time-average power density carried by the electromagnetic wave can be calculated as

$$\vec{P}_{ave}(z) = \frac{1}{T} \int_0^T \vec{P}(z, t) dt \quad (1)$$

where; $\vec{P}(z, t)$ is the Poynting vector representing the instantaneous power density crossing unit area at a specific time in Eq.(2).

$$\vec{P}(z, t) = \vec{E} \times \vec{H} \quad (2)$$

The time-average power density carried by the electromagnetic wave can be also calculated as

$$\vec{P}_{ave} = \frac{1}{2} \text{Re} \{ \vec{E}_s \times \vec{H}_s^* \} \quad (3)$$

where \vec{E}_s and \vec{H}_s^* are the phasor forms of electric field and conjugate of magnetic field, respectively. The intrinsic impedance of the medium is calculated as

$$Z_0 = \frac{E_0}{H_0} \quad (4)$$

In the far field region, where the electromagnetic waves are referred to as radiative field, the electric field, magnetic field and power density are combined together with Eq. (5).

$$P = \frac{E_0^2}{Z_0} \text{ or } P = H_0^2 Z_0 \quad (5)$$

where P ; Power density, (Watt/m^2), E_0 ; Electric field intensity (V/m), H_0 ; Magnetic field intensity (A/m) and Z_0 ; characteristic Impedance of free space, which is approximately 377Ω [26].

Eq. 5 shows that, in the far field, the measurement of the electric field or the magnetic field gives information about the electromagnetic level of the medium [25,27] and when the value of one of the field components is measured the other can be calculated.

3. Measurement

In this study, the electromagnetic pollution caused by the base station was measured in and around Bursa Uludag University medical school. The measurement results are divided into frequency ranges between 27 MHz to 3 GHz, allocated by the ICTA and classified as GSM, UMTS, LTE and other frequencies other than these frequencies. Measurements were carried out inside and outside the hospital building.

The measurements outside the hospital were performed at the main entrance because of high density of people. The measurement points were selected as the places where the medical devices are located, the clinics close to the base station, the corridors and waiting rooms inside the hospital. The position and the measurement time are randomly selected and the most important selection criterion is determined to be the population density for indoor measurement. A total of 33 points were identified for indoor environment.

The measurement points in the front were close to the building and were across the base station. The measurements were carried out behind the windows and walls that face the base station.

In addition, measurements were performed inside the clinics and compared with national standards.

The measurement position and the measurement time are taken into consideration for outside measurement. A total of 45 measurements were identified for outdoor environment. After measurements, the data in the outdoor environment were obtained by taking the 6-minute average electric field values for each position considering the latitude and longitude of the measurement point and measurement time.

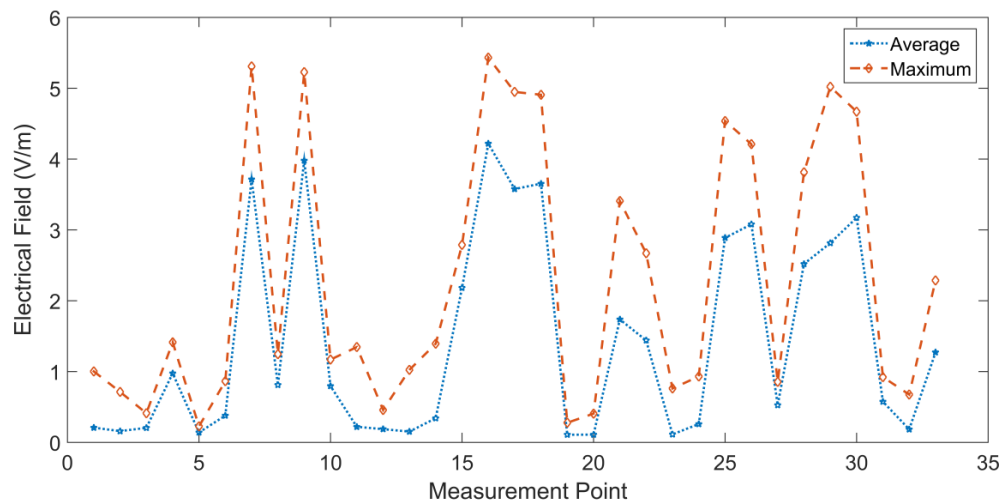


Figure 1. Indoor maximum and average electrical field value

The maximum value obtained indoor is 4.314 V/m and the minimum electric field value is 0.108 V/m . The highest electric field value was detected on the 3rd floor of the building behind the window facing the base station. 0.97 V/m value is measured behind the wall across the same base

station. And the same value of the electric field (0.97 V/m) is obtained when the measurement is repeated behind the wall in front of the same base station, on the same floor. Average and maximum peak electric field values obtained during indoor measurements are given in Fig.1.

4. Artificial Neural Network

The results of systematic measurement of outdoor measurements are trained by artificial neural network. The output electric field values are estimated based on the input parameters of the trained network. To estimate the total electric field value, there are 3 input parameters and 1 output value as shown in Fig. 2. The input parameters are latitude, longitude and measurement time values. In order to increase the accuracy of the predicted values given by the training network, it is necessary to select the input parameters as systematically as possible. If the random values are applied as input values, the MSE (mean squared error) value increases and the accuracy of prediction value decreases. For this reason, although the number of input data is not much, three different interrelated parameters are applied to the network as input variables.

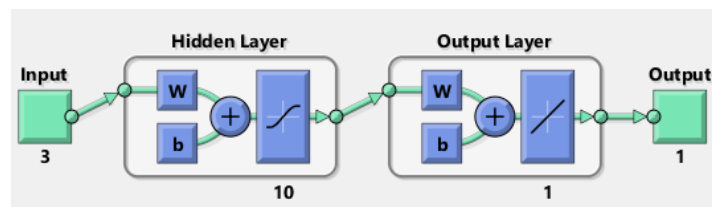


Figure 2. Input parameters, measurement time, latitude, longitude for total E field prediction

In the second artificial neural network which was constructed in the study, different output parameters were tried to be estimated by using different inputs [28]. This created network has 5 inputs and 1 output parameters. Three of the input parameters are fixed and the other 2 input parameters are changed depending on the output parameter to be obtained. The parameters that are constant are latitude, longitude and measured time values of the measurement point, while the other 2 dependent input parameters are average electric field values covering the GSM, UMTS, LTE frequencies. One of the GSM, UMTS and LTE electric field values is estimated as an output parameter while the remaining 2 frequency components are defined as input parameters in Fig. 3. For example, in order to estimate the electric field value of UMTS frequency, input parameters are latitude, longitude, measurement time, GSM and LTE electric field values.

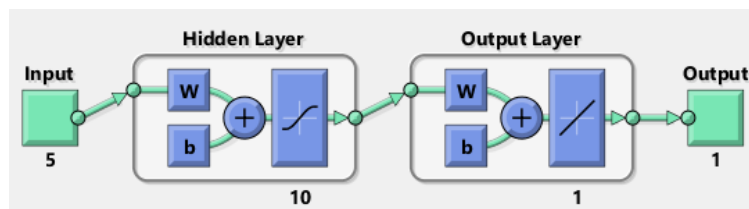


Figure 3. Input parameters; time, latitude, longitude, LTE and UMTS frequency values

In this way, the average electric field values of the other 2 frequency components are estimated using the same method. 70% of the measured data was used to train artificial neural networks, rest of

30% data were used for network test. There are 10 neurons in the hidden layer and one neuron in the output layer, in both prediction networks.

5. Fuzzy logic

Another prediction method used in the study is fuzzy logic [29]. In this method, the accuracy of the estimated results was increased. The range of input and output values was required for estimation. The input data were latitude and longitude values of the measurement point as in the ANN prediction model. However, the latitude values of the measurement points were rated between 0-400 and the longitude values were rated between 0-400 as shown in Eq. (6) and Eq. (7) respectively.

$$Lat_{out} = (Lat_{in} - 40.20696) * 10000 \quad (6)$$

$$Lon_{out} = (Lon_{in} - 28.85185) * 10000 \quad (7)$$

Since the decimal degrees of the coordinates are very small, those formulas are used. The fuzzy logic system can easily detect the distance between the measurement positions, by scaling according to a specific position by using the coordinates. The output parameter of the system is the average total electric field value. This value has been entered into the system by taking the minimum and maximum value range of the measurement data.

In the estimation with fuzzy logic, there is a relation between input and output parameters. Table of rules should be created according to the input parameter values in order to get the output parameter values. As a result of this table, an output data is estimated according to the input value.

As an input membership function, the position values are divided into 9 equal parts which are latitude and longitude of the measurement point. Rules have been created with obtained membership functions in order to calculate output values. A total of 16 rules were created to increase the accuracy of the output data.

Fuzzy logic estimation is applied to average electric field values including total average electric field value, GSM, UMTS and LTE frequency bands as in ANN estimation method. However, when the field values for these frequencies are estimated, the input parameters used are latitude and longitude values, in addition, the output values are estimated by entering the maximum and minimum measured value of this frequency as an input.

6. Results

Average field values were estimated according to the total average electric field value and frequency. Regression analysis was applied to the results obtained by artificial neural networks. The calculated regression value, R^2 , is 0.8422 for the total electric field, 0.64913 for GSM, 0.5033 for UMTS and 0.8462 for LTE. These values could be better if more measurements could have been performed. In addition, the mean square error values are calculated in order to analyse the accuracy of the prediction results given by the trained network. In Fig. 4, the MSE values for total EM (Top-Left), for GSM (Top-Right), for UMTS (Bottom-Left) and for LTE (Bottom-Right) are given.

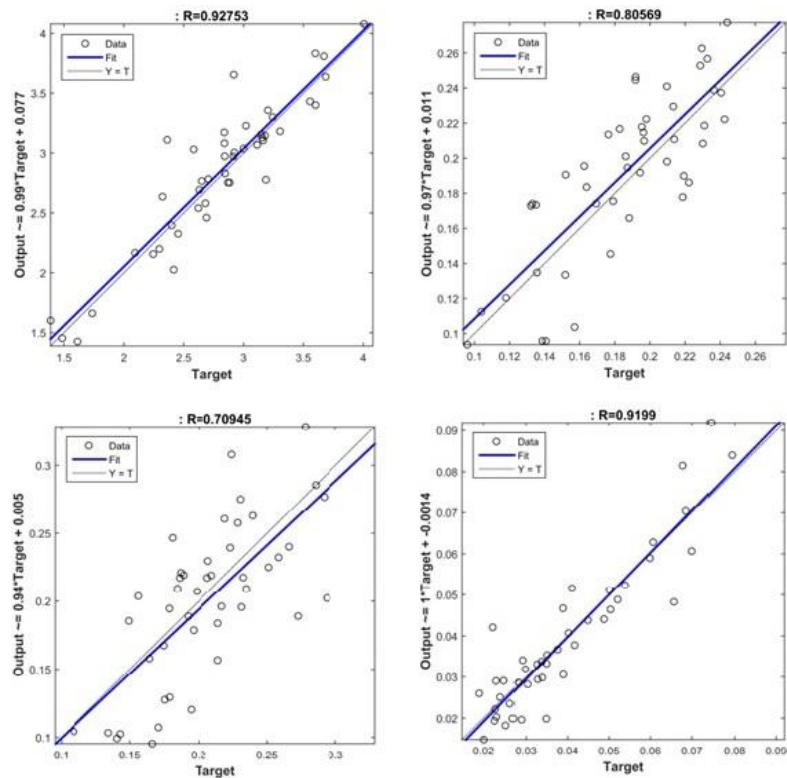


Figure 4: Total EM ANN regression (Top-left), GSM EM ANN regression (Top-right), UMTS EM ANN regression (Bottom-Left), LTE EM ANN regression (Bottom-right).

In addition, the correlation coefficient values of the Measurement-ANN-Fuzzy methods of the total average electric field, GSM average electric field, UMTS average electric field and LTE average electric field values are shown in Table 1, Table 2, Table 3 and Table 4 respectively.

Table 1. Total average E-field correlation coefficient

| Method | Fuzzy | Measurement | ANN |
|--------------------|----------|-------------|----------|
| Fuzzy | 1 | 0.942636 | 0.966254 |
| Measurement | 0.942636 | 1 | 0.921688 |
| ANN | 0.966254 | 0.921688 | 1 |

Table 2. GSM E-field correlation coefficient

| Method | Fuzzy | Measurement | ANN |
|--------------------|----------|-------------|----------|
| Fuzzy | 1 | 0.939559 | 0.819398 |
| Measurement | 0.939559 | 1 | 0.805687 |
| ANN | 0.819398 | 0.805687 | 1 |

Table 3. UMTS E-field correlation coefficient

| Method | Fuzzy | Measurement | ANN |
|--------------------|----------|-------------|----------|
| Fuzzy | 1 | 0.943614 | 0.65603 |
| Measurement | 0.943614 | 1 | 0.709447 |
| ANN | 0.65603 | 0.709447 | 1 |

Table 4. LTE E-field correlation coefficient

| Method | Fuzzy | Measurement | ANN |
|-------------|----------|-------------|----------|
| Fuzzy | 1 | 0.960722 | 0.90267 |
| Measurement | 0.960722 | 1 | 0.919899 |
| ANN | 0.90267 | 0.919899 | 1 |

Obtained measurement and estimated electric field values are compared with each other. The measurement points and the electric field values obtained at these points are plotted as V/m. In comparison, the closest prediction method has been determined with measurement values. The estimated results are compared with the values obtained by the measurements, ANN and fuzzy logic in Fig. 5, Fig.6, Fig. 7 and Fig. 8 respectively.

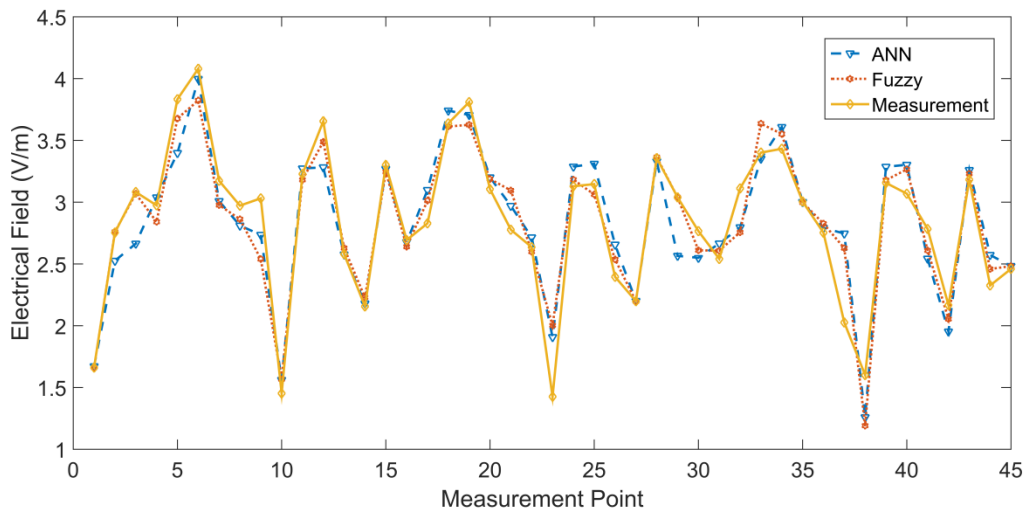


Figure 5. Total average E- Field

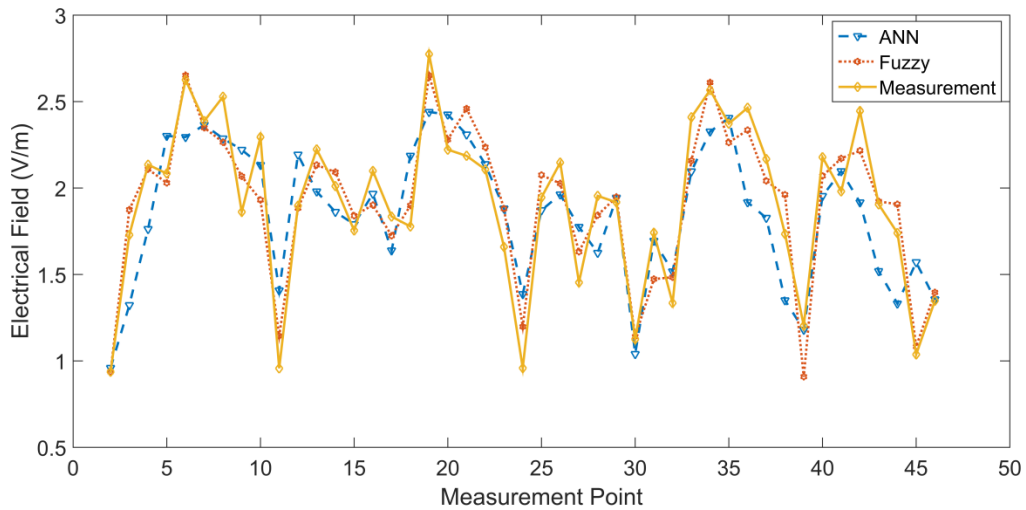


Figure 6. GSM E-Field

When Table 1 and Fig. 5 are analyzed, it is seen that the correlation rate between measurement data and fuzzy logic is 94%, as well as it is 92% between measurement and ANN. When the results for GSM are examined in Table 2, the similarity is 93% between measurement data and fuzzy logic and 80% between measurement and ANN as it is seen in Fig. 6.

For UMTS, there is a 94% correlation between measurement data and fuzzy in (Table3 and Fig.7) and 70% between the measurement and ANN. Finally, the graph obtained for LTE shows a correlation of 96% between measurement and fuzzy and 91% between measurement and ANN (Table 4 and Fig. 8).

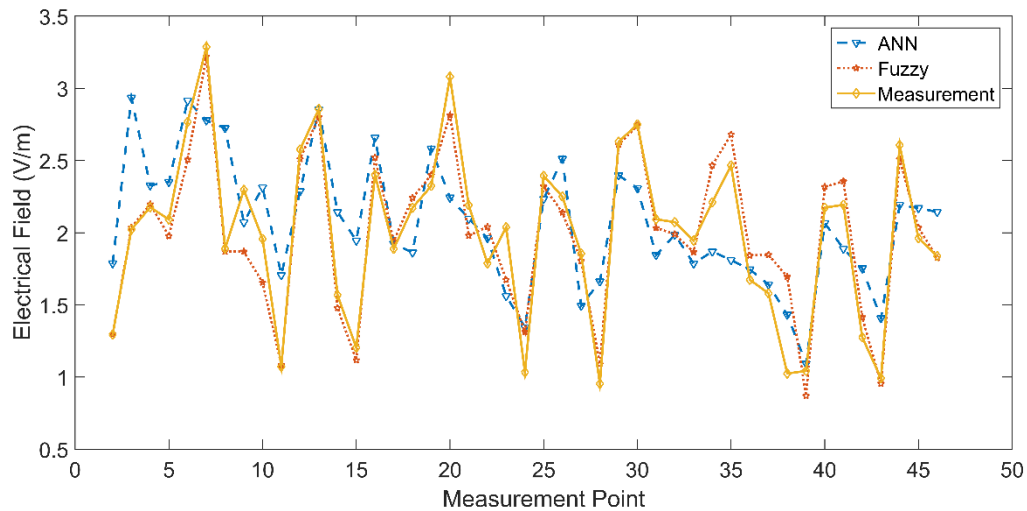


Figure 7. UMTS E-Field

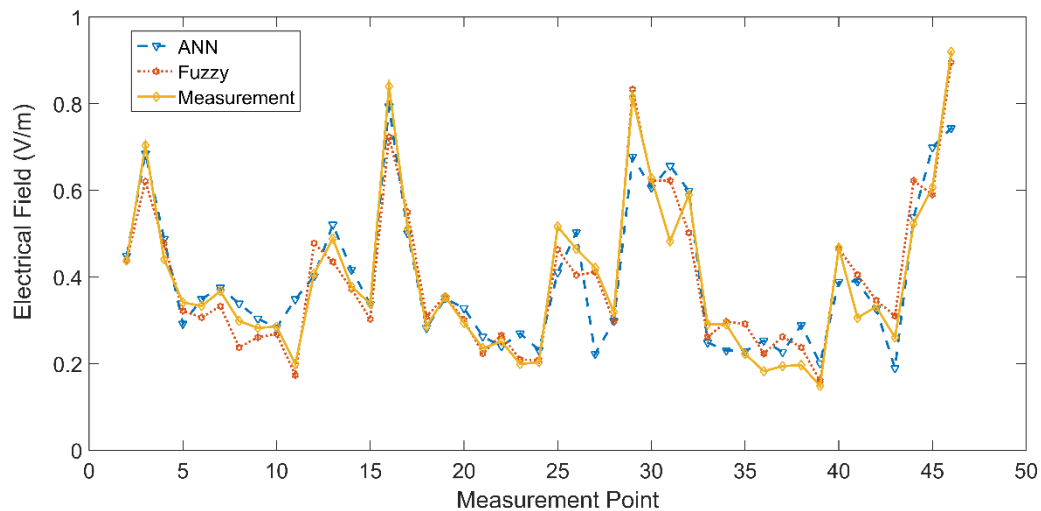


Figure 8. LTE E-Field

7. Conclusions

The average electrical field value level of the environment in clinics with medical devices required by national standards should not exceed 3 V/m for indoor measurements. As a result of measurements, the highest measured value was found to be 2.88 V /m in clinics and the most

important parameter of signal attenuation was found to be due to the building materials of concrete walls which have 75-80 cm thickness approximately.

When the estimation methods and measurement results are compared, accuracy of fuzzy logic estimation results are higher than ANN estimation results which is determined by the average electric field.

When the obtained data are compared with the measured average results, it is observed that the electric field values change nonlinearly. For this reason, it is possible to obtain better learning of the network by taking more measurements in future studies in order to increase the accuracy of predictions.

In this study, it was determined that the average electric field value within the region can be estimated with latitude and longitude values only in the regions with a certain amount of base stations.

Finally, the measurement and estimation of the electromagnetic pollution, which is a result of 2G, 3G and 4.5G communication infrastructure are performed and the capability of both ANN and fuzzy logic methods are illustrated.

8. Acknowledgements

This Study is supported by the Uludag University AYP (MH2016/1) Scientific Research Project.

9. References

- [1] Kurnaz, C. (2016). An Empirical Modeling of Electromagnetic Pollution on a University Campus. *ACES Express Journal*, Vol. 1- 2, pp. 76-79.
- [2] Kurnaz, C., Yıldız, D., Karagol, S. (2017). Assessment Of Short/Long Term Electric Field Strength Measurements for a Pilot District. 18th International Symposium Electromagnetic Fields in Mechatronics, Electrical and Electronic Engineering (ISEF) Book of Abstracts.
- [3] Mousa, A. (2011). Electromagnetic Radiation Measurements and Safety Issues of Some Cellular Base Stations in Nablus. *Journal of Engineering Science and Technology Review*, Vol. 4-1, pp. 35-42.
- [4] ICNIRP(2002). Statement General Approach to Protection Against Non Ionizing Radiation, *Health Physics* 82(4), pp.540-548.
- [5] Health and Electromagnetic Fields, <https://ec.europa.eu>.
- [6] ICTA Turkey Electromagnetic Exposure Standards, <https://www.btk.gov.tr/en-US/>.
- [7] ICNIRP Guidelines(1998). Guidelines for Limiting Exposure to Time-Varying Electric, Magnetic, and Electromagnetic Fields (up to 300GHz). International Commission on Non-Ionizing Radiation Protection, *Health Physics* vol.74, no.4, pp.494-522.
- [8] Liechti, R., Stärk, K. D. C., Mobile Communication Base Stations and Animal Health Risk Perception Among Swiss Veterinarians and Farmers. 10th International Symposium on Veterinary Epidemiology and Economics, 2003.

- [9] Ibrani, M., Ahma, L., Hamiti, E., Haxhibeqiri, J.(2011). Derivation of Electromagnetic Properties of Child Biological Tissues at Radio Frequencies. *Progress in Electromagnetics Research Letters*, Vol. 25, pp. 87-100.
- [10] Elliott, P., Toledano, M.B., Beale, L., Hoogh, K., Best, N., Briggs, D.J.(2010). Mobile Phone Base Stations and Early Childhood Cancers: Case-Control Study. *BMJ*, Vol:22;340:c3077.
- [11] Lee, K., Yun, J. (2011). A Comparison of Specific Absorption Rates in SAM Phantom and Child Head Models at 835 and 1900 MHz. *IEEE Transactions On Electromagnetic Compatibility*, Vol. 53, No. 3, pp. 619-627.
- [12] Ibrani, M., Ahma, L., Hamiti, E. (2014). Assessment of The Exposure of Children to Electromagnetic Fields from Wireless Communication Devices in Home Environments. *IET Communications*, Vol. 8-12, pp. 2222–2228.
- [13] Everaert, J., Bauwens, D. (2007). A Possible Effect of Electromagnetic Radiation from Mobile Phone Base Stations on the Number of Breeding House Sparrows (*Passer domesticus*). *Electromagnetic Biology and Medicine*, Vol. 26, pp. 63–72.
- [14] Sorgucu, U., Develi, I.(2012). Measurement and Analysis of Electromagnetic Pollution Generated by GSM-900 Mobile Phone Networks in Erciyes University Turkey. *Electromagnetic Biology and Medicine*, Vol. 31(4), pp. 404–415.
- [15] Peyman, A., Khalid, M., Calderon, C., Addison, D., Mee, Maslanyj, T., M., Mann, S.(2011). Assessment of Exposure To Electromagnetic Fields From Wireless Computer Networks (Wi-Fi) in Schools; Results of Laboratory Measurements. *Health Phys.*, Vol. 100-6, pp. 594-612.
- [16] Kurnaz, Ç., Engiz, B.K.(2016). Measurement and Evaluation of Electric Field Strength in Samsun City Center. *International Journal of Applied Mathematics, Electronics, and Computers*, Vol. 4, pp. 24-29.
- [17] Engiz, B. K., Kurnaz, C.(2016). Long-Term Electromagnetic Field Measurement and Assessment for A Shopping Mall. *Radiation Protection Dosimetry*, pp. 1–9.
- [18] Sarolic, A., Matic, P. (2010). Wireless LAN Electromagnetic Field Prediction for Indoor Environment Using Artificial Neural Network. *Automatika*, Vol. 51-3, pp. 233–240.
- [19] Gül, B. K., Kurnaz, Ç., Engiz, B. K. (2015). Measurement and Evaluation of Electromagnetic Pollution in Ondokuz Mayıs University Kurupelit Campus in Samsun Turkey. *Third Intl. Conf. on Advances in Information Processing and Communication Technology – IPCT*.
- [20] Tuysuz, B., Mahmutoglu, Y. (2017). Measurement and Mapping of the GSM-Based Electromagnetic Pollution in the Black Sea Region of Turkey. *Electromagnetic Biology and Medicine*, Vol. 36- 2, pp.132–140.
- [21] Schmid, G., Lager, D., Preiner, P., Berbacher, R. U., Cecil, S.(2007). Exposure Caused by Wireless Technologies Used for Short-Range Indoor Communication in Homes and Offices. *Radiation Protection Dosimetry*, Vol. 124-1, pp. 58–62.
- [22] Diaz, P. G., Sanz, S. S., Figueras, J.A.P., Fernández, S. J.(2013). Mobile Network Deployment Under Electromagnetic Pollution Control Criterion: An Evolutionary Algorithm Approach. *Expert Systems with Applications*, Vol. 40, pp. 365–376.

- [23] Perez, P. G., García, M. C., Cuiñas, I., Caldeirinha, R. F.S.(2017). Modeling and Inferring the Attenuation Induced by Vegetation Barriers at 2G/3G/4G Cellular Bands Using Artificial Neural Networks. *Measurement*, Vol. 98, pp.262–275.
- [24] Beekhuizen, J., Vermeulen, R., Eijdsen, M. V. , Van Strien, R., Bürgi, A., Loomans,E., Guxens, M., Kromhout, H., Huss, A. (2014). Modelling Indoor Electromagnetic Fields (EMF) from Mobile Phone Base Stations for Epidemiological Studies. *Environ Int.* Vol. 67, pp. 22-6.
- [25] Sadiku, M., *Elements of Electromagnetics*, Oxford University Press, 2007.
- [26] Dianah, A. R. S. N., . Hazmin, S. N., Umar , R., Kamarudin, M. K. A., and Dagang, A. N. (2017), A Review on Electromagnetics (EM) Exposure Measurement Techniques From Base Station, *Journal of Fundamental and Applied Sciences*, Vol. 9, pp. 182-198 doi:<http://dx.doi.org/10.4314/jfas.v9i2s.14>
- [27] Balanis, C. A., *Advanced Engineering Electromagnetics*, John Wiley & Sons, 2012.
- [28] Neural Network Toolbox™ User's Guide, Mathworks, R2017b, <http://www.mathworks.com>.
- [29] Fuzzy Logic Toolbox™ User's Guide, Mathworks, 2017, <http://www.mathworks.com>.

THE EFFECT OF HOT WATER AGEING ON THE GLASS FIBER REINFORCED EPOXY COMPOSITE

Gurbet ÖRÇEN^{1*}


In the present study, the effects of hot water ageing on the glass fiber reinforced epoxy woven composites were experimentally examined. The specimens in three groups which undamaged, damaged, and single patch-repaired ones were kept in tap water at 50°C and 70°C temperature for 8 days and 16 days. At the end of those periods, the moisture absorption rates were calculated, the maximum failure loads at the end of period of keeping in hot water were determined and the failure modes occurring on these specimens were observed and compared. As a result of experimental study, it was found that the moisture absorption rates increased but the failure load values decreased together with the increase in water temperature and duration of hot water ageing.

Key words: *Composites, Single patch-repaired, Adhesive bonded, Hot water, Environmental degradation.*

1. Introduction

In the engineering practice, the use of composite materials became very popular in terms of light weight and strength. Opening holes on the composite plates causes stress accumulation in the application sites. Moreover, the use of bolts and pins at these sites is considered as the important parameters influencing the load-carrying capacity and the damage. For this reason, the adhesive bonds are preferred in many of the composite plates bonds. Also the adhesive bonds are frequently used because of the low-cost and no-damage on the connectors. As a result of damage of composite plates because of various reasons, the adhesive bonds are generally repaired by using the patches. It is known that the mechanical properties of composites and adhesives that are used vary depending on the environmental conditions, as well as the bond types and repairing methods. Especially the moisture and thermal environments have significant effects on the performance of composites. For this reason, many researchers have investigated the durability of adhesive-bonded composites.

In literature, the adhesive patch bonds [1-28] and the effects of environmental conditions on these bonds and composites have been experimentally examined in many studies. Especially the studies on using single-patch repair [1-10,12,14,15,17], the patch applied on specimen having hole damage at the center [1,2,15,16,19], repairing the damaged composite specimens, and the effects of moisture/temperature on the composite specimens [21,24,26-28,30] have a significant place in literature. Among the studies carried out on patch, Campilho et al. [1, 2] repaired the composite plate,

^{1*} Department of Mechanical Engineering, University of Dicle, Diyarbakır, Turkey, (gurbetorcen@dicle.edu.tr) 
<https://orcid.org/0000-0002-8329-8142>

which were holed at the center, by making use of patch on the single surface. They carried out an experimental study on examining the parameters influencing the patch thickness, effect of patch length, stress distribution, and mechanical behaviors of patch-repaired composite plates. Charalambides et al. [13] experimentally analyzed the damage behaviors of single patch-repaired composite plates, on which the patch is applied on only one side, caused from the external factors. Tsouvalis et al. [15] examined the efficiency of steel plates, which have hole damage at the center and been repaired by using carbon/epoxy patch, under the static tensile load. They determined that the failure load rates of patches increased from 30% to 50%. Her et al. [16] investigated the effects of material characteristics, size, and thickness of adhesives and patches on the stress distribution of damaged composite plates repaired by using patch. Liu et al. [19] applied a prepreg external patch on the perforated composite plate, and then they performed tensile test.

For the patch-repaired composite materials, Park et al. [21] examined the effects of temperature, moisture, and cold among the environmental factors on the single patch-repaired composite connections. Akderya et al. [26] experimentally investigated the effects of thermal ageing on the tensile properties of composites, joints of which were established by using adhesives. Soykok [27] examined the behaviors of single lap adhesively bonded glass fiber-reinforced epoxy composite specimens in the hot water. The prepared composites were kept in hot water for one or two weeks at 50°C, 70°C, and 90 °C, and then tensile test was applied. Zhang et al. [28] examined the effects of hot water on the adhesive bonds between the aluminum and steel surfaces.

This experimental study; it is important to expose undamaged, damaged and patch repaired glass fiber reinforced epoxy composite specimens to hot water from environmental conditions. Also, the effects of hot water were investigated. For this purpose, the composite specimens were kept in tap water at 50°C and 70°C for 8 and 16 days. Therefore study, the results obtained from the specimens in each of the three groups is important in that together. In this study, the moisture absorption performances, maximum and minimum load damages for pre- and post-absorption and failure modes were determined and compared.

2. Materials and Methods

2.1. Material preparation

The glass fiber-reinforced woven epoxy plates with 1m x1m size were produced by using a heat-controlled vacuum infusion machine. The specimens were cut from these composite materials at the geometries to be used in the present study. The composite specimens were divided into three groups; namely the undamaged specimens in first group (Figure 1), specimens with circular hole damage at the center with 5 mm and 10 mm diameter in second group (Figure 2a, Figure 2b). The specimens in second group were repaired by using patch on one side and then the third group was constituted (Figure 3). The width (w), thickness (t), and length (L) of specimens in each group were 30 mm, 1.7 mm, and 160 mm, respectively. The dimensions of composite patches made of the same material were 30 mm x 30 mm. Three specimens were produced for each group and the specimens were prepared in accordance with ASTM 5868-01 [29]. The thickness of adhesive was 0.3 mm and the epoxy adhesive Loctite 9466 was chosen as the adhesive material. While preparing the specimens in third group, the adhesion surfaces of specimens and those of patches were cleansed by using sandpaper and then wiped with swab soaked into acetone in order to improve the adhesion quality.

A specific mold for the specimens was prepared by using a 3D printer in accordance with the sizes of damaged specimen and patch, as well as the adhesive thickness (Figure 4). The damaged

composite specimen was placed into a mold and the patch was fastened on a single side by using Loctite 9466 adhesive, thus the repaired specimens were obtained (Figure 5). These specimens repaired by using adhesive and patch were kept at room temperature for drying for 15 days. Then the specimens were fixed at 50°C and 70°C temperature and then placed into thermostat-controlled boilers, which were filled with tap water, for 8 days and 16 days. The hangers were placed into the boilers in order to prevent the specimens from contacting each other (Figure 6).

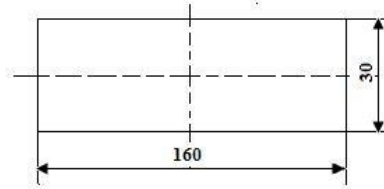


Figure 1. Glass fiber-reinforced composite specimens-Undamaged (Group I).

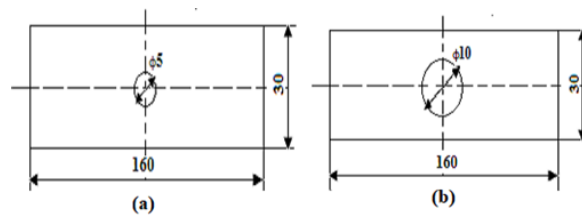


Figure 2. Specimens with circular hole damage (Group II).

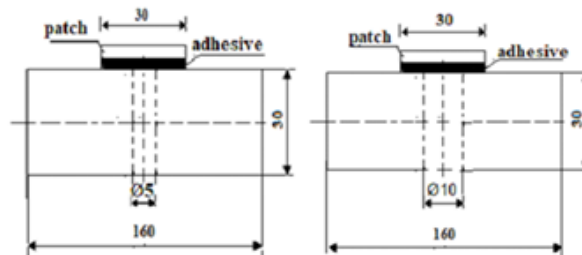


Figure 3. Single patch-repaired specimens (Group III).

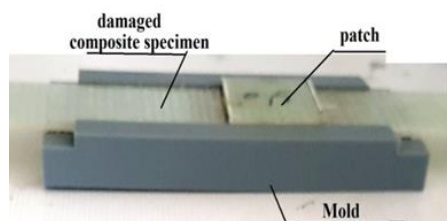


Figure 4. Mold prepared for repaired specimens.

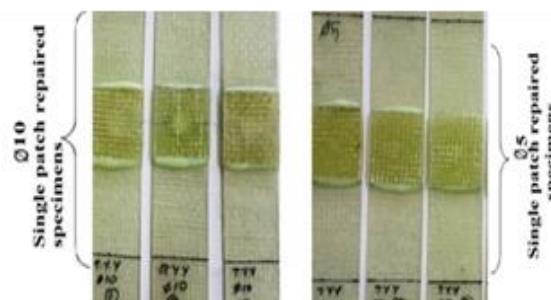


Figure 5. Repaired specimens.

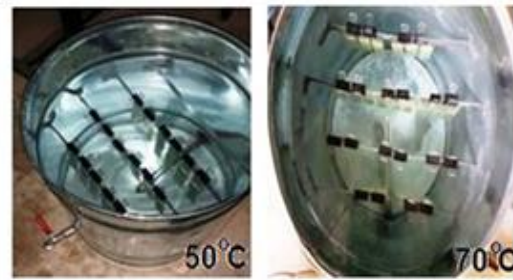


Figure 6. The specimens placed into water boilers fixed at 50°C and 70°C temperatures.

3. Results and Discussion

3.1. Moisture absorption rates of specimens

Before and after placing them into hot water at 50°C and 70°C, the specimens were weighed individually. At the end of 8 and 16 days periods, the excessive water on the specimens taken out of hot water boilers was dried by using a swab. In order to measure the moisture absorption rates of specimens, a 0.01g-sensitive scale was used. The initial weights of specimens (w_0) and the weights of specimens after the application (w_t) were measured, and the moisture absorption rates of each sample (M_t) were calculated using following formula.

$$M_t = [(w_t - w_0) / w_0] \times 100 \quad [30]$$

Figures 7 and 8 represent the moisture absorption rates of specimens in terms of the specimens geometries and duration of keeping in hot water. As can be seen from the figures, it is seen that moisture absorption rates are higher in specimens that are kept for 16 days than specimens that are kept for 8 days. However, when the temperature is 70 °C, the absorption rate is also increased. For example, the moisture absorption of undamaged specimens in 1st group kept in hot water at 50°C for 16 days increased by 46.15% when compared to the specimen kept under the same conditions for 8 days (Figure 7). The moisture absorption rates of specimens kept in hot water at 70°C for 16 days were 22.22% and it was higher than that of specimens kept under the same conditions for 8 days (Figure 8). The moisture absorption rates of specimens having Ø5 mm circular hole damage at the center in 2nd group kept in hot water at 50°C for 16 days were found to increase by 50% when compared to the specimens kept under the same conditions for 8 days (Figure 7). The moisture absorption rates of specimens having Ø10 mm circular hole damage at the center and kept in hot water at 70°C were found to increase by 41.66% (8 days) and 11.11% (16 days) when compared to the moisture absorptions observed after keeping the specimen at 50°C. The moisture absorption rates of single patch-repaired specimens having Ø5 mm circular hole damage at the center in 3rd group kept in hot water at 50°C for 16 days increased by 120% when compared to the specimens kept under the same conditions for 8 days (Figure 7). Similarly, the moisture absorption rates of single patch-repaired specimens having Ø10 mm damage in 3rd group kept in hot water at 70°C increased by 33.33% (for 8 days) and 9.52% (for 16 days) when compared to the specimens kept in hot water at 50°C.

This shows that environmental temperature plays a decisive role in the diffusibility of water molecules in fiber-reinforced composites. At higher temperatures, more filtration of the water into the

matrix of the resin takes place [27]. This is explained by the fact that the moisture absorption rates of the specimens kept in hot water at 70 °C are higher than those kept in hot water at 50 °C.

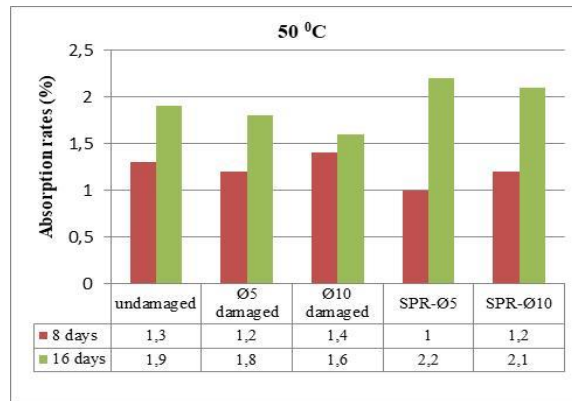


Figure 7. Moisture absorption rates of specimens kept in hot water at 50°C for 8 and 16 days.

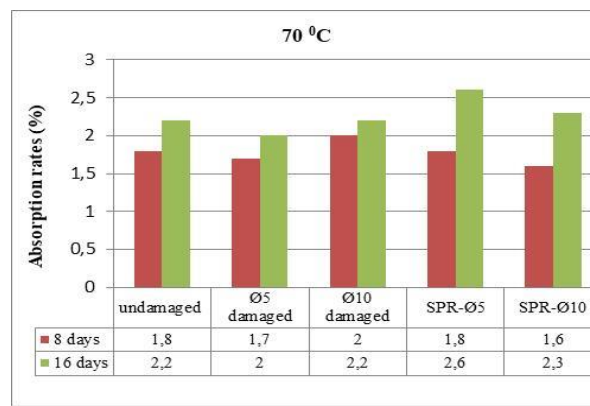


Figure 8. Moisture absorption rates of specimens kept in hot water at 70°C for 8 and 16 days.

3.2. Maximum failure loads of specimens

The specimens were exposed to tensile test at 1mm/min speed by using Instron BS8801 device having the capacity of 100 kN (Figure 9). At the end of hot water ageing period, the excessive water on the surface of each specimen was dried by using a swab, and static tensile test was carried out within 1 hour. The maximum failure load values obtained from 3 specimen groups kept in hot water at 50°C and 70°C for 8 and 16 days were compared to the values obtained from dry specimens and the results of maximum failure load comparisons were presented in Figures 10 and 11. In addition, load-extension curves of the specimens are given in Figures 12,13,14,15 and 16. The results of experiment were expressed as the average values obtained from three specimens.



Figure 9. Tensile test applied to the specimens.

As shown in the load-extension curves and Figures 10,11, the maximum failure loads of the specimens;it is seen that due to the increase in temperature and residence time in hot water, it is lower than the values obtained from dry specimens. For example; the maximum failure load values obtained from the undamaged specimens kept in hot water at 50°C and 70°C for 8 days were observed to decrease by 1.59% and 3.59%, respectively, when compared to the maximum failure load values obtained from the dry and undamaged specimens. Moreover, the maximum failure load values obtained from the undamaged specimens kept in hot water at 50°C and 70°C for 16 days were observed to decrease by 2.39% and 5.98%, respectively, when compared to the maximum failure load values of dry and undamaged specimens (Figures 10,11 and 12).

The maximum failure load values of specimens having Ø5 mm circular hole damage at the center and kept in hot water at 50°C and 70°C for 8 days were found to decrease by 4.78% and 9.89%, respectively,when compared to the maximum failure load values obtained from dry specimens (Figures 10,11 and 13).

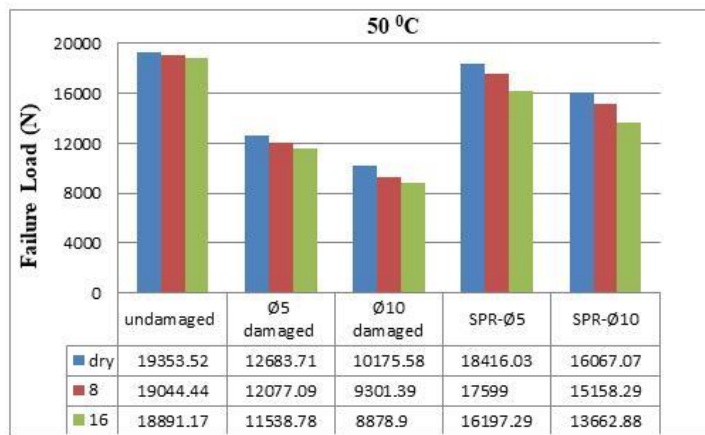


Figure 10. Maximum failure load values of specimens kept in hot water at 50°C.

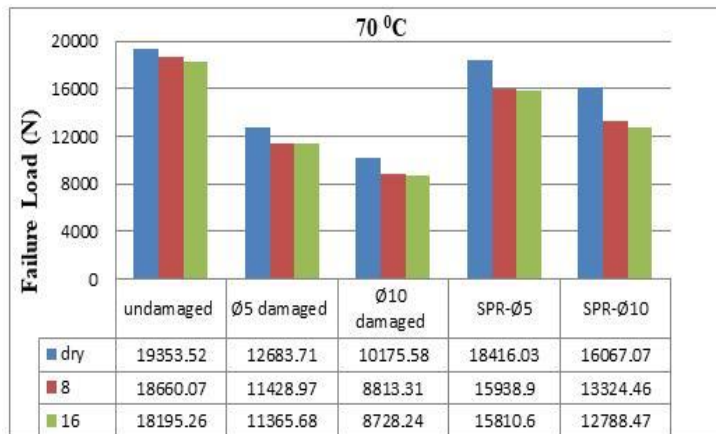


Figure 11. Maximum failure load values of specimens kept in hot water at 70°C.

Moreover, the maximum failure load values of specimens having Ø10 mm circular hole damage at the center and kept in hot water at 50°C and 70°C for 8 days were found to decrease by 8.59% and 13.39%, respectively, when compared to the maximum failure load values of dry specimens (Figures 10,11 and 14).

The maximum failure load values of single patch-repaired specimens having Ø5 mm circular hole damage at the center and kept in hot water at 50°C and 70°C for 8 days were found to decrease by

4.44% and 13.45%, respectively, when compared to the maximum failure load values obtained from dry specimens (Figures 10,11 and 15).

The maximum failure load values of single patch-repaired specimens having $\varnothing 10$ mm circular hole damage at the center and kept in hot water at 50°C and 70°C were observed to decrease by 9.87% and 4.02%, respectively, when compared to the values of specimens kept under the same conditions for 8 days (Figures 10,11 and 16).

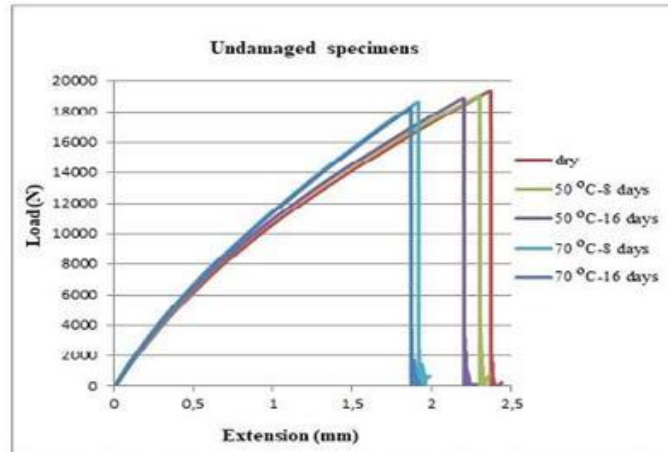


Figure 12. Load-extension diagram of the undamaged specimens.

Polymeric matrixes are susceptible to swelling caused by water absorption in composite structures. This causes swelling stresses. These stresses are the cause of the formation of micro-cracks, particularly during the transition phase. In most cases, the degradation of a composite material during wet aging causes a phenomenon of water absorption due to temperature, hygrometric speed and the nature of the composite. The transport of water can be facilitated by differentiating within the matrix by imperfections in the matrix formed during manufacture or by capillarity along the fiber / matrix interface. As a result, these microfractures adversely affect the mechanical properties of the material [27].

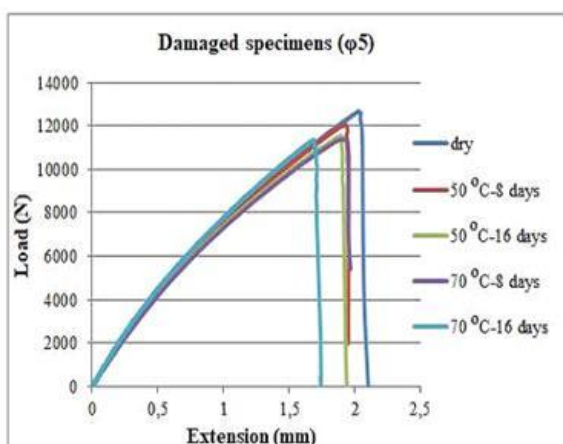


Figure 13. Load-extension diagram of damaged specimens ($\varnothing 5$).

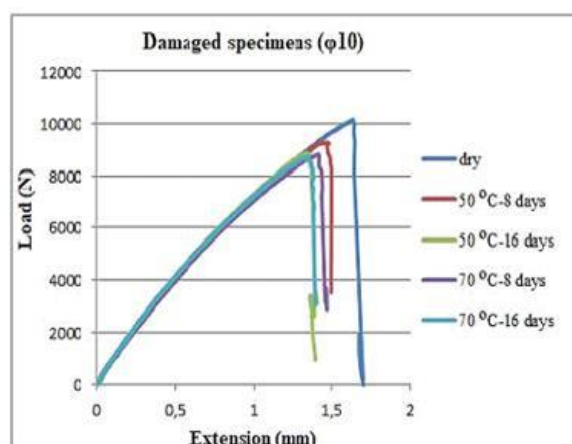


Figure 14. Load-extension diagram of damaged specimens ($\varnothing 10$).

Hydrothermal degradation due to temperature and moisture absorption at the fiber-matrix interface also leads to weakened fiber / matrix interface bonds. When these bonds are damaged, both the ability to transmit forces to the fibers and the homogeneity of the load distribution between the fibers are expected to be interrupted [27]. In this study, this is explained by the increase of the temperature of the water and the waiting times of the hot water and the decrease of the maximum load of the specimens.

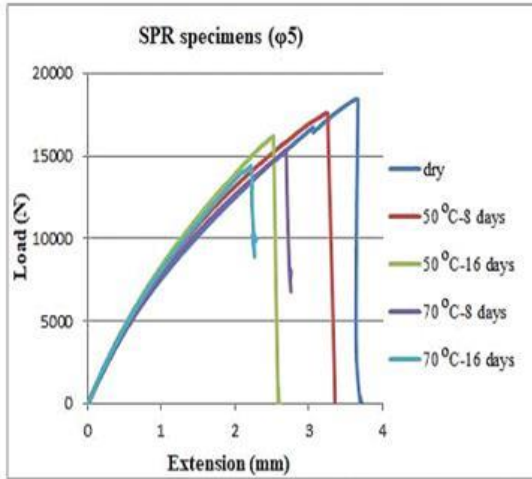


Figure 15. Load-extension diagram of repaired specimens (Ø5).

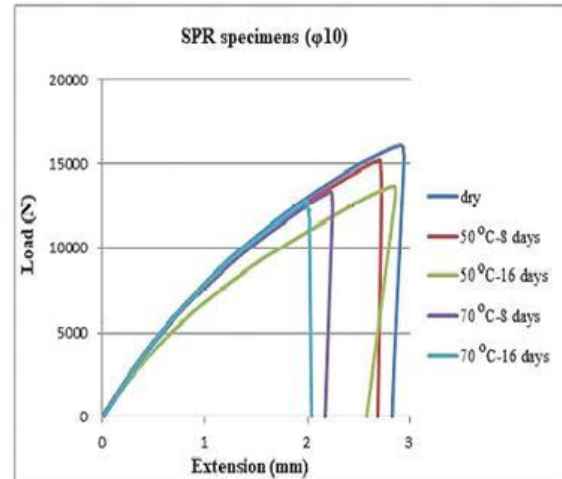


Figure 16. Load-extension diagram of repaired specimens (Ø10).

3.3. Failure mode of specimens

The failure modes of specimens, which were kept in hot water at 50°C and 70°C, were observed at the end of tensile test and these modes are shown in Table 1.

Table 1. Observed failure modes

| Waiting times | Failure Modes | | | | | | | |
|----------------|---------------|------|-------------|------|---------|--------|----------|--------|
| | Ø5 damaged | | Ø10 damaged | | SPR- Ø5 | | SPR- Ø10 | |
| | 50°C | 70°C | 50°C | 70°C | 50°C | 70°C | 50°C | 70°C |
| 0 | NT | NT | NT | NT | CF+LFT | CF+LFT | CF+LFT | CF+LFT |
| 8 days | NT | NT | NT | NT | CF+LFT | CF+LFT | CF+LFT | CF+LFT |
| 16 days | NT | NT | NT | NT | CF+LFT | CF+LFT | CF+LFT | CF+LFT |

The failure modes of some of specimens are also illustrated in Figures 17 and 18. The Net-Tension failure mode was observed when the damaged specimens of 2nd group were kept dry and in hot water at 50°C and 70°C for 8 days (Figure 17) and 16 days (Table 1). Among the single patch-repaired specimens, it was determined that the mixed-type damages occurred, that the adhesive joint broke especially on single side (cohesive failure), on which the patch was attached, and that the other side was undamaged. In this cohesive failure site, also the fiber damage (LFT failure) was observed at low level on the adhesion layer of adhesive bond. On the side, on which no patch was attached, it was observed that the damage started around the hole, and that the net-tension damage occurred but it did not split from the patch (Figure 18).

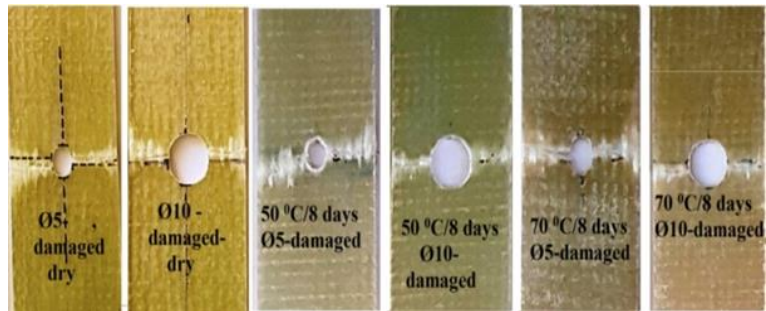


Figure 17. Net-Tension damage images of dry form of damaged specimens and specimens kept in hot water at 50°C/70°C for 8 days.

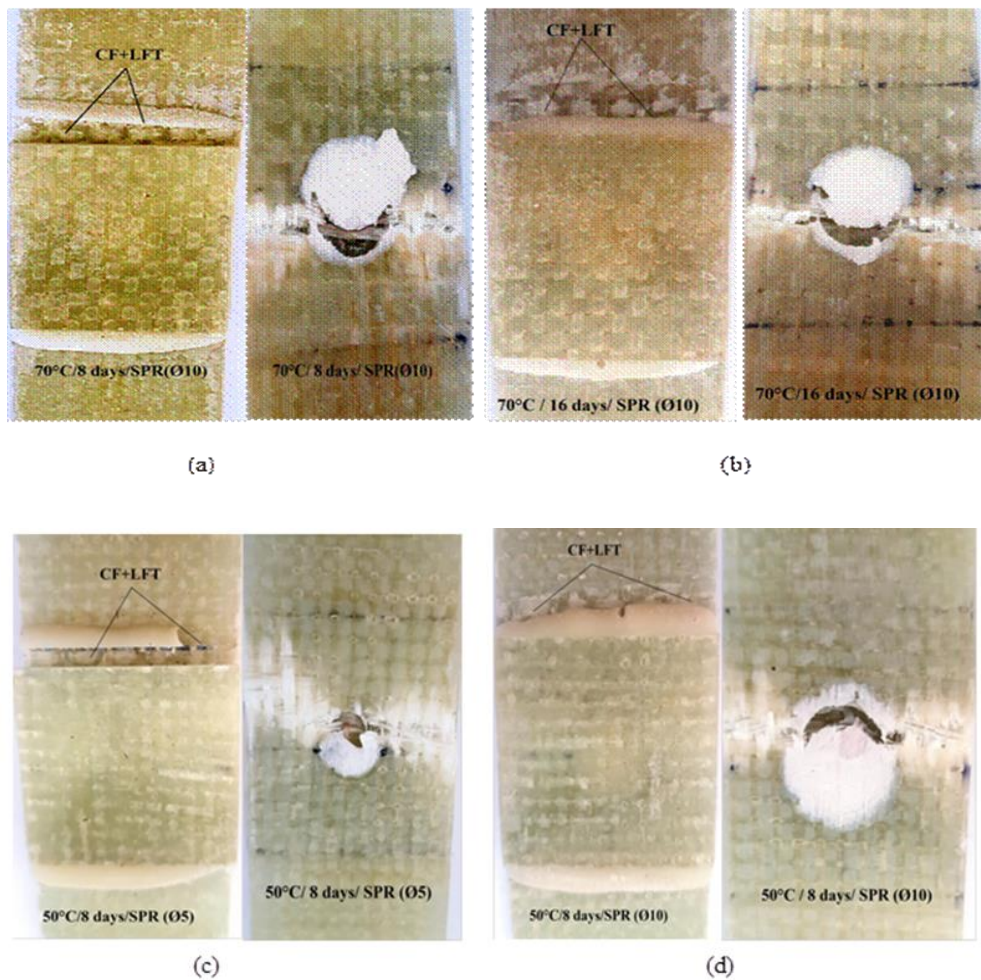


Figure 18. Damage images of patched (front) and unpatched (back) sides of repaired (Ø10, Ø5) specimens kept in hot water at 50°C and 70°C for 8 and 16 days.

4. Conclusions

In this study, the effects of hot water ageing on the woven glass fiber reinforced epoxy composites were examined experimentally. The undamaged, damaged, and repaired specimens were

kept in hot water at 50°C and 70°C for 8 and 16 days. At the end of hot water ageing period, the moisture absorption rates, maximum failure load values, and failure modes of specimens were determined and compared. At the end of this study, the following conclusions were made;

- It was found that the maximum failure load values of damaged specimens increased after repairing with patch. The resistance of damaged specimen having Ø5 mm circular hole damage at the center increased by 45.19% after being repaired with single patch. For the damaged specimens having Ø10 mm circular hole damage at the center, the strength increased by 57.89% after repairing by using single patch.

- The minimum failure loads were obtained from the specimens having Ø10 mm circular hole damage at the center, whereas the maximum failure loads were observed among the undamaged specimens.

- The specimens kept in hot water at 70°C for 16 days were observed to show maximum moisture absorption values when compared to the other environmental conditions.

- It was found that when the waiting times of composite samples in hot water and the temperature of water increased, the amount of moisture absorption increased but the failure load values were decreased.

- It was also seen that generally the same failure modes were observed among the specimens under all conditions.

Nomenclature

| | |
|-----|----------------------------------|
| SPR | : Single patch-repaired specimen |
| NT | : Net Tension |
| CF | : Cohesive Failure |
| LFT | : Light-Fiber Tear Failure |

References

- [1] Campilho, R.D.S.G., Moura, M.F.S.F., Domingues, J.J.M.S. (2009). Numerical prediction on the tensile residual strength of repaired CFRP under different geometric changes. *International Journal of Adhesion & Adhesives*, 29, 195–205.
- [2] Campilho, R.D.S.G., Mmnoura, M.F.S.F., Domingues, J.J.M.S. (2005). Modelling single and double-lap repairs on composite materials. *Composites Science and Technology*, 65, 1948–1958.
- [3] Toudeshky, H. H., Mohammadi, B.(2009).Mixed-mode numerical and experimental fatigue crack growth analyses of thick aluminium panels repaired with composite patches. *Composite Structures*, 91, 1–8.
- [4] Toudeshky, H. H., Mohammadi, B., Daghyani, H. R. (2006). Mixed-mode fracture analysis of aluminium repaired panels using composite patches. *Composites Science and Technology*, 66, 188–198.
- [5] Toudeshky, H.H.(2006).Effects of Composite Patches on Fatigue Crack Propagation of Single-side Repaired Aluminum Panels. *Composite Structures* ,76, 243–251.
- [6] Oudad, W., Bouiadjra, B. B., Belhouari, M., Touzain, S. , Feugas, X. (2009). Analysis of the plastic zone size ahead of repaired cracks with bonded composite patch of metallic aircraft structures. *Computational Materials Science*, 46, 950–954.

- [7] Ouinas, D., Bouiadjra, B.B., Serier, B., Bekkouche, M. S.(2007). Comparison of the effectiveness of boron/epoxy and graphite/epoxy patches for repaired cracks emanating from a semicircular notch edge. *Composite Structures*, 80, 514–522.
- [8] Ouinas, D., Sahnoune, M., Bebdouche, N., Bouiadjra, B.B. (2009). Stress Intensity Factor Analysis for Notched Cracked Structure Repaired by Composite Patching. *Materials and Design*, 30, 2302–2308.
- [9] Bouiadjra, B. B., Belhouari, M., Serier, B. (2002). Computation of the stress intensity factors for repaired cracks with bonded composite patch in mode I and mixed mode. *Composite Structures*, 56, 401–406.
- [10] Bouiadjra, B.B., Rezgani, L., Ouinas, D., Belhouari, M. , Ziadi, A.(2007). Numerical Analysis of the Notch effect and the Behaviour of Notch Crack in Adhesively Bonded Composite Laminates. *Computational Materials Science*. 38, 759–764.
- [11] Papanikos, P., Tserpes, K.I., Pantelakis, Sp.(2007). Initiation and progression of composite patch debonding in adhesively repaired cracked metallic sheets. *Composite Structures*, 81, 303–311.
- [12] Umamaheswar, T.V.R.S.(1999). Singh, R., Modelling of a patch repair to a thin cracked sheet. *Engineering Fracture Mechanics*, 62, 267-289.
- [13] Charalambides, M.N., Hardouin, R., Kinloch, A.J., Mathews, F.L.(1998). Adhesively-bonded Repairs to Fibre-composite Materials I: Experimental. *Composites Part A*, 29A, 1371-1381.
- [14] Achour, T., Bouiadjra S. B.(2003). Numerical Analysis of the Performances of the Bonded Composite Patch for Reducing Stress Concentration and Repairing Cracks at Notch. *Computational Materials Science*, 28, 41–48.
- [15] Tsouvalis N.G., Mirisiotis, L.S.N.(2008). Experimental Investigation of the Static Behaviour of a Hole Drilled Steel Plate Reinforced with a Composite Patch. *Strain*, 44, 133–140.
- [16] Her, S.C., Chao, M.(2011). Adhesively Bonded Patch Repair of Composite Laminates. *Journal of Adhesion Science and Technology*, 25, 2569–2585.
- [17] Madani, K., Touzain, S., Feugas, X., Benguediab, M., Ratwani, M.(2008). Numerical analysis for the determination of the stress intensity factors and crack opening displacements in plates repaired with single and double composite patches. *Computational Materials Science*, 42, 385–393.
- [18] Ridha, M., Tan, V.B.C., Tay, T.E.(2011). Traction–separation laws for progressive failure of bonded scarf repair of composite panel. *Composite Structures*, 93, 1239–1245.
- [19] Liu, X., Wang, G.(2007). Progressive failure analysis of bonded composite repairs. *Composite Structures*, 81, 331-340.
- [20] Turan, K., Örcen, G.(2017). Failure analysis of adhesive-patch repaired edge-notched composite plates. *The Journal of Adhesion*, 93:(4), 328-341.
- [21] Park, Y.B., Song, M.G., Kim, J.J., Kweon, J.H., Choi, J.H.,(2010). Strength of carbon/epoxy composite single-lap bonded joints in various environmental conditions. *Composite Structures*, 92 (9), 2173–2180.

- [22] Walker, S.P.(2004). Thermal effect on the compressive behavior of IM7/PET15 laminates. *J Compos Mater*, 38, 149–162.
- [23] Bismarck, A., Hofmeier, M., Dörner, G.(2007).Effect of hot water immersion on the performance of carbon reinforced unidirectional poly(ether ether ketone) (PEEK) composites: stress rupture under end-loaded bending. *Composites Part A*, 38, 407–426.
- [24] Parker, B.M.(1986).Some effects of moisture on adhesive-bonded CFRP–CFRP joints. *Composite Structures*, 6, 123–139.
- [25] Ashcroft, I.A., Hughes, D.J., Shaw, S.J.(2000).Adhesive bonding of fiber reinforced polymer composite materials, *Assembly Autom*,20, 150–161.
- [26] Akderya, T., Kemiklioglu, U., Sayman, O.(2016).Effects of thermal ageing and impact loading on tensile properties of adhesively bonded fibre/epoxy composite joints.*Composites Part B*, 95, 117-122.
- [27] Soykok, I.F.Degradation of single lap adhesively bonded composite joints due to hot water ageing.*The Journal of Adhesion*, <http://dx.doi.org/10.1080/00218464.2015.1076340>.
- [28] Zhang, F., Wang, H.P., Hicks, C., Yang, X., Carlson, B. E., Zhou, Q. (2013). Experimental study of initial strengths and hygrothermal degradation of adhesive joints between thin aluminum and steel substrates. *International Journal of Adhesion & Adhesives*, 43, 14–25.
- [29] ASTM Standart D5868-01.1995, Standart Test Method for Lap Shear Adhesion for Fiber Reinforced Plastic (FRP) Bonding, ASTM International, West Conshohocken,PA,2014,DOI: 10.1520/D5868-01R14,www.astm.org.
- [30] Assarar, M., Scida, D., El Mahi, A., Poilâne , C., Ayad, R.(2011). Influence of water ageing on mechanical properties and damage events of two reinforced composite materials: Flax–fibres and glass–fibres.*Materials and Design*, 32,788–795.

THE PROPERTIES OF CADMIUM OXIDE-CARBON NANOTUBE NANOCOMPOSITE SYNTHESIZED VIA SOL-GEL METHOD

Öyküm BAŞGÖZ¹, Ömer GÜLER^{2*}, M. Gökhan ALBAYRAK³, Mehmet TAKGÜN⁴

In this study, cadmium oxide based carbon nanotube reinforced material was produced and the optical and electrical properties of the obtained composite were investigated. After the carbon nanotubes used as reinforcement material were synthesized using the chemical vapor deposition method, they were supplemented at different ratios to the commercially available cadmium oxide powders. As another group of samples; cadmium oxide powders were synthesized by the sol-gel method and the carbon nanotubes were again supplemented at different ratios. Synthesized carbon nanotubes were subjected to Transmission Electron Microscope examination. Composite materials obtained were examined by Scanning Electron Microscope. Then, the changes in the electrical conductivity of the composites obtained by temperature were measured. The optical properties of the composites were determined by taking UV-vis spectrometers.

Key words: *Carbon Nanotube, Cadmium Oxide, Sol-Gel, Nanocomposite.*

1. Introduction

In recent years, the application areas of metal oxides have grown to a large extent due to their new electrical, catalytic and optical properties, so researchers primarily work with these materials because of their optical and structural properties of metal oxides [1-4]. Transparent oxide conductors such as copper oxide (CuO), zinc oxide (ZnO), tin oxide (SnO) and cadmium oxide (CdO) are of interest due to their semiconductor optoelectronic properties (transparent in the visible region and electrically conducting) [5]. CdO is an n-type semiconductor. It has 2.2 - 2.8 eV direct and 0.55 eV indirect band gap and is used in many applications such as photodiode, solar cells in the result of low electrical resistance, high optical transparency [6-8]. CdO is n-type semiconductors in the rock salt crystal structure of NaCl (surface-centered cubic structure) [9]. Since CdO-structured semiconductors have an extraordinarily large carrier mobility in the visible region and good optical transparency, their use is increasing [10-12].

¹ Mersin University, Engineering Faculty, Metallurgical and Materials Eng. Dept., 33100, Mersin, Turkey oykumbasgoz@mersin.edu.tr

² Mersin University, Engineering Faculty, Metallurgical and Materials Eng. Dept., 33100, Mersin, Turkey, oguler@mersin.edu.tr, <http://orcid.org/0000-0003-0190-9630>

³ Firat University, Engineering Faculty, Metallurgical and Materials Eng. Dept., 23000, Elazig, Turkey mgalbayrak@firat.edu.tr

⁴ Firat University, Engineering Faculty, Metallurgical and Materials Eng. Dept., 23000, Elazig, Turkey mehmet_takgun@hotmail.com

* Corresponding author; oguler@mersin.edu.tr,

CdO is used in making photodiodes, solar cells, flat panel displays, optical communication, thin film resistors, phototransistors, photovoltaic, transparent conductive electrodes, liquid crystal displays and IR detectors due to their high conductivity, high permeability and low band gap properties [13-15]. The physico - chemical properties of CdO depend not only on chemical composition but also on size, shape, surface morphology and production technique [16]. There are many different methods for producing CdO in the literature. As a result of these methods, CdO acquisition at nano size is made possible. Physical, chemical and thermal hydrothermal methods [17-18], template assisted method [19], solvothermal method [20], mechanochemical method [21-22], thermal disruption method [23], photosynthetic method [24] sonochemical method [25] are production methods. Sol-gel technique for preparing pure and doped CdO films is a cost-effective method of controlling size and morphology [26], and nanoparticles are one of the most promising methods for synthesizing nanoparticles.

The idea of doping carbon nanotubes has attracted the attention of researchers because it allows them to control their electronic properties (intercalation reaction with electron donors or recipients) [27]. In addition, the absence of certain band voids in MWCNT provides added value to photovoltaic efficiency by absorbing light over a broad wavelength range [28]. Isolated CNTs have an electrical conductivity of $2 \times 10^7 \text{ s / m}$, a capacitance of 10^{13} A / m^2 and a thermal conductivity of 3500 W / mK [29].

The purpose of this work is to reinforce the above mentioned CNTs with very good electrical properties by using two different cadmium oxide matrices and to examine the change in electrical and optical properties that will occur in the structure compared to pure CdO.

2. Material and Method

In this study, CdO synthesized by sol-gel method was used as matrix. CNTs synthesized by Chemical Vapor Deposition (CVD) method were used as reinforcement material and nanocomposites with CdO matrix were synthesized by powder metallurgy method. Carbon nanotube synthesis was performed using a single crystal silicon (100) substrate. This substrate was first washed with acetone followed by ethanol in an ultrasonic bath. Then, the substrate was placed in the middle of a tube furnace on a boat, the inside of the tube furnace was vacuumed with a pump and purged. The furnace was then heated to $650 \text{ }^\circ\text{C}$ in an argon (Ar) atmosphere at a flow rate of 1 liter per minute through the system. After the tube furnace reached $650 \text{ }^\circ\text{C}$, the flow of Ar gas was interrupted and acetylene (C_2H_2) gas was introduced for 40 minutes. At the end of 40 minutes, the acetylene gas was cut off and the Ar gas was again supplied to the system until the furnace cooled to room temperature. Characterization of the obtained nanotubes was performed by X-ray diffraction (XRD) and transmission electron microscopy (TEM). Jeol Jem 2100 F brand TEM device was used.

Carbon nanotubes were added to the CdO synthesized by the sol-gel method at 0.1, 0.2, 0.5 and 1 % by weight. For a homogenous mixture, the alcohol carbon nanotube mixture was mixed in an ultrasonic mixer and then the appropriate amount of CdO was added. The alcohol was mixed with a magnetic stirrer until evaporation. The resulting powder mixture was pelletized by pressing at a pressure of 600 MPa and then sintered at $450 \text{ }^\circ\text{C}$. In order to compare the properties of the sol-gel produced CdO, the Acros Organic brand (Code: 223792500, 99% purity) CdO was readily available. The production of the H₁-encoded nanocomposite with the ready CdO matrix was similarly performed and compared with the CdO-matrix nanocomposite synthesized by the sol-gel method.

Table 1. Codes and other characteristics of samples.

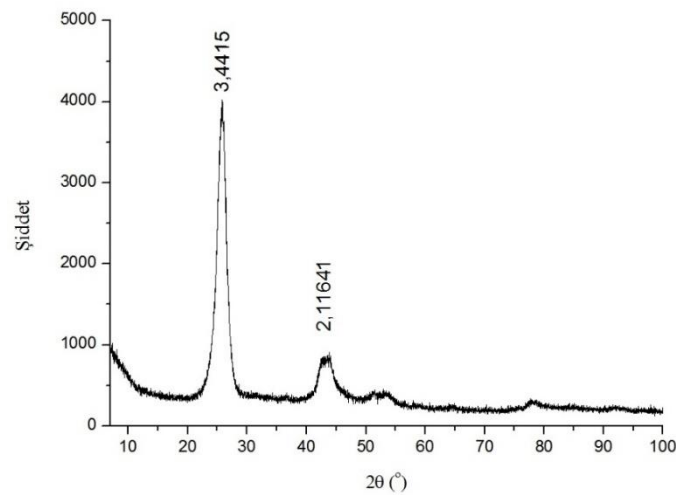
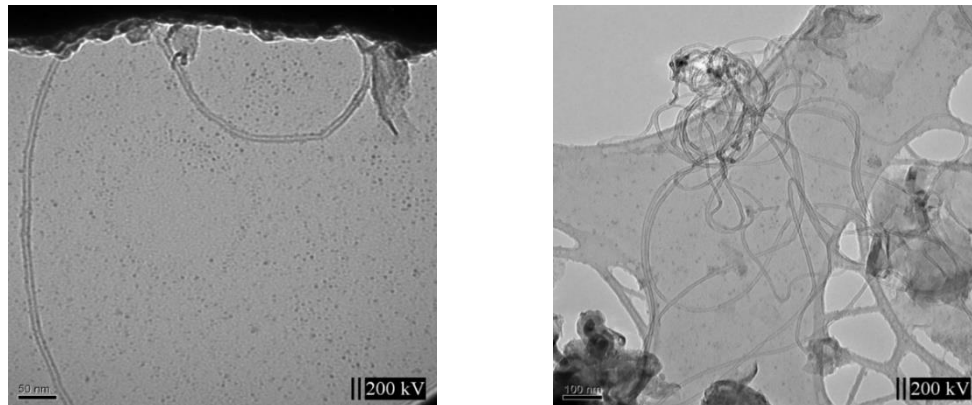
| Samples Codes | The type of CdO | The amount of CNT (% w) |
|----------------|-----------------|-------------------------|
| H ₁ | Commercial | - |
| S ₁ | Sol-Gel | - |
| S ₂ | Sol-Gel | 0.1 |
| S ₃ | Sol-Gel | 0.2 |
| S ₄ | Sol-Gel | 1 |

2.1. Production of Carbon Nanotubes

Fig. 1 shows the XRD analysis of carbon nanotubes produced by the chemical vapor deposition method. As can be seen, the powders gave both a violent and broad peak at about 26°, which overlaps with the peaks of the carbon nanotubes in the database of the XRD (Pixel analysis Diffrac Evaluation Software ICDD tag No. 00-058-1638). The fact that the pikes are wide indicates that the powders are nano-sized according to Debye-Scherrer equality. Debye-Scherrer equality;

$$D=0.9 \lambda / \beta_{hkl} \cos\theta$$

D is the crystal size, B is the maximum peak intensity half-peak width in radians, θ is the Bragg angle, λ is the wavelength of the light used in the diffraction [29].

**Figure 1. XRD analysis results of carbon nanotubes produced.****Fig. 2. TEM Images of the produced carbon nanotubes.**

TEM images of the carbon nanotubes produced in Fig. 2 are given. As can be seen, the structures obtained are carbon nanotubes. There is a gap in the middle of the structures obtained, and on both sides there are walls with certain thicknesses. The produced carbon nanotubes vary in diameter from 15 to 20 nm and vary in size from 1-5 μm .

Some particles have black particles in the joint or tip (Fig. 2.b). These particles are nano-sized iron particles that have been used as catalysts during the synthesis of carbon nanotubes. Carbon nanotubes grow on these particles.

2.2. Production of CdO with Sol-Gel

For synthesis, 1 mole of cadmium acetate dihydrate was used, 46 moles of methanol, 0.2 moles of glycerol and 0.5 moles of triethylamine. Firstly, cadmium acetate was dissolved in 23 moles of methanol using a magnetic stirrer. Stirring is carried out until the mixture has a transparent color. Glycerol was added and then triethylamine and the remaining methanol mixture added. The whole mixture was stirred at 60 °C for 2 hours in a magnetic stirrer. The mixture was stirred at room temperature for 12 hours in a magnetic stirrer to obtain a homogeneous mixture. Calcination heat treatment was applied in order to remove the solvent in the thoroughly homogenized solutions by mixing. The resulting powder mixture was calcined at 600 °C for 1 hour and a brown powder was obtained at the end of the treatment. The flow chart of the method mentioned in Fig. 3 is given.

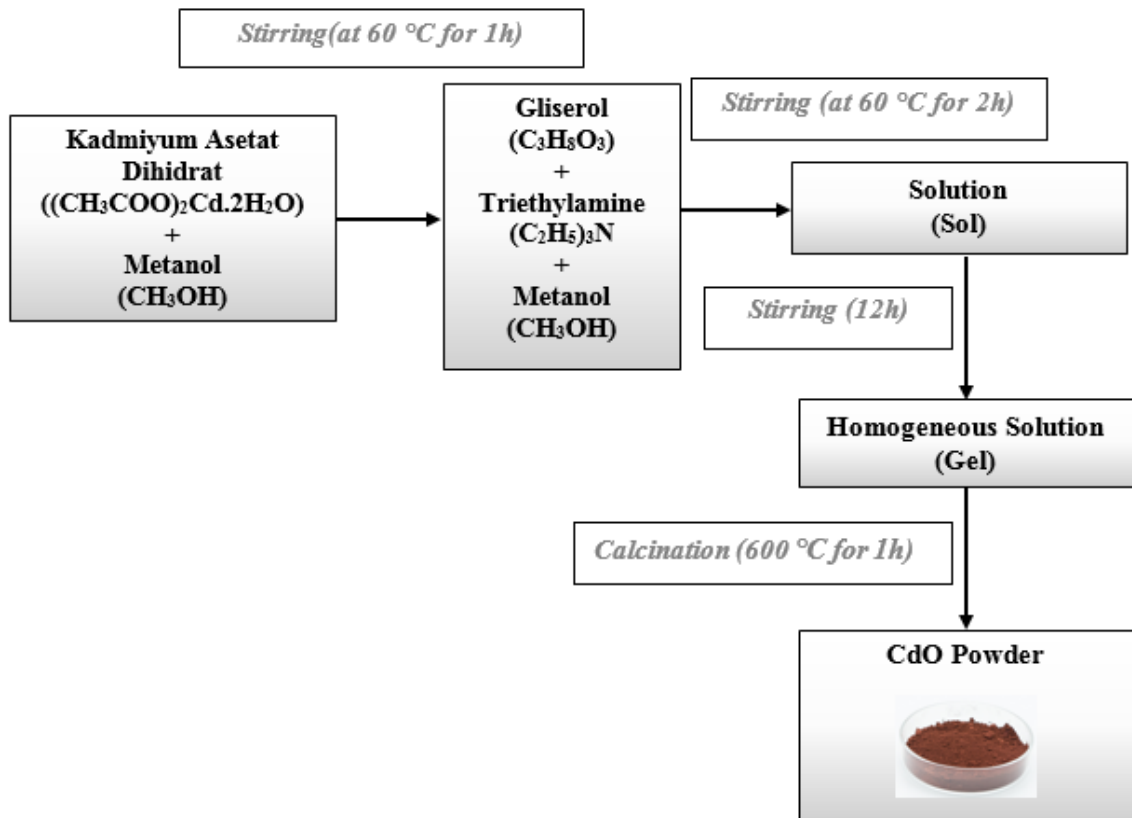


Figure 3. CdO synthesis flow diagram by sol-gel method.

3. Result and Discussion

3.1. Microstructure Examination Results of CdO-KNT Composite

Microstructures of the resulting composites were determined by scanning electron microscopy. Jeol Jsm 7001 F electron microscope used in this study was used. In Figure 3, microstructure images of H_1 sample and S_x series are given.

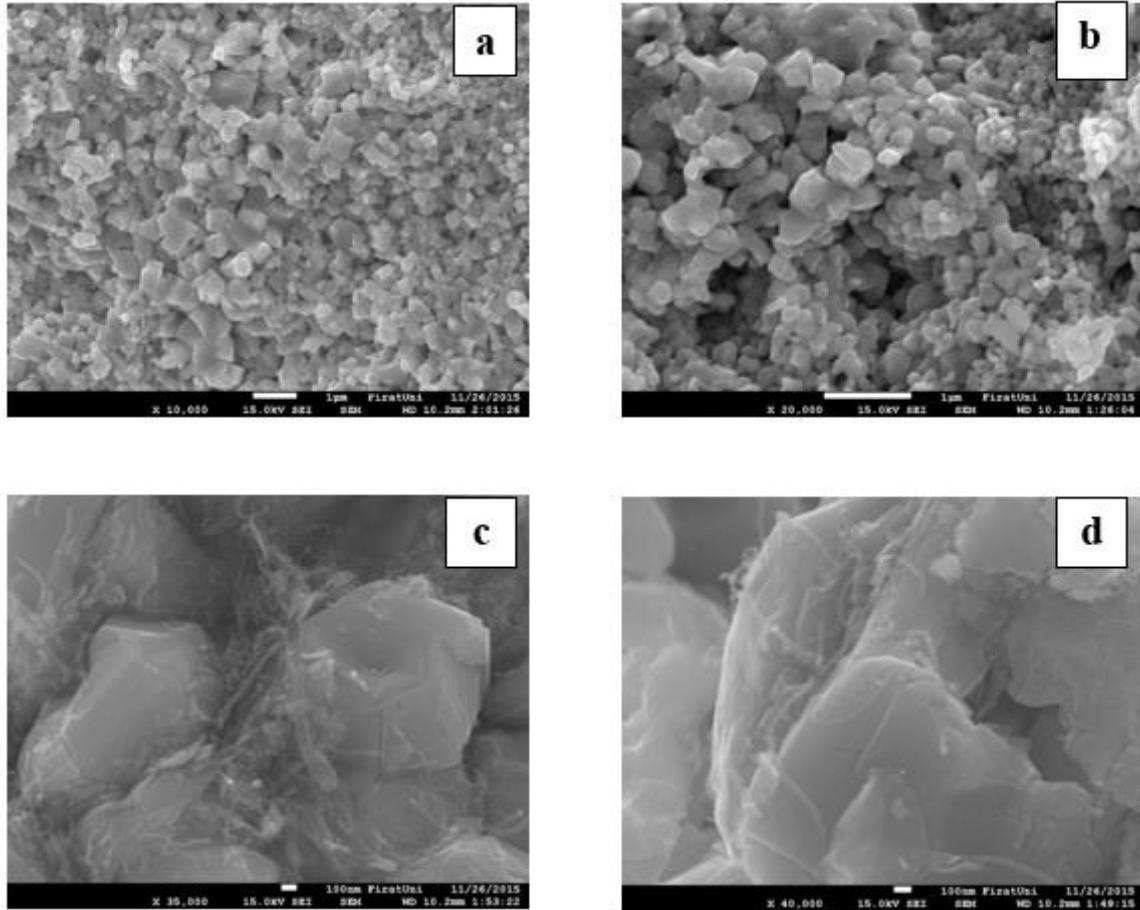


Figure 4. Microstructure images of H_1 sample and S_x series. a) H_1 , b) S_1 , c) S_2 , d) S_4 samples.

Figure 4.a gives a SEM image of sample H_1 . The H_1 sample is commercially available pure CdO. When the microstructure images are examined, a structure consisting of many particles in homogeneous and close to each other is seen.

In Figure 4.b, SEM image of S_1 sample is given. Sample S_1 is pure CdO produced by the sol-gel method. The structures formed as shown are homogeneous spherical shaped particles, the size of the particles being around 100 nm.

Figure 4.c shows a SEM image of sample S_2 . The sample S_2 is a CdO matrix 0.1 % CNT reinforced composite sample produced by the sol-gel method. It can be said that the CNTs are distributed homogeneously within the structure. In addition, there were not CNT pellets found in the structure.

In Figure 4.d, a SEM image of sample S_4 is given. S_4 sample is a composite sample of CdO matrix 1 % CNT reinforced by the sol-gel method. Although there are homogeneously distributed regions of CNTs in the structure, it is not uncommon to find the regions where the CNTs are scattered and clustered as in the H_5 sample.

3.2. Investigation of Electrical Properties of CdO-KNT Composite Samples Produced

The conductivity of the produced semiconducting samples was changed according to the temperature by applying the temperature values in the range of 300-433 K by applying 0,5-5 V current in a dark environment. KEITHLEY 6517A electrometer was used to measure the current values of the samples according to the temperature. Figure 4 shows the electrical conductivity measurements of samples S₁, S₂, S₃ and S₄ respectively.

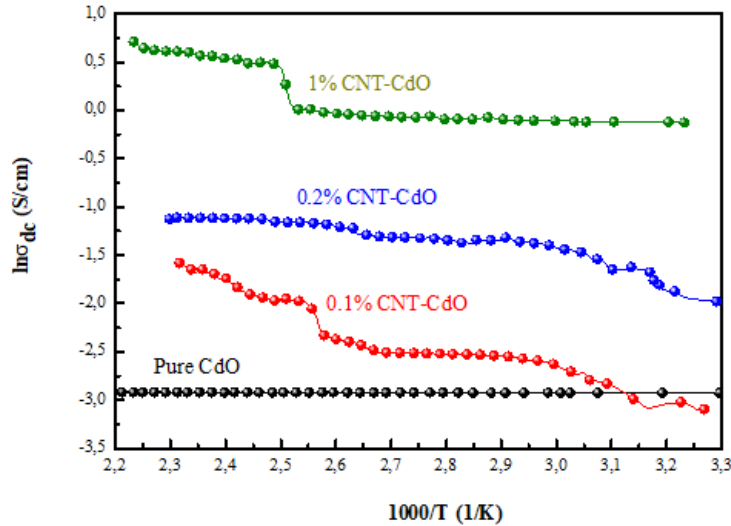


Figure 5. Electrical properties of composites of S_x samples.

Conductivity values of pure CdO, 0.1%, 0.2 and 1 CNT doped CNT-CdO composites at room temperature were found to be 5.37×10^{-2} , 4.9×10^{-2} , 1.44×10^{-1} and 8.8×10^{-1} S/cm, respectively. These values show that the conductivity at room temperature of the composite increases with increasing KNT ratio compared to pure CdO.

3.3. Investigation of Optical Properties of CdO-CNT Composite Samples Produced

In Fig. 6, reflection-wavelength spectrum graphs of CdO and S₁, S₂, S₃ and S₄ samples with 0.1, 0.2 and 1 CNT added by sol-gel method are given. ,

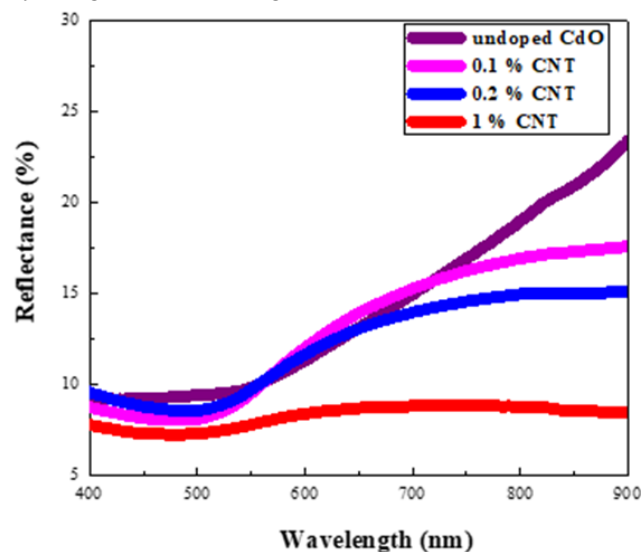


Figure 6. Reflection-wavelength spectrum of S_x series samples.

In Fig. 6, reflectance values were measured (%) for all samples between 400-900 nm wavelengths. Reflectance values of CNT-doped samples decreased in the reflection-wavelength spectrum graph shown in Figure 6. An increase in reflectance values is observed after 500 nm wavelength range when the S_x series exhibits similar reflectance characteristics at a wavelength range of 400-500 nm. However, a lesser increase is observed in the sample of 1% CNT added compared to the others. It might be that the reason for this is due to the increase in the rate of CNT in the structure and the difficulty in homogeneous distribution. The S_1 has the highest reflectance value and the S_4 has the lowest reflectance value.

In Fig. 7, a graph of the change of the S_x series $(ahv)^2$ according to $h\nu$ (photon energy) is given.

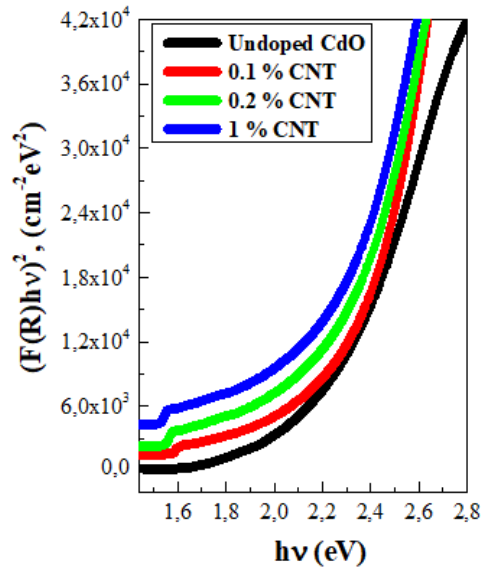


Figure 7. A Graph of The Change of The S_x Series $(ahv)^2$ According to $h\nu$ (Photon Energy).

To determine the bandgap values of CNT doped and undoped CdO nanowires, optical absorption method was used on diffuse reflectance. The Kubelka-Munk function transforms the reflectance values into absorbance. The Kubelka-Munk theory is usually used to analyze the diffuse reflectance spectra obtained from samples with low absorbance. The Kubelka-Munk formula can be expressed by the following relation:

$$F(R) = (1-R)^2 / 2R$$

Where R represents the diffuse reflectance. F (R) is the Kubelka-Munk function corresponding to the absorbance. F (R) values were converted to linear absorption coefficient with the following relation.

$$\alpha = F(R)/t = \text{Absorbance}/t$$

Here t is the thickness of the sample. It is estimated that CdO has a direct optical band gap (bandgap). Thus, the optical band gaps of the CdO samples can be determined using the following relationship.

$$\alpha h\nu = C(h\nu - E_g)^{1/2}$$

$$D = 0.9 \lambda / \beta_{hkl} \cos\theta$$

C is a constant, α absorbance coefficient, and $h\nu$ is the photon energy. $h\nu$ (photon energy) versus $(ahv)^2$ graph, optical absorption method and equation 5. Equation 3 is used when the crystal size of the samples is determined using the Debye-Scherrer relationship. Where D is the crystal size, β_{hkl} is the

peak width of half maximum density, θ is the diffraction angle and λ is the wavelength of the X-ray [30, 31]. The bandgap values calculated in this way are given in Table 2.

Table 2. Sample contents and E_g values.

| Sample Code | The type of CdO | Amount of CNT (% w) | E_g (eV) |
|----------------|-----------------|---------------------|------------|
| H ₁ | Commercial | - | 1,75 |
| S ₁ | Sol - Gel | - | 1,88 |
| S ₂ | Sol - Gel | 0,1 | 2,02 |
| S ₃ | Sol - Gel | 0,2 | 1,93 |
| S ₄ | Sol - Gel | 1 | 1,84 |

The bandgap values calculated in Table 2 don't show a decrease or increase parallel to the contribution of CNT. CdO produced by the sol-gel method seems to have a wider E_g value when compared to CdO produced by the ready-made CdO and the left-handed CdO.

3.2. Comparison of Electrical and Optical Properties of Commercial and Sol-Gel Produced CdO Matrix Composites

Comparative graphs were drawn to investigate how the properties of the CdO-matrix composite synthesized by the sol-gel method are changed from electrical and optical point of view compared to commercially available CdO. In Figure 8, comparative electrical conductivity plots of samples S₁ and H₁ are given.

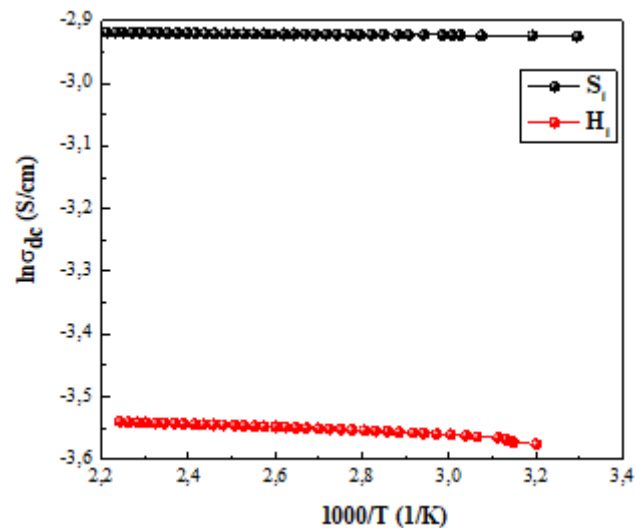


Figure 8. Electrical Properties of the Composites Of Samples S₁ -H₁.

The graph of Figure 8 clearly shows that the CdO (S₁) synthesized by the sol-gel method has better electrical properties than the ready-supplied CdO (H₁). Figure 9 shows the reflection-wavelength spectrum graph of samples S₁ and H₂.

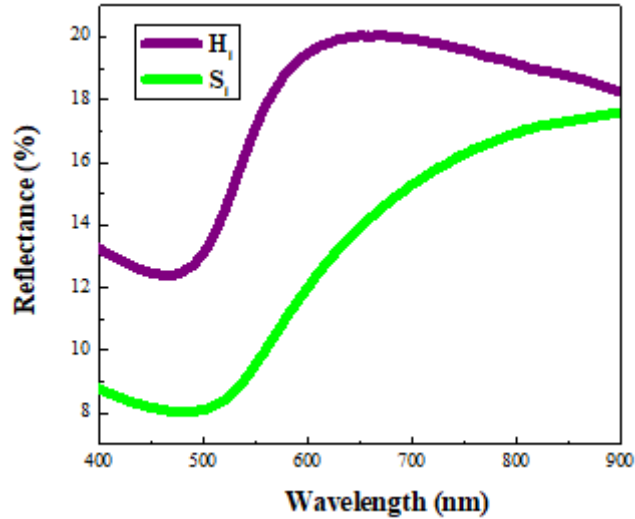


Figure 9. Reflection-Wavelength Spectrum of S_1 - H_1 Samples.

The H_1 sample provided at 400-500 nm wavelengths has a higher reflectance value than the S_1 sample synthesized by the sol-gel method. A sharp increase in the reflectance value is observed after 500 nm for sample S_1 . The CdO synthesized by the sol-gel method exhibits low reflectance at low wave lengths and almost the same reflectance value at 900 nm wavelength as supplied.

Figure 10 shows a graph of the change of H_1 (photon energy) of samples (S_1H_1) of samples S_1 - H_1 .

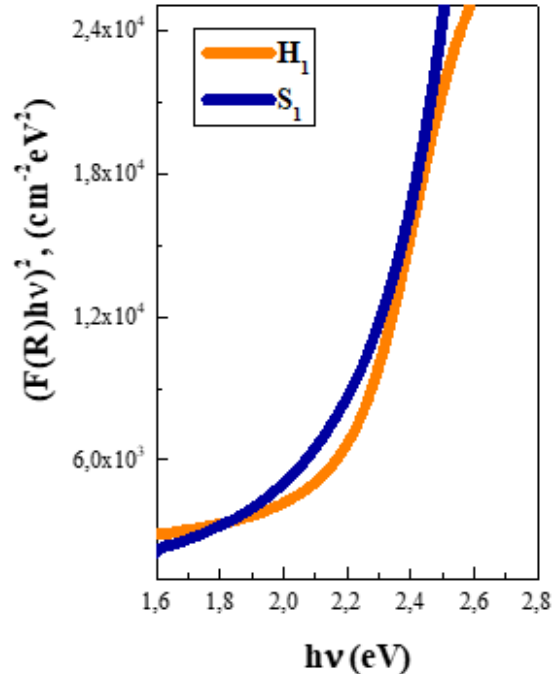


Figure 10. S_1 - H_1 samples $(\alpha hv)^2 \sim hv$ (photon energy) change graph.

The E_g value of the H_1 sample was 1.75 eV while the E_g value of the S_1 sample was 1.88 eV. It has been found that CdO synthesized by the sol-gel method broadens the bandgap value.

4. Conclusions

Using the CVD method, carbon nanotubes with diameters ranging from 15 to 25 nm and varying from 2 to 5 μm in diameter were synthesized. The resulting carbon nanotubes were reinforced in commercially available CdO at 0.1, 0.2 and 1% to produce composite samples called H groups. The carbon nanotubes produced by the sol-gel method were reinforced with 0.1, 0.2 and 1% carbon nodules to produce composite samples called S groups.

SEM studies of the produced composites showed that the production of a homogeneous composite structure was difficult with the increase of the amount of carbon nanotubes. In samples containing 1% CNT, it was found that some regions contained carbon nanotubes in bulk without disintegration.

As a result of the electrical examinations of the produced composites depending on the temperature; it was found that the electrical conductivity increased with the carbon nanotube increase in both sample groups. In addition, it has been observed that the CdO-containing composites produced with Sol-Gel have higher electrical conductivities than the CdO-containing composites already provided.

As a result of optical examinations, the forbidden energy ranges of all samples have been determined. In the H group samples, the forbidden energy range of the pure CdO sample was found to be 1.75 eV and increased to the maximum level with 0.1% CNT content with the increase of KNT and then decreased with the increase of CNT. Composite containing 1% CNT was found to have a forbidden energy range of pure CdO. For the S group samples, the forbidden energy range of the pure CdO sample was found to be 1.88 eV and it was found that it increased to the maximum level with the content of 0.1% CNT with the increase of CNT and then decreased with the increase of CNT. Composite containing 1% CNT was found to have a forbidden energy range of pure CdO.

Consequently, it was determined that the composites using CdO produced by Sol-Gel showed better performance in terms of electrical and optical properties than the H group samples.

Acknowledgment

This study was presented at International Engineering Science and Education Conferences (2018).

5. References

- [1] Dong, Wenting; Zhu, Congshan. Optical properties of surface-modified CdO nanoparticles, *Optical Materials*, 22, (2003), 3, pp. 227-233.
- [2] LI, Feng; ZHANG, Changwen; ZHAO, Mingwen. Magnetic and optical properties of Cu-doped ZnO nanosheet: First-principles calculations. *Physica E: Low-dimensional Systems and Nanostructures*, (2013), 53, pp. 101-105.
- [3] GULINO, Antonino; COMPAGNINI, Giuseppe; SCALISI, Alessandro A. Large third-order nonlinear optical properties of cadmium oxide thin films, *Chemistry of materials*, 15, (2003), 17, pp. 3332-3336.
- [4] Farmanzadeh, D., Valipour, A., Adsorption of benzene and toluene molecules on surface of pure and doped cadmium oxide nanosheets: A computational investigation, *Applied Surface Science*, 450, (2018), pp. 509-515.

- [5] Nawar A. M., Aal N. A., Said N., El-Tantawy, F., & Yakuphanoglu F., Improving the optical and electrical properties of Zinc Oxide thin film by Cupric Oxide dopant, *IOSR J. Appl. Phys*, 6, (2014), 4, 17-22.
- [6] Azizar M., M.K.R. Rahman Khan, Effect of Annealing Temperature on Structural, Electrical and Optical Properties of Spray Pyrolytic Nanocrystalline CdO Thin Films, *Mater. Sci. Semicond. Process*, 24, (2014), pp. 26–33.
- [7] Yakuphanoglu F., Synthesis and Electro-Optic Properties of Nanosized-Boron Doped Cadmium Oxide Thin Films for Solar Cell Applications, *Sol. Energy*, 85, (2011), pp. 2704–2709.
- [8] Balmuri, S. R., Selvaraj, U., Kumar, V. V., Anthony, S. P., Tsatsakis, A. M., Golokhvast, K. S., & Raman, T., Effect of Surfactant in Mitigating Cadmium Oxide Nanoparticle Toxicity: Implications for Mitigating Cadmium Toxicity In Environment, *Environmental research*, 152, (2017), pp. 141-149.
- [9] Zheng, B.J., Lian, J.S., Zhao, L., Jiang, Q., Optical and Electrical Properties of In- Doped CdO Thin Films Fabricated by Pulse Laser Deposition, *Applied Surface Science*, 256, (2010), 9, pp. 2910–2914.
- [10] Coutts, T.J., Young, D.L., Li, X., Mulligan, W.P., Wu, X., Vac, J., 2000. “Search for Improved Transparent Conducting Oxides: A fundamental investigation of CdO, Cd₂SnO₄, and Zn₂SnO₄, *Journal of Vacuum Science & Technology A: Vacuum, Surfaces, and Films*, 18, (2000), 6, pp. 2646-2660.
- [11] Metz A.W., Ireland J.R., Zheng J.G., Lobo R.P., Yang Y., Ni J., Stern C.L., Dravid V.P., Bontemps N., Kannewurf C.R., Poepelmeier K.R., Marks T.J., Transparent conducting oxides: texture and microstructure effects on charge carrier mobility in MOCVD-derived CdO thin films grown with a thermally stable, low-melting precursor, *Journal of the American Chemical Society*, 126, (2004), 27, pp. 8477-8492.
- [12] Kumaravel, R., et al., Electrical, optical and structural properties of aluminum doped cadmium oxide thin films prepared by spray pyrolysis technique, *Materials Chemistry and Physics*, 122, (2010), 2-3, pp. 444-448.
- [13] Bhosale, C.H., Kambale, A.V., Kokate, A.V., Rajpure, K.Y., Structural, optical and electrical properties of chemically sprayed CdO thin films, *Materials Science and Engineering B*, 122, (2005), pp. 67–71.
- [14] Uplane, M. D., et al., Stability and electronic properties of Zn_xCd_{1-x}O alloys, *Mater. Chem. Phys*, 1, (1999), pp. 8630.
- [15] Peter, L.M., The photoelectrochemical properties of anodic Bi₂S₃ films, *Journal of Electroanalytical Chemistry and Interfacial Electrochemistry*, 98, (1979), 1, pp. 49-58.
- [16] Yufanyi, Divine Mbom, et al., CdO nanoparticles by thermal decomposition of a cadmium-hexamethylenetetramine complex, *Journal of Materials Science Research*, 3, (2014), 3, pp. 1.
- [17] Ye, M., Zhong, H., Zheng, W., Li, R., & Li, Y., Ultralong cadmium hydroxide nanowires: synthesis, characterization, and transformation into CdO nanostrands, *Langmuir*, 23, (2007), 17, pp. 9064-9068.

- [18] Zhang, J., Wang, Y., Lin, Z., Huang, F., Formation and Self-Assembly of Cadmium Hydroxide Nanoplates in Molten Composite-Hydroxide Solution, *Crystal Growth & Design*, 10, (2010), 10, pp. 4285-4291.
- [19] Prakash, T., Arunkumar, T., Sathiyasa Raj, D., Jayaprakash, R., Surfactant-aided Variation in CdO Nanocomposites Morphology, *Physics Procedia*, 49, (2013), pp. 36-43.
- [20] Ghoshal, T., Biswas, S., Nambissan, P. M. G., Majumdar, G., De, S. K., Cadmium Oxide Octahedrons and Nanowires on the Micro-Octahedrons: A Simple Solvothermal Synthesis, *Crystal Growth & Design*, 9, (2009), 3, pp. 1287-1292.
- [21] Tadjarodi, A., Imani, M., A novel nanostructure of cadmium oxide synthesized by mechanochemical method, *Materials Research Bulletin*, 46, (2011), 11, pp. 1949-1954.
- [22] Tadjarodi, A., Imani, M., Synthesis and characterization of CdO nanocrystalline structure by mechanochemical method, *Materials Letters*, 65, (2011), 6, pp. 1025-1027.
- [23] Shi, W., Wang, C., Wang, H., Zhang, H., Hexagonal Nanodisks of Cadmium Hydroxide and Oxide with Nanoporous Structure, *Crystal Growth & Design*, 6, (2006), 4, pp. 915-918.
- [24] Andeani, J. K., Mohsenzadeh, S., Phytosynthesis of Cadmium Oxide Nanoparticles from *Achillea wilhelmsii* Flowers, *Journal of Chemistry*, 2013, (2012), pp. 1-4.
- [25] Ramazani, M., Morsali, A., Sonochemical syntheses of a new nano-plate cadmium (II) coordination polymer as a precursor for the synthesis of cadmium (II) oxide nanoparticles, *Ultrasonics Sonochemistry*, 18, (2011), 5, pp. 1160-1164
- [26] Aydın, C., El-Nasser, H. M., Yakuphanoglu, F., Yahia, I. S., & Aksoy, M., Nanopowder synthesis of aluminum doped cadmium oxide via sol-gel calcination processing, *Journal of Alloys and Compounds*, 509, (2011), 3, pp. 854-858.
- [27] Duclaux, L., Review of the doping of carbon nanotubes (multiwalled and single-walled), *Carbon*, 40, (2002), 10, pp. 1751-1764.
- [28] Kumar, S. S., Vairam, S., Neelakandeswari, N., & Aruna, S., Effect of metal oxide charge transfer layers on the photovoltaic performance of carbon nanotube heterojunction solar cells, *Materials Letters*, 220, (2018), pp. 249-252.
- [29] S.P. Yakala, S.S. Yawale, G.T. Lamdhade, Tin oxide and zinc oxide based doped humidity sensors, *Sensors and Actuators A: Physical*, 135, (2007), pp. 388-393.
- [30] Ates, T.; Tatar, C., Yakuphanoglu, F., Preparation of semiconductor ZnO powders by sol-gel method: Humidity sensors, *Sensors and Actuators A: Physical*, 190, (2013), pp. 153-160.
- [31] S.P. Yawale, S.S. Yawale, G.T. Lamdhade, Tin oxide and zinc oxide based doped humidity sensors, *Sensors and Actuators A: Physical*, 135, (2007), pp. 388-393.

COMPARISON OF THE PRINTING AREAS FOR COMMONLY USED FONT TYPES: EXAMPLE OF GREEN INFORMATION

*Emrah AYDEMİR**

Some of the fonts used in the computer systems are designed to facilitate readability on the computer screen while others are designed to use both readability and print space economically. However, computer users do not have any idea which of the most commonly used fonts are more economical. In the present study, the printing area of the 10 commonly used fonts were examined with image processing methods and compared among each other. It is seen that the font which uses the least print area among Century Schoolbook, Courier New, Georgia, Times New Roman, Arial, Comic Sans MS, Tahoma, Verdana, Cambria, Calibri fonts is Courier New whereas the type that uses the least print area is Times New Roman. It was found that Comic Sans MS and Verdana used almost twice as much printing area as the font Courier New font. With this study, it is thought that computer users will be more careful and more conscious about the font they use for printing.

Key words: *Font Types, Printing Area, Image Processing, Green IT*

1. Introduction


As a result of various social, economic and environmental factors, it can be said that less paper is used recently. Specifically, users prefer e-mail, projector, document scanning, double-sided printing, single-spaced text, recycled paper, printing multiple pages per page, smaller font size, margin reduction, toner / ink saving mode, colorless and paper-free printing solutions [1]. Users and companies may also seek for such simple solutions that don't require investment.

Font designers put great efforts to choose features such as the type and size of the font to make the reader's reading experience more enjoyable and more comfortable. The typography of the text undoubtedly influences the reader's reading and comprehension performance [2, 3]. In addition, the font type and font size are also effective on reading and comprehension [4, 5]. Indirectly, text type can be said to affect the printing area used while **printing on type paper**. Türk Telekom has developed a font type with 25% less ink / toner for its use [6]. In this study, the widely used font types were compared regarding the use of the print area. Thus, it is aimed to increase both individual and institutional awareness about green IT.

2. Green Information Technologies

Reducing the use of environmentally harmful materials and chemicals in information and communication technology products or the use of recyclable products can be considered as green information. Technologies aiming to minimize the environmental impact of design, production and use of tools such as computers, monitors, printers, network and communication systems known as green IT [7]. In green IT, respect for nature and the efficient use of products are essential [8]. It also contributes to environmental

¹ Department of Computer Engineering, Kırşehir Ahi Evran University, Kırşehir, TURKEY, (emrah.aydemir@ahievran.edu.tr)

 <https://orcid.org/0000-0002-8380-7891>

sustainability through equipment that uses energy more effectively. Energy efficiency is provided not only by hardware but also by green software [9]. Especially virtualization technology is one of the best examples of this condition [10]. However, the awareness of individuals and institutions about green IT is very low [11]. The UK is the first country to focus on green IT strategies and policies [12]. The ultimate aim of green computing is to reduce operational costs and increase the efficiency of the IT infrastructure [13]. Individual and corporate users of information technologies can choose and apply the solution they want to use to reduce costs.

3. Commonly Used Font Types

Effective reading, fast reading, charm and general preference font types were examined and eight fonts were found to be widely used [14]. Hashim and Majid [15] used these fonts and the Calibri font in the readability of web texts. However, it has been concluded that fonts do not have an effect on web readability. These fonts are listed below.

1. Comic Sans MS
2. Verdana
3. Tahoma
4. Arial
5. Georgia
6. Century Schoolbook
7. Times New Roman
8. Courier New
9. Calibri

Times New Roman font type is designed for both legible and print economy. The Georgia font type is similar to the Times New Roman font type, but is particularly legible on the computer screen. The Century Schoolbook font type is also designed to be more legible, especially in books, and is widely used in school books [14].

Thesis manuscripts of the Institute of Science and Technology belonging to 208 state and private universities in Turkey examined the font types given in Table 1 below. Some universities have allowed their students to use more than one font. Some of the universities have been excluded from the evaluation due to their being a vocational school, not being an institute of science or lack of a thesis guide, resulting in 68 universities in total.

Table 1. Font Type and Number of Universities Using

| Font Type | Number of Universities | Rate (%) |
|--|------------------------|----------|
| Arial | 22 | 9,13 |
| Bitstream-Charter | 1 | 0,41 |
| Calibri | 9 | 3,73 |
| Cambria | 4 | 1,66 |
| Helvetica | 1 | 0,41 |
| Tahoma | 2 | 0,83 |
| Times New Roman | 132 | 54,77 |
| Verdana | 2 | 0,83 |
| There is no Institue or thesis writing guide | 68 | 28,22 |
| Grand Total | 241 | 100 |

The majority of the universities (54.77%) prefer the Times New Roman font type. Then Arial font type was preferred with 9.13%. Other font types are used in very few universities. With Helvetica, the Bitstream-

Charter font type is used only at a university. These font types are not installed in the Windows 10 version and in Microsoft Office 2016 by default. Therefore, these font types were excluded from the study. Cambria was added to nine font types and 10 font types were examined.

The 10 font types specified here are printed on 12-point A4 paper. Figure 1 below shows the 400% zoom of the "S" character. Only solid black is used, and each character is under the corresponding font. Figure 1 shows that some font types are thicker and more dominant when carefully examined. However, in some font types, thinner and lesser points are used. Such properties are effective in the use of the print area. Montrucchio and Ferrero [16] also found that in order to reduce the use of toner in these studies, these characters were able to place white spots in dense places and save about 40% of toner. Similar results were observed in different studies [17, 18]. Another method of saving toner is to illuminate some areas of characters in print. For example, only the color values of the internal pixels are exposed from the pixel groups of the same color. Thus, outlines are unaffected [19]. It is another method to make the inner and edge pixels independent [20] or to just open some parts of the image [21].

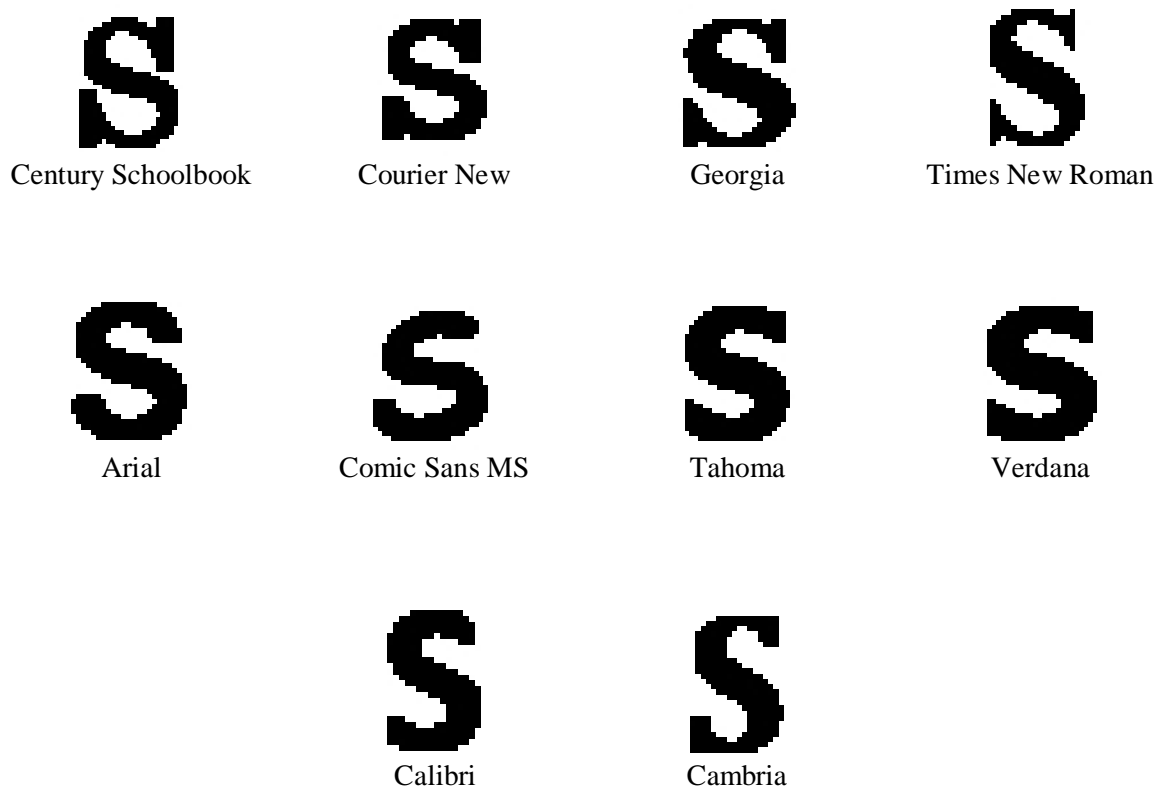


Figure 1. A Letter of Commonly Used Font Types (400% Zoomed)

4. Method

Font type and font size are important for less ink / toner consumption [22]. For this reason, with 10 commonly used font types in the study, 10 verses of the National Anthem were written in Word file to fit on one page. Then the output from this word file is saved as an image file with jpg extension. With the help of C # programming language, image files with jpg extension have been converted to Bitmap file type. Thus, red, green and blue values of each pixel will be accessible. These values consist of values between 0-255. The pixels of the image files created here are either full black or full white. By counting the black pixels and white pixels, the necessary analyzes were made and the ratio of the blacks was extracted. Thus, the use of printing area has been determined. Pixel numbers are calculated by the following equations.

$$T_s = \sum_{i=0}^y \sum_{j=0}^d s \quad (1)$$

T_s = Total black pixel count

y = Total number of horizontal pixels in paper

g = Total number of vertical pixels in paper

s = Black pixel

$$T_b = \sum_{i=0}^y \sum_{j=0}^d b \quad (2)$$

T_b = Total white pixel count

b = White pixel

$$T_p = T_s + T_b \quad (3)$$

T_p = Total pixel count

The number of white pixels is calculated by counting the white pixels by scanning all pixels horizontally and vertically. The number of black pixels is calculated similarly and the sum of the two gives the total number of pixels. As a result of the ratio of these values with the following equation 4, the printing area utilization ratio is calculated.

$$\varphi = \frac{T_s}{T_s + T_b} \quad (4)$$

φ = Black pixel ratio

5. Results

The calculated number of black pixels and white pixel numbers for each font is given in Table 2 below. In this case, the font with the least use of the print area was Courier New with 3.55%. The Times New Roman font is 4.94% followed by the least printable area.

Table 2. Print Area Usage Ratios of Font Types

| Font Types | Total white pixel count | Total black pixel count | Total | Black Ratio (%) |
|--------------------|-------------------------|-------------------------|---------|-----------------|
| Comic Sans MS | 3619078 | 249628 | 3868706 | 6,452493 |
| Verdana | 3619623 | 249083 | 3868706 | 6,438406 |
| Tahoma | 3622015 | 246691 | 3868706 | 6,376577 |
| Arial | 3633961 | 234745 | 3868706 | 6,067791 |
| Georgia | 3644581 | 224125 | 3868706 | 5,793281 |
| Cambria | 3668706 | 200000 | 3868706 | 5,169687 |
| Century Schoolbook | 3672691 | 196015 | 3868706 | 5,066681 |
| Times New Roman | 3679757 | 188949 | 3868706 | 4,884036 |
| Calibri | 3684153 | 184553 | 3868706 | 4,770406 |
| Courier New | 3731099 | 137607 | 3868706 | 3,556926 |

Comic Sans MS and Verdana font types have been found to have the most printing area fonts. It would be correct to say that these fonts use approximately twice as much printing space as the Courier New font type. There is a 0.1% difference between Times New Roman and Calibri font type.

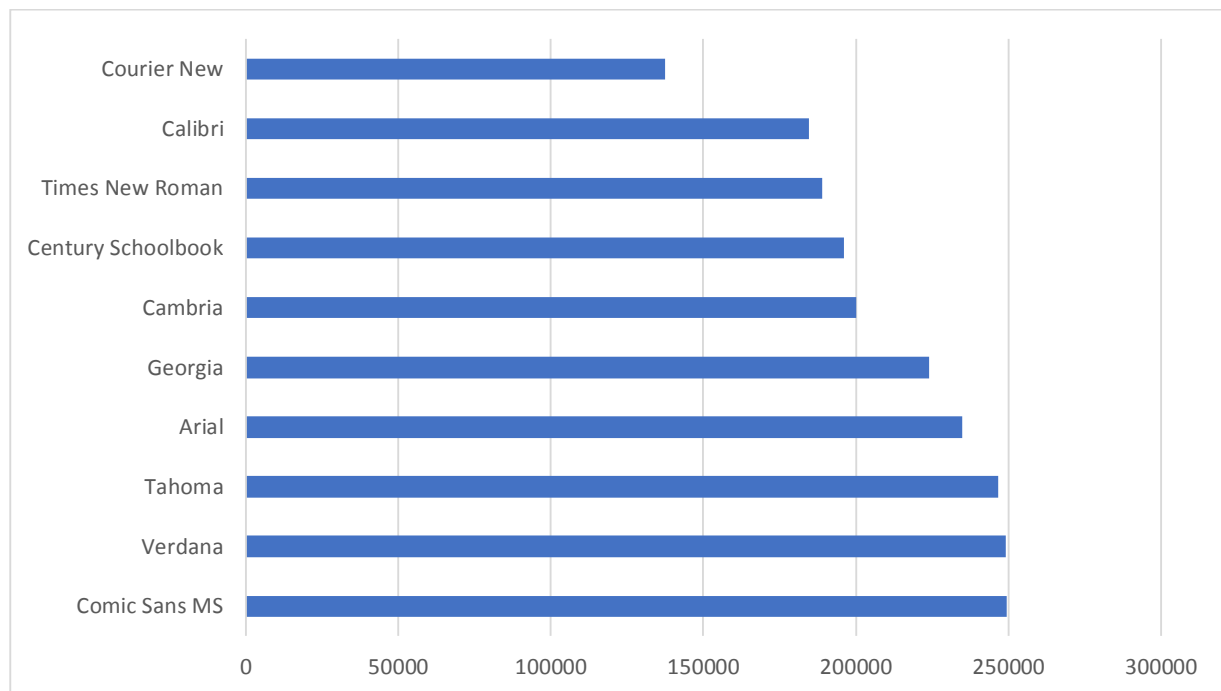


Figure 2. Black Pixel Numbers by Font Types

Black pixel numbers according to font types are shown in Figure 2 and there is very little difference between Comic Sans MS, Verdana and Tahoma but this difference is very high for Times New Roman and Courier New.

6. Discussion and Conclusion

Due to the fact that computers are indispensable devices of today, much of the information is obtained through these tools. In some cases, the information must be transferred from the computer to the paper. Even though this situation is reduced by different solutions, some users think that paper transfer is still necessary [23]. In this study, it was investigated which common fonts would be appropriate to use less toner or ink in case of paper printing. It has been seen that the Courier New font uses the most printing area of the 10 commonly used fonts. It would not be correct to say that reading from the computer screen is more disadvantaged than reading paper [24]. Therefore, of course, not printing is the right solution. However, selecting the font types that use less toner / ink when printing is required will be the most suitable option for greener printing. Milošević et al. [25] also produced similar results. The font generated by the font called eco-font was found to use 39% less ink than other fonts. It was seen that these two different fonts could be parsed by the users but not the problem. The Regulation on the Procedures and Principles to be Applied in the Official Correspondences [26] covering all public institutions and organizations states that the electronic documents will use Times New Roman or Arial as the font. However, the Times New Roman font uses approximately 10% less print space than the Arial font. This means that 10% toner savings will be achieved if the Times New Roman font type is selected and applied in all public institutions. It is good to see that the Times New Roman font type is mostly used in the thesis writing guidelines of the Institute of Science. Considering this situation, other

institutions and organizations will undoubtedly have many different benefits. Some of these are less damage to nature, less paper consumption, less toner consumption, less electricity. Particularly while efforts are being made for a sustainable ecosystem [29] on the one hand, ignoring such issues will be in contradiction in itself. Unhelkar [27] also refers to a number of users to reduce the environmental impact of information technologies in their daily life, such as turning off the monitor, minimizing printing operations or using recycled paper. It would be right to say that there is almost no difference between Times New Roman and Calibri. This difference can be ignored and the two font types can be considered equal in terms of the print area. Furthermore, in future studies, both fonts that use less print space and methods that can hide data in various ways can be used [28].

7. References

- [1]. Werner, K., Rothenberg, S., & Miller, J. (2012). Drivers of greener print choices: an exploratory study of print consumer environmentalism, *A Research Monograph of the Printing Industry Center at RIT*. <https://scholarworks.rit.edu/books/101>.
- [2]. Ralekar, C., Saha, P., Gandhi, T. K., & Chaudhury, S. (2018). Effect of Devanagari Font Type in Reading Comprehension: An Eye Tracking Study. *In International Conference on Intelligent Human Computer Interaction*. Springer, Cham, 136-147.
- [3]. Kumar, R., Malik, A., Singh, S., Kumar, B., & Chand, S. (2016, April). A space based reversible high capacity text steganography scheme using font type and style. *In 2016 International Conference on Computing, Communication and Automation (ICCCA)* (pp. 1090-1094). IEEE.
- [4]. Kim, H., & Park, S. H. (2012). What are Legible Korean Font Sizes within In-Vehicle Information Systems?. *Journal of the Ergonomics Society of Korea*, 31(2), 397-406.
- [5]. Kim, S., Lee, K. E., & Lee, H. W. (2013). The Effect of Hangul Font on Reading Speed in the Computer Environment. *Journal of the Ergonomics Society of Korea*, 32 (5), 449-457.
- [6]. Haberturk, (2019). *A first in the world from Türk Telekom*, Online Available: <https://www.haberturk.com>.
- [7]. Laudon, K. C., & Laudon, J. P. (2015). *Management information systems: Managing digital business*. Ankara, Turkey: Nobel Publisher.
- [8]. Damar, M., & Goksen, Y. (2018). User and Institution Oriented Energy Management System with Green IT Approach. *Dokuz Eylul University Faculty of Engineering Science and Engineering Journal*, 20 (58), 259-274.
- [9]. Kern, E., Dick, M., Johann, T., & Naumann, S. (2011). Green software and green it: An end users perspective. *In Information Technologies in Environmental Engineering* (pp. 199-211). Springer, Berlin, Heidelberg.
- [10]. Cetin, H. and Akgun, A. (2015). A Comparison of Virtualized and Traditional Systems in the Context of Green Information Technologies. *Journal of Alanya Faculty of Business*, 7 (2), 131-142.
- [11]. Goksen, Y., Damar, M., and Dogan, O. (2016). Green Computing: A Case Study In A State Organization And Policy Recommendations. *Ege Academic Review*, 16 (4), 673-686.
- [12]. Chai-Arayalert, S., & Nakata, K. (2011, August). The evolution of green ICT practice: UK higher education institutions case study. *In Proceedings of the 2011 IEEE/ACM International Conference on Green Computing and Communications* (pp. 220-225). IEEE Computer Society.
- [13]. Agrawal, N., & Agarwal, K. N. (2012). Current trends in green ict. *JoAAG*, 7(1), 71-85.
- [14]. Bernard, M., Lida, B., Riley, S., Hackler, T. and Janzen, K. (2002). A comparison of popular online fonts: Which size and type is best. *Usability news*, 4 (1).
- [15]. Hashim, A. A., & Majid, M. A. (2015). Effects of video display terminal resolutions to the legibility of text on a web page. *International Journal of Software Engineering and Computer Systems*, 1(1), 131-157.
- [16]. Montrucchio, B., & Ferrero, R. (2016). Toner savings based on quasi-random sequences and

- a perceptual study for green printing. *IEEE Transactions on Image Processing*, 25(6), 2635-2646.
- [17]. Shu, J. (1995). Error diffusion with ink reduction for high quality and high resolution ink jet printing. *In Proceedings. IEEE International Conference on Image Processing*, 3(1), 121–124.
- [18]. Guo, J. M. (2006). A complete printer model in error-diffused halftone images. *In Proceedings. IEEE International Conference Image Process*, 1529–1532.
- [19]. Davidson, M. L., & Hawkins, B. C. (2001). *U.S. Patent No. 6,266,153*. Washington, DC: U.S. Patent and Trademark Office.
- [20]. Rombola, G., & Foster, T. J. (2009). *U.S. Patent No. 7,602,510*. Washington, DC: U.S. Patent and Trademark Office.
- [21]. Ray, E. T. (2013). *U.S. Patent No. 8,467,105*. Washington, DC: U.S. Patent and Trademark Office.
- [22]. Možina, K., Medved, T., Rat, B., & Bračko, S. (2010). Influence of light on typographic and colorimetric properties of ink jet prints. *Journal of Imaging Science and Technology*, 54(6), 60403-1-60403-8.
- [23]. Josephson, S. (2008). Keeping your readers' eyes on the screen: an eye-tracking study comparing sans serif and serif typefaces. *Visual communication quarterly*, 15(1-2), 67-79.
- [24]. Duran, E., & Alevli, O. (2014). The effect of reading on screen on comprehension of 8th grade students. *Literacy Education Research*, 2 (1), 1-11.
- [25]. Milošević, R., Nedeljković, U., Banjanin, B., Novaković, D., & Kašiković, N. (2016). The analysis of ink jet printed eco-font efficiency. *Journal of Graphic Engineering and Design*, 7(1), 1-13.
- [26]. The Regulation on the Procedures and Principles to be Applied in the Official Correspondences, (2015). *T. C. Official Newspaper*, Number: 29255, 2 February 2015.
- [27]. Unhelkar, B. (2011). Green IT: The next five years. *IT Professional*, 13(2), 56-59.
- [28]. Tuncer, T., & Sönmez, Y. (2017). Block based data hiding method for images. *European Journal of Technique*, 7(2), 85-95.
- [29]. Mesbah, L. A. (2014). Ecosystem Services for a Sustainable Energy Policy in Bosnia and Herzegovina. *Balkan Journal of Electrical and Computer Engineering*, 2(3), 108-112.

A GEOLOGICAL AND PETROLOGICAL OVERVIEW OF THE HISTORY OF KIRA MOUNTAIN: AN APPROACH TO THE SIMILARITY AND DIFFERENCE OF KARACADAG


Süleyman POLAT^{1}, Hakan ÇOBAN², Şemsettin CARAN³*

The volcanism of Kira Mountain, at south of the Bitlis Zagros suture zone (BZK), was erupted from different joint systems by young extensional tectonic regime. The main geological and petrographic features of the Late Miocene Kira Mountain volcanics were investigated as well as the major oxide, trace element and rare earth element geochemical characteristics. The Kira Mountain volcanic products are classified as basanite, tephrite and trachy-basalt and show alkaline character above the alkaline-subalkaline separation line. Nonetheless, the peripherals associated with these volcanics starts with the Miocene aged Şelmo Formation. This formation is accompanied by Oligocene Germik Formation and Eocene Gercus Formations. The Karacadag volcanics are adjacent to the Lower, Middle and Late-Cambrian Sadan, Koruk and Sosink Formations, respectively, predominantly the Precambrian Derik Formation. In addition to these formations, Late Cretaceous Karababa and Karbogaz Formations, Late Cretaceous-Paleocene Germav Formation, Eocene Midyat Formation and Eocene Şelmo Formations are also contiguous. The phenocrysts of the Karacadag volcanics include olivine, clinopyroxene, plagioclase and opaque minerals. In the Kira Mountain volcanics, olivine, plagioclase and opaque minerals are accompanied by sanidine and pyroxene. As reported by the geochemical and petrographical studies, The Karacadag volcanics are mainly classified as basalt and trachy-basalt, tephrite, basanite and hawaiite. Moreover these lavas are mainly alkaline and present subalkaline transition. The Karacadag volcanics erupted in three different stages with different phases, and the Kira mountain volcanics were found to be identical with the Siverek stage.

Key words: Kira Mount, Batman, Karacadag, basalt

1. Introduction

After the closing of the Tethys Ocean in the Middle Miocene (approximately 11-12 Ma, [13, 14, 15]), the deformation and compression effect in Anatolia, which started with the Arabian plate dipping under the Eurasian plate, continues effectively today. As a result of this collision to the north of the Bitlis-Zagros suture zone (BZK), volcanic units such as Mount Ararat, Mount Nemrut, Mount

¹ Department of Geological Engineering, Batman University, Batman, Turkey, (suleyman.polat@batman.edu.tr)  <https://orcid.org/0000-0001-9726-3840>

² Department of Civil Engineering, Bitlis Eren University, Bitlis, Turkey, (hcoban@beu.edu.tr)  <https://orcid.org/0000-0002-9614-6818>

³ Department of Geology Engineering, Süleyman Demirel University, Isparta, Turkey, (semsettincaran@sdu.edu.tr)  <https://orcid.org/0000-0001-6889-6024>

Suphan and Mount Tendurek have developed within the Erzurum-Kars Plateau. In the south of BZK, the Late Miocene Kıra Mountain, which has a limited distribution compared to the Karacadag volcanics and approximately 75km to the east (Figure 1), has a long arc shape. Şelmo Formation (Miocene; conglomerate, sandstone, shale, siltstone, etc.), Germik Formation (Oligocene; shale, dolomite and gypsum) and Gercus Formations (Eocene; conglomerate, sandstone and claystone) were covered by the volcanics of the Kıra Mountain.

Another volcanic unit in the south of BZK is Karacadag, which has continued its activity in the Late Miocene-Holocene (approximately 11 Ma-0,01 Ma), the largest volcanic complex in Anatolia (Figure 2). The neighboring units and geological features of Karacadag begin with Derik Group formations from old to young. Derik Group formations are known as Telbesmi (Precambrian; andesitic intercalated sandstones), Sadan (Lower Cambrian; sandstone mainly with shale alternation), Koruk (Middle Cambrian; limestone, dolomite, dolomitic limestone) and Sosink (Middle- Late Cambrian; sandstone-weighted, occasionally marl and shale alternation) outcropping in different terrains throughout the region. These formations are accompanied by Karababa (Mardin group member, Late Cretaceous; limestone, dolomite, dolomitic limestone), Karbogaz (Adiyaman group member, Late Cretaceous; limestone, occasionally chert band limestone), Germav (Sırnak Group member, Late Cretaceous-Paleocene; marl, shale, sandstone intercalation), Hoya (Midyat Group member, Eocene; limestone and dolomite intercalations) and Şelmo (Silvan Group member, Miocene; milstone, shale, sandstone) formations [2, 5, 7, 8, 16, 17].

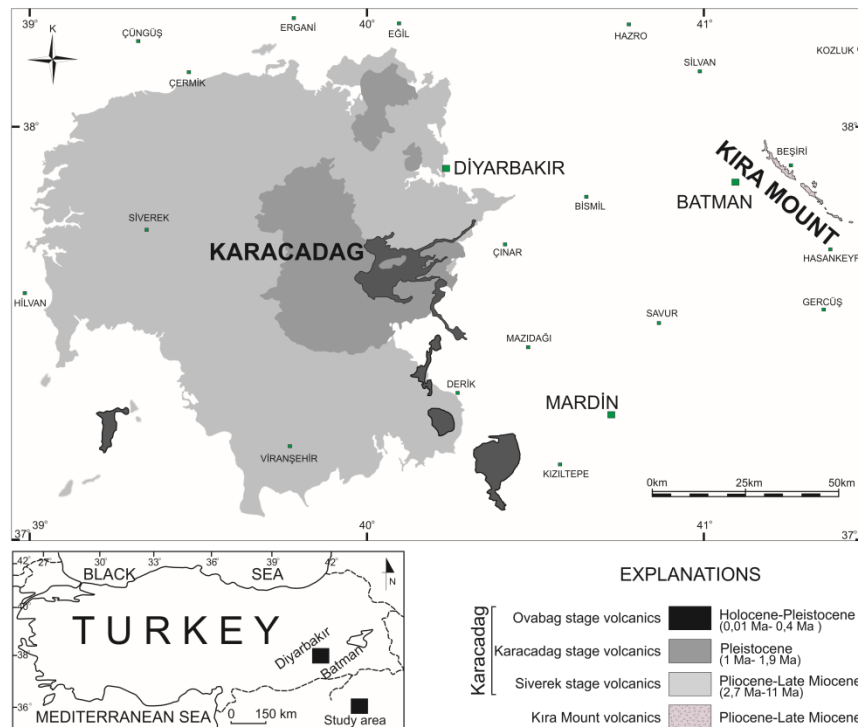


Figure 1 Mapping of Kıra Mount and Karacadag in Southeast Anatolia and the spread of two volcanism (The dispersion of Karacadag volcanism is modified from [12])

The Kıra Mountain lavas, which can be traced from Batman center, erupted Eocene aged limestones (Hoya formation), sedimentary rocks with Oligocene gypsum-shale-evaporites (Germik formation) and Miocene aged conglomerate-claystone-shales (Şelmo formation) along the stretching

cracks. In this study, it is aimed to present the geochemical and petrographical data of the Kira Mountain and the Karacadag volcanism. Additionally, the mantle resource areas are evaluated in the light of the available data.

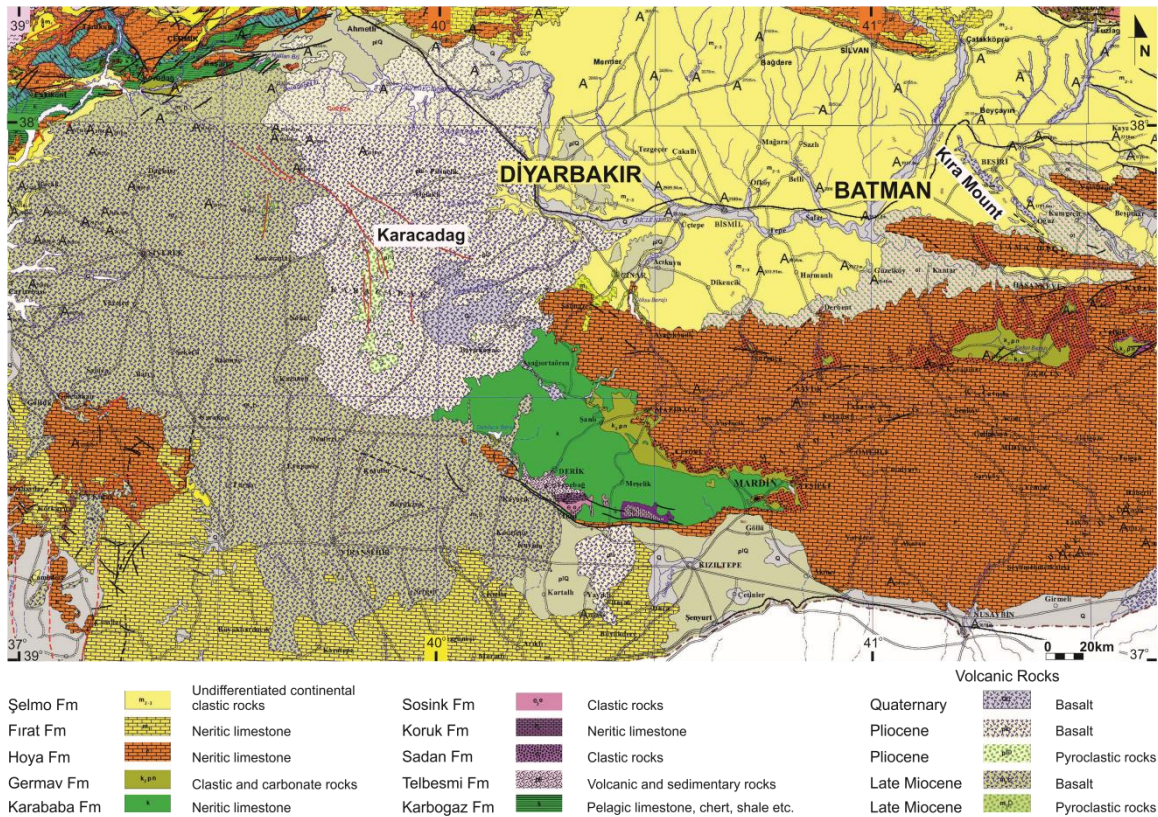


Figure 2. Geological map of the study area and its vicinity (the regional geology map is modified from [12])

2. Analytical techniques

In addition to the geological and topographical maps of the study area and its surroundings, more than 100 representative samples were collected by using satellite data. Thin sections were prepared in different university laboratories for petrographical studies from selected samples. Thin sections were examined by Leica DM750P brand under polarized microscope and detailed petrographic determinations were made especially mineralogical composition and textural features. For geochemical data, major oxides, trace elements and rare earth element analyzes were performed at the laboratories of ACME (Canada) and Istanbul Technical University. Each sample was weighed between 0.1g and 1g and subjected to a solution of HCF: HNO₃: HF (3:1:0.5) acid mixture at a temperature of 180 °C and a pressure of 20 bar at the Berghof brand microwave. Fully soluble analyte solutions were analyzed on a Perkin Elmer ELAN DRC-e brand ICP-MS, Perkin Elmer Analyst 700 AAS device. Multi-element ICP-MS calibration solutions at 10mg/L concentration were used as calibration solutions.

3.3. The geology of the investigated field

3.1. Kira mount volcanics

The volcanics which can be traced along the Beşiri (Batman) district and nearby villages have a plateau basalt character and layer thickness reaches 40m. Considering the land spread (about 23 km²),

there are no pyroclastic material exits. The color and textural characteristics of basaltic magma show occasional changes, and the presence of aggregates with gas porosity or column shape is noteworthy. Volcanites, where limited samples of basalt lava morphology are observed, can be distinguished from Karacadag volcanics in the field observations with abundant fractures and widespread discontinuities. In the scope of phenocrystalline, feldspar minerals (sanidine and plagioclase) are added to olivine, pyroxene and opaque minerals. Minerals are generally not euhedral, but they offer examples of alteration at different scales. Opaque minerals are commonly found in sections, while the feldspar bars in the matrix give typical basaltic texture samples (Figure 3).

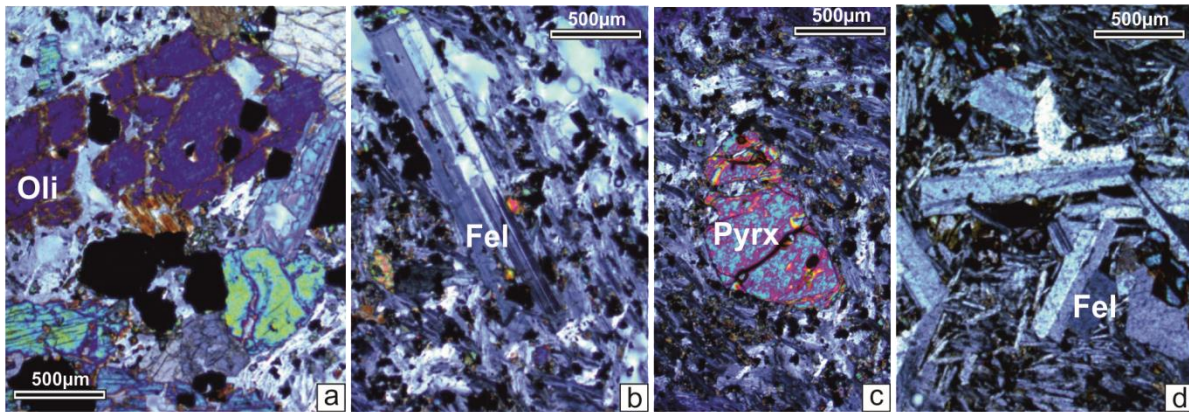


Figure 3. The Kırta Mount volcanics generally show basaltic texture as euhedral or subhedral phenocrysts. a) Sample 1.1; Hypidiomorphic macrocrystalline olivines, microcrystalline pyroxene and opaque mineral grains in hypocrystalline porphyritic texture b) Sample 4a.2; plagioclase laths with polysynthetic, lamellar twins with lots of opaque minerals c) Sample 4b.3; the coloured crystal is pyroxene and the rest of the field is occupied by plagioclase microlites, high relief small opaque minerals and small pyroxene remnants in hypocrystalline texture d) Sample E4b-7, showing porphyritic texture, euhedral feldspar phenocrysts are seen in dense groundmass with abundant plagioclase microlites. (Oli: olivine, Fel: feldspar, Pyrx: pyroxene and all samples given above are trachy-basalt)

3.2. Karacadag volcanics

Karacadag volcanism, which is located in a very wide geography (about 10 000 km²) covering different provinces of Mardin and Şanlıurfa, mainly in Diyarbakır, has been active in three main stages [3, 4]. The most widely distributed and relatively oldest Siverek stage (2.7 Ma-11 Ma/constitutes 80% of the volcanism) was the north-south direction from the south of Ergani to Viransehir. The Karacadag stage (1 Ma- 1,9 Ma/constitutes 15% of the volcanism) composes the main body of Karacadag and contains pyroclastic aggregates in some places. The youngest member, the Ovabag stage (0,01 Ma- 0,4 Ma/constitutes 5% of volcanism), has reached the SE directional surface, not in the form of a whole, but in several parts of the opening cracks. The phenocrysts of these volcanics include olivine, pyroxene (clinopyroxene), feldspar (plagioclase) and opaque minerals [10, 11, 12].

3.3. Geochemical properties

The major oxides, trace elements and REE of the Kırta Mountain volcanics and the Karacadag volcanic complex (Table 1 and Table 2) were evaluated in the TAS diagram proposed by Le Bas et al. (1986) [9]. (Data related to the Karacadag volcanites are described in [3, 10, 11, 12]). The main oxide changes reflect a characteristic of the sodic composition rich in TiO₂, which is commonly seen around the Mediterranean when both volcanic products are considered together. The samples belonging to Karacadag show a wide distribution up to basalt and trachy-andesite including trachy-basalt, tefrite,

phonotephrite, basanite, basaltic trachy-andesite, and alkaline character except for a few examples according to Irvine and Baragar 1971 [6] (Figure 4).

Table 1. Major oxide values of Kırta Mount volcanites and Karacadağ volcanic complex (%)

| | | SiO ₂ | Al ₂ O ₃ | Fe ₂ O ₃ | MgO | CaO | Na ₂ O | K ₂ O | TiO ₂ | P ₂ O ₅ | MnO | Cr ₂ O ₃ |
|----------------|-------|------------------|--------------------------------|--------------------------------|-------|-------|-------------------|------------------|------------------|-------------------------------|------|--------------------------------|
| Kırta Mount | (min) | 46,30 | 13,74 | 13,90 | 3,48 | 7,20 | 3,84 | 1,44 | 3,44 | 1,56 | 0,21 | 0,047 |
| | (mak) | 47,60 | 14,41 | 15,02 | 4,16 | 8,97 | 4,36 | 1,52 | 3,61 | 1,67 | 0,24 | 0,117 |
| Karacadağ | (min) | 43,27 | 11,35 | 6,82 | 4,40 | 4,57 | 2,31 | 0,43 | 1,18 | 0,02 | 0,12 | 0,00 |
| | (mak) | 61,50 | 18,17 | 15,83 | 11,36 | 13,17 | 5,42 | 3,25 | 4,76 | 1,28 | 0,26 | 0,07 |

Table 2. Trace elements and REE values of Kırta Mount volcanites and Karacadağ volcanic complex (ppm)

| | Rb | Sr | Ba | Sc | V | Cr | Co | Ni | Y | Zr | Nb | La | |
|----------------|-------|-------|-------|-------|-------|-------|-------|------|-------|-------|-------|------|-------|
| | (min) | 21,9 | 361,1 | 385 | 28 | 171 | 320 | 25,5 | <20 | 45,3 | 250,6 | 16,5 | 34,2 |
| | (max) | 29,3 | 498,8 | 544 | 29 | 189 | 800 | 34,8 | <20 | 51 | 268,8 | 18,2 | 36,9 |
| Kırta Mount | Ce | Pr | Nd | Sm | Eu | Gd | Tb | Dy | Ho | Er | Tm | Yb | |
| | (min) | 76,8 | 10,49 | 47,5 | 10,73 | 4,2 | 11,28 | 1,67 | 9,25 | 1,82 | 4,82 | 0,62 | 3,79 |
| | (max) | 82,6 | 11,27 | 51,1 | 11,62 | 4,49 | 12,13 | 1,85 | 10,73 | 1,97 | 5,27 | 0,68 | 4,44 |
| | Lu | Th | Pb | U | Hf | Ta | Ga | Cs | Cu | Zn | | | |
| (min) | 0,52 | 3,8 | NA | 0,6 | 5,2 | 1 | 19,5 | <0,1 | 25,99 | 167 | | | |
| (max) | 0,63 | 4,7 | NA | 1,7 | 6,1 | 1,4 | 22,1 | 1,1 | 48,53 | 203,1 | | | |
| Karacadağ | Rb | Sr | Ba | Sc | V | Cr | Co | Ni | Y | Zr | Nb | La | |
| | (min) | 3,30 | 412 | 147 | 18,0 | 142 | 60 | 26,0 | 57 | 18,8 | 112,0 | 14,1 | 9,83 |
| | (max) | 33,0 | 1160 | 543 | 25,00 | 263 | 460 | 67,0 | 300 | 30,80 | 897 | 90 | 82,90 |
| | Ce | Pr | Nd | Sm | Eu | Gd | Tb | Dy | Ho | Er | Tm | Yb | |
| | (min) | 22,80 | 2,82 | 12,10 | 3,31 | 1,31 | 3,74 | 0,58 | 3,21 | 0,59 | 1,66 | 0,22 | 1,29 |
| | (max) | 162 | 18,90 | 64,10 | 13,70 | 4,52 | 11,50 | 1,50 | 6,60 | 1,10 | 2,70 | 0,36 | 2,11 |
| | Lu | Th | Pb | U | Hf | Ta | Ga | Cs | Cu | Zn | | | |
| | (min) | 0,15 | 0,72 | 0,50 | 0,20 | 2,65 | 0,76 | 36,0 | 0,10 | 40 | 150 | | |
| | (max) | 0,27 | 6,80 | 6,00 | 2,20 | 11,10 | 7,10 | 20,1 | 0,80 | 100 | 260 | | |

Although it is noteworthy that the Kırta Mountain lavas are falling into the trachy-basalt, tephrite, phonotephrite, and basanite range, it is determined that they have an alkaline character such as Karacadağ products. In order to examine the main oxide data carefully, Kırta Mountain volcanics show lower values of SiO₂, Al₂O₃, MgO, CaO, Na₂O, K₂O and TiO₂ compared to Karacadağ products whereas Fe₂O₃ and MnO data are considered as equivalent on average. With respect to the P₂O₅ and Cr₂O₃ values, an enrichment is observed.

It is seen that the rising basalts, mostly Siverek stage volcanics and Karacadağ stage volcanites, predominantly alkaline character Karacadağ products imply the Nb/La (>1) and Nb/Yb ratios showing a scattered trend and the OIB type as the asthenospheric mantle. In contrast, the lower Nb/La (<1) and low Nb/Yb (<8) values of the Kırta Mountain volcanics indicate that the mantle source they derive is

interacting with each other on the basis of the mixed lithospheric-asthenosphere mantle, which is a strong evidence of the heterogeneity of the mantle source (Figure 5).

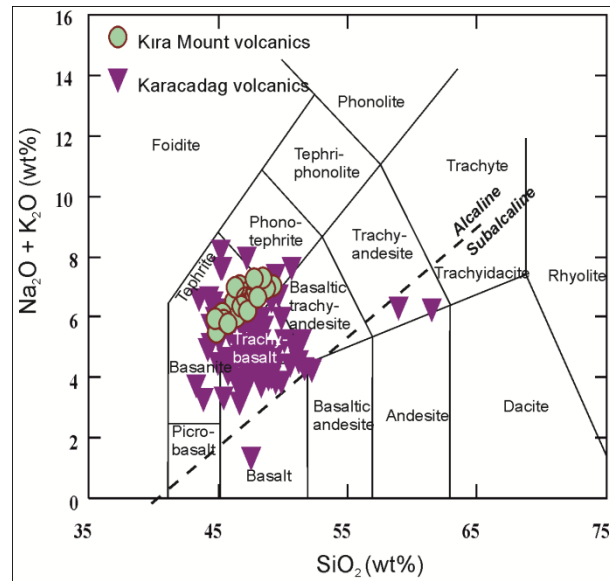


Figure 4. TAS diagram [9] and geochemical characteristics [6] of Kira Mount volcanics and Karacadag volcanics

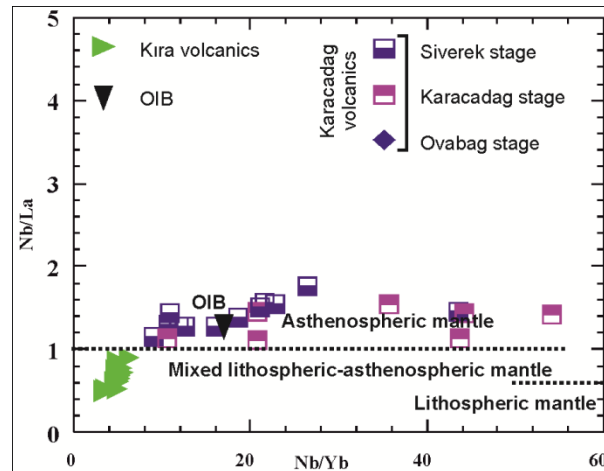


Figure 5. Nb/La-Ln/Yb diagram of Kira Mount volcanics and Karacadag volcanics [1]

4. Discussion

To take regionally, the collision of the Arabian and Anatolian plate, which controls the neotectonics Turkey is one of two main events and has played a decisive role in terms of the dynamics of this case. This movement formed an in-plate volcanism that started in Late Miocene and continued until Quaternary and thus formed Karacadag and Kira Mountain. Karacadag lava coming out of the opening cracks and reaching the surface in the direction of NW-SE is in line with the Kira Mountain lava. The Karacadag products also show formations in the N-S direction. While the Kira Mountain volcanites are classified as tephrite, phono-tephrite, trachy-basalt and basanite, the Karacadag magma also offers a wide distribution extending from basalt to trachy-andesite. Karacadag products are similar

to OIB and are predominantly of asthenospheric mantle origin. In contrast, the magma forming the Kırta Mountain marks a mixed lithospheric-asthenospheric mantle composition.

5. Conclusion

On the basis of the stratigraphic location of the region for many years, the Kırta Mountain volcanics have been evaluated as Pliocene and some have been accepted as Quaternary in literature studies. Nonetheless, in the light of the current geological data, with the effect of the stress regime developed due to neotectonic deformation in the region, mantle uplift was realized and basaltic products were exposed in plateau basalt form spreading in Diyarbakır and Batman regions. Although the Kırta Mountain lavas exhibit similar mineral paragenesis, they can be distinguished from the Karacadağ Volcanites by their abundant fractures and widespread discontinuities in the field surveys as well as by their distinctive color distribution in different shades. Considering the unique contribution of analysis data, it is quite clear that the Late Miocene aged Kırta Mountain volcanites were found in the Karacadağ volcanites which correspond to Siverek stage periodically, exhibit different geochemical characteristics and derived from different types of magma.

References

- [1] Abdel-Rahman, A.M., Mesozoic Volcanism in the Middle East: Geochemical, Isotopic and Petrogenic Evolution of Extension Related Alkali Basalts from Central Lebanon. *Geological Magazine* 139/6 (2002), pp. 621–640
- [2] Canpolat, E., Geomorphology of Karacadağ (Diyarbakır) Volcano, Master Thesis, Istanbul University Institute of Social Sciences Department of Geography, Istanbul, Turkey, 2005
- [3] Ekici, T., Macpherson, C. G., Oflu, N., Polybaric Melting of a Single Mantle Source During the Neogene Siverek Phase of the Karacadağ Volcanic Complex, SE Turkey, *Lithos* (2012), 146-147, pp. 152-163
- [4] Ekici, T., Macpherson, C. G., Oflu, N., Fontignie, D., Foreland Magmatism During the Arabia-Eurasia Collision: Pliocene-Quaternary Activity of the Karacadağ Volcanic Complex, SW Turkey, *Journal of Petrology Volume 55* (2012)., Number 9, pp. 1753-1777
- [5] Ercan, T., Şaroğlu, F., Turhan, N., Matsuda, J. I., U, T., Fujitani, T., v.d., Geology and Petrology of Karacadağ Volcanites. *Bulletin of the Geological Society of Turkey*, S 6 (1991), pp. 118-133
- [6] Irvine, T. N., Baragar, W. R. A., A Guide to the Chemical Classification of the Common Volcanic Rocks. *Canadian Journal of Earth Sciences* 8 (1971), pp. 523-548
- [7] Kalkan, Ö., Petrogenesis of the Basalts of Kırta Mount (Batman), Master Thesis, Batman University Graduate School of Natural and Applied Sciences, Batman. Turkey, 2014
- [8] Kavak, O., *Diyarbakır ve Çevresinde Yer Alan Karacadağ Volkaniti'nin Genel Özellikleri. (General properties of Karacadağ Volcanite in Diyarbakir and its Surroundings), Karacadağ and the Book of Environment*, Uzman Printing, Page 361-372, Diyarbakır, Turkey, 2013
- [9] Le Bas, M.J., Le Maitre, R.W., Streckeisen, A., Zanettin, B., A Chemical Classification of Volcanic Rocks Based on the Total Alkali-Silica Diagram. *Journal of Petrology* 27 (1986), pp. 745–750

- [10] Lustrino, M., Keskin, M., Mattioli, M., Lebedev, V. A., Chugaev, A., Sharkov, E., Kavak, O., Early Activity of the Largest Cenozoic Shield Volcano in the Circum-Mediterranean Area: Mt. Karacadag, SE Turkey. *European Journal of Mineralogy* 22 (2010), pp. 343-362
- [11] Lustrino, M., Keskin, M., Mattioli, M., Kavak, O., Heterogeneous Mantle Sources Feeding the Volcanic Activity of Mt. Karacadag (SE Turkey), *Journal of Asian Earth Sciences* 46 (2012), pp. 120–139
- [12] MTA, 2002. 1/500 000 Scale Geological Map of Turkey, Diyarbakır, Ankara
- [13] Şengör, A. M. C. and Yılmaz, Y. Tethyan evolution of Turkey: A Plate Tectonic Approach. *Tectonophysics*, 75 (1981), pp. 181–241.
- [14] Okay, A. I., Şengör, A. M. C. and Görür, N. 1994. Kinematic History of the Opening of the Black Sea and its Effects on Surrounding Regions. *Geology*, 22 (1994), pp. 267–270.
- [15] Okay, A.I., 2008; Geology of Turkey: A synopsis. *Anschnitt, Zeitschrift für Kunst und Kultur im Bergbau, Beiheft* 21, 19-42. Veröffentlichungen aus dem Deutschen Bergbau-Museum Bochum, Nr. 157.
- [16] Yeşilova, Ç., Helvacı, C., Stratigraphy and Sedimentology of the North of Batman-Siirt, *Bulletin of TPDJ*, Volume 23 (2012), Issue 2, pp. 7-49
- [17] Yeşilova, G. P., Helvacı, C., Diagenesis and Paleogeographic Development of Oligocene Evaporites (Kurtalan, SW Siirt) in Germik Formation, *Hacettepe University Earth Sciences Application and Research Center Bulletin*, 34/1 (2013), pp. 1-22

ASSESSMENT OF ENERGY PERFORMANCE BASED ON ENERGY AUDIT OF A HOTEL USING EXERGY APPROACH


Mehmet Emin Ugur OZ^{1}, M. Ziya SOGUT²*


This study presents an analytic assessment method of energy consumption processes that was developed to apply to the energy management systems of hotels. This method has based directly on an exergetic approach and examined energy and environmental performances using energy and exergy analysis with the pre-energy audit. The energy efficiency performance of the hotel was considered for uninsulated (Case I) and insulated (Case II) conditions. The results of the analysis show that energy consumption losses are related to not only the structural features of the buildings but also the operational management of the hotels. Also, the specific energy consumption of Case II is 43,08% higher than the Case I. Exergetic efficiency for insulated and uninsulated conditions were found as 27.31% and 16.26%, respectively. At the end of the study, some recommendations on effective energy management and the applications of a hotel were revealed.

Key words: Hotels, Energy Management, Energy Audit, Energy Analysis, Exergy Analysis.

1. Introduction

Increases in the energy consumption based on fossil energy resources, which is the primary reason for the environmental impact, has been motivated all sectors for investigation energy-efficient applications. According to researches of the European Union (EU), the building sector has approximately 40% of the total energy consumption and 36% of the CO₂ emissions. Hotels, which are known as having high energy consumption and large complex buildings among the commercial buildings, have 6% roundly of the total energy consumption of the building sector. Hotels, as commercial enterprises, directly depends on tourism mobility and the capacity of the sector, which served 980 million people in 2011, is expected to will increase to 55% in 2020 to serve more than 1.5 billion people [1]. A study about 610 hotels across Europe with including 40 hotels in Ankara Turkey, revealed that the amount of energy used by most hotels is between 200-400 kWh/m².yr. This important potential for consumption, which is dependent on the occupancy rates of hotels, has contributed significantly to the emission production [2]. Therefore, the determination of energy efficiency and savings potential is the critical point for reducing energy waste and CO₂ emissions. In the literature, many studies related energy efficiency and savings based on the building sector like commercial, high-volume buildings and hotels have found [3,4]. Energy analysis considering hotels is defined as a

¹ M.Emin Ugur OZ Vocational Schools of Tech. Sci., Energy Depart., Uludag Univ., Bursa, Turkey (meuguroz@uludag.edu.tr)  <https://orcid.org/0000-0002-2306-6008>

² M.Ziya Sogut, Maritime Faculty, Piri Reis University, Tuzla/Istanbul, Turkey, (mzsogut@gmail.com)  <https://orcid.org/0000-0002-2306-6008>

quantitative expression of consumption and expresses only potential use of existing energy. In this type of analysis, defining and evaluating of the system according to losses are not possible. To define irreversibility potential and energy losses of hotels are explained by exergy analyses directly. Exergy analysis in hotels is a tool to determine the real potential of energy losses and carbon footprint. [5]. Energy and exergy analyses of hotels have become prominent regarding energy management, energy costs and sustainable environments in buildings. However, few studies in the literature have focused on hotels within the scope of exergetic analyses. Gonçalves studied new energy and exergy indicators, which are suggested for legislation, regarding building energy performance in a 4-star hotel in Coimbra, Portugal [5]. Xydis et al. analyzed the energy and exergy efficiencies of four hotels in different regions of Greece using data acquired from 2001-2002 [6]. Kilkis stated that efficiency and environmental compliance could ensure lower costs for a sustainable exergy-efficient building. This situation was explained by the dynamic and controlled balance between radiant changes and convective changes in an attentive design optimization with corresponding thermal heating-cooling changes (HVAC) in the building [7].

Studies about hotels can be defined as local energy consumption analyses, per m² as well and process analyses. A sustainable model about energy performance evaluation of hotels with exergy analysis has not been observed in the literature. First, this study was presented by the pre-energy audit of a hotel, which was considered under insulated and uninsulated conditions with real data. In this study, occupancy rate and per m² area were considered as a reference parameter for analyses. Energy and exergy analyses for each one of two situations were calculated CO₂ emissions dependent on irreversibility and energy losses. Besides, energy and emission capacity per a customer according to occupancy rate, energy saving potential according to improvement potential were found separately.

2. Energy management and energy audit at hotels

The global consumption of energy by hotels is approximately 360 MToe, which has an important effect on the environment due to the activities and energy-based infrastructures of hotels. Considering the hotel sector, Europe hotels have approximately a potential of 42% and 5.45 million beds capacity. According to a study made for these hotels, the average energy consumption was defined between 305 and 330 kWh/m².yr with an average emissions release of 160-200 kgCO₂/m². The energy consumed by hotels is derived mostly from fossil fuels. Natural gas and fossil fuels generate approximately 39% of the total energy for a typical hotel, whereas electricity generates approximately 61% of the total consumption for a typical hotel. When analyzing the activity structure of hotels, energy is used for heating, cooling, conditioning, lighting, and ventilation. The usage of heating requirements depends on the operations of building heating, swimming pools, and cooking [2]. According to energy savings studies that considered capacity and usage rates in hotels, maximum energy savings potentials of 30% were attained. Energy savings potentials are dependent on the place of use; in hotels in Europe, the distribution of energy use is as follows: 15-20% in heating, 5-30% in cooling, 40-70% in water heating and 7-40% in lighting [8].

Considering the costs of annual energy consumption of hotel, there is a need for effective and sustainable energy management. Energy management for hotels is defined as a disciplined study that is structured and organized for the efficient use of energy without sacrificing environmental conditions, service quality, comfort, and safety. This system in Turkey can be provided with an ISO 50001 Energy Management System. [9]. Effective energy management is a dynamic structure that progresses within a cycle of monitoring, planning, implementing, controlling and measuring. The primary task of energy

management is dependent on the capability of an organization to effectively determine all energy processes and savings potentials with pre-energy searching.

3. Exergetic approach in integrated building

The primary objective of effective and sustainable energy methods is to maximize the energy savings potentials through the use of energy searching attached to a targeted consumption. An analysis for each energy-consuming system is important for determining the aspects required for subsequent improvements. A flow chart of the exergetic approach developed for building implementations is shown in Fig. 1.

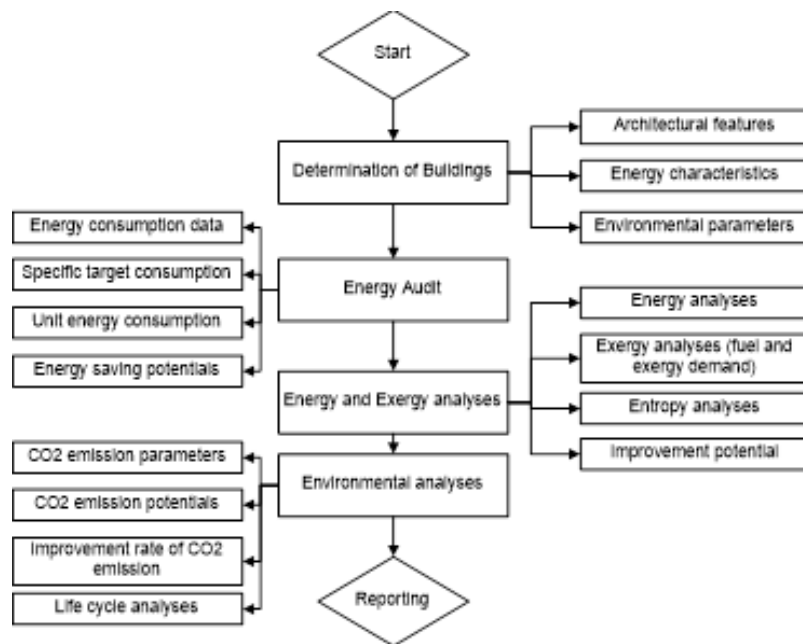


Fig. 1. Flowchart of the exergetic approach for buildings

Step 1: Energy Audit

Exergetic analysis of the process shows directly a useful performance related to irreversibility. But previously from this analysis, distribution of energy consumption of all processes should be examined and process to be studied should be determined. An energy audit is the most important stage of the methodology for developing efficiency and determining the energy savings potential. The most important stage of an energy audit is the data collection process. The data collection process requires a strategic approach to energy management. The collected data should be transformed into a standard structure, and their unit transformation should be ensured by a unit analysis. Energy management standards determine standard, target energy consumptions and energy savings potentials. The standard equation of consumption is a linear equation that demonstrates that the need for energy is dependent on specific variables. This equation is expressed as;

$$E = a + b(P) \quad (1)$$

Where the variables “a” and “b” are fixed, and P is a specific variable. After the standard equation dependent, targets are determined by considering consumption processes. The target equation is the

same form as the standard equation. To determine the energy savings potential, the cumulative sum value (CUSUM) method is employed. This method consists of determining the total cumulative sum of the energy savings potentials from the energy data using the least squares method [10].

Step 2: Exergy analysis

Energy demands of residential or commercial buildings are generally determined as based on heat losses and gain. Energy demands in these buildings are assessed for demands, comfort conditions and thermal losses during the project process. The energy demand based on heating for a building (\dot{Q}_m) is;

$$\dot{Q}_m = [\dot{Q}_h(T_{in} - T_{out}) - \varphi_m(\phi_{in,m} + \phi_{out,m})] \cdot t \quad (2)$$

Where \dot{Q}_h is specific heat losses of the building, $(T_{in} - T_{out})$ is monthly the average inlet and outlet temperature, φ_m is the utilization factor, ϕ_i and $\phi_{s,m}$ represents average inlet gains and average solar energy gains respectively, and t is time [11]. Fossil fuels are generally used as the primary energy source to supply heat demands in the buildings. The amount of fuel for the total energy load (M_f) is;

$$M_{fuel} = \frac{\dot{Q}_{heat,year}}{LHV_{fuel} \cdot \eta_{boiler}} \quad (3)$$

Where LHV_{fuel} is the low heat value of the fuel and η_u is the thermal efficiency of the boiler or heat supplier [11]. The total energy efficiency of a heating system is the ratio of annual energy demand to annual fuel consumption. According to this, the total efficiency is;

$$\eta_I = \frac{\dot{Q}_{heat,year}}{M_{fuel,year} \cdot LHV} \quad (4)$$

Where η_I is the total energy efficiency, $\dot{Q}_{heat,year}$ is the demand for heating energy, and $M_{fuel,year}$ is the annual fuel consumption. Considering the heat requirements of the buildings, thermal exergy is addressed accordingly heating and cooling demands related to minimum energy or fuel usage. The exergy factor firstly is the minimum exergy or heat demand depending on Carnot efficiency between inlet and output or dead state temperature. Exergy factor can also be described as the rate of energy and exergy demand for buildings. It can even be thought as a ratio of the real need in buildings to will be consumed with energy. In this case, the (γ) exergy factor is,

$$\gamma = \frac{\dot{E}_x}{\dot{Q}_h} = \left(1 - \frac{T_0}{T}\right) \quad (5)$$

The exergy demand of a building can be considered as minimum energy demand accordingly internal comfort requirements, indoor and output temperature together with on structure components directly dead state temperature. The exergy demand is,

$$\dot{E}_x = \dot{Q}_h \cdot \left(1 - \frac{T_0}{T}\right) \quad (6)$$

Where \dot{Q}_h is the total heat demand of the building, T_0 is the dead state temperature or outdoor temperature, and T is the ambient temperature [9,12,13]. The exergy load rate for buildings is dependent on the exergy load of the heating system and the exergy demand rate of the distribution system. The total system exergy of buildings depends on the heating system, the distribution system and other components that consume energy, such as DHW, HVAC or heat pump systems. The total system exergy load rate of the building becomes

$$\dot{E}_{x_{total}} = \dot{E}_{x_{HS,in}} + \dot{E}_{x_{dis,in}} + \dot{E}_{x_{DHW,in}} + \dot{E}_{x_{other,in}} + \sum P_{sys,in} \quad (7)$$

Where $\dot{E}x_{HS,in}$ is the exergy load of the heating system, $\dot{E}x_{dis}$ is the exergy load rate of the distribution system, $\dot{E}x_{DHW,in}$ is the exergy load rate of the domestic water heater, $\dot{E}x_{other,in}$ is other component that consume energy, and $\sum P_{sys,in}$ is the electric power consumption of all systems. The total exergy efficiency of buildings based on the demand exergy rate:

$$\varphi = \frac{\dot{E}x_{demand}}{\dot{E}x_{total}} \quad (8)$$

Exergy is consumed in all thermal systems that are dependent on environmental conditions[9,12,13]. Therefore, the exergy destruction rate is an important parameter for assessing irreversibility and the entropy production of systems. The exergy destruction rate of the system can be calculated by;

$$\dot{E}x_{dest} = (1 - \psi_{sys}) \cdot \dot{E}x_{total} \quad (9)$$

The rational exergy efficiency is the most accurate criteria for exergy efficiency related to building energy system[14].

The improvement of exergy efficiency for an energy process or system is based on to minimize the exergy loss or irreversibility. The exergy loss or irreversibility is based on the exergy difference between input and output of the system. The improvement potential (IP) is defined for irreversible processes of energy systems as follows [15,16]:

$$IP = (1 - \eta_{II}) \cdot (\dot{E}x_{in} - \dot{E}x_{out}) \quad (10)$$

Step 3: CO₂ Emission Analysis

The United Nations Environment Program can be seen at the top of these organizations, and according to the 4th evaluation report, the amount of CO₂ emission was delimited by 450 ppm. According to the pre-industrialization value (280 ppm), this value has been expected to rise global temperature as 2 °C. In recent years, scientific researches have brought to light that the target level should be limited to 350 ppm related to boundary condition in which environmental cycles can occur, as this limit would not result in climate change [17].

CO₂ emissions are considered in two aspects. The first aspect is the amount of CO₂ emitted from burning fossil fuels. The second aspect is the equivalent amount of CO₂. This criterion is described as a criterion for evaluating the global warming potential (GWP) and accepted as the equivalent potential of greenhouse gases like CH₄ and N₂O, emitted by especially fossil fuel consuming systems. (GWP_{N2O}: 21 and GWP_{CH4}:.310). The conversion factor between these two criteria is 7.78 GtCO₂ considering unit ppmCO₂ [17]. CO₂ emission assessment of buildings is defined considering energy consumption and relationship of the emissions and the energy is expressed by the following equation.

$$E_{p,SEG} = 100 * (SEG_a / SEG_r) \quad (11)$$

Where SEG (kg-CO₂/m²year) states to the annual CO₂ rate for per m². “a” and “r” indies expresses to real and reference conditions, respectively. The emissions value of buildings is related to energy consumed and each fuel consumed has an emission factor (F_{SEG}). According to this, total emission potential is calculated as below;

$$SEG = m_{fuel} \cdot F_{SEG} \quad (12)$$

Where F_{SEG} refers to the CO₂ emission factor for each fuel like natural gas (0.234) and coal(0.433) [18,19]. The CO₂ emission metrics related to the exergy concept is defined as another method in emissions analyses.

4. Results and discussions

In this section, the exergetic approach suggested for a hotel were applied considering a sample hotel, which has two cases including isolated and uninsulated conditions. But first, energy efficiency potential was defined based on an energy audit. Then, energy and exergy analyses of the hotel were made consequently. Structural features of the hotel were given below:

4.1. Structural Features of Hotel

The hotel was built in provincial borders of Bursa/Turkey, and its construction is a concrete building. Energy consumption of the hotel depends on electric and natural gas. The building's central air conditioning system is powered by steam for steam humidification. Alternatives energy systems (such as renewable) except the standard energy sources was not supported in the building. Construction components were assessed separately for building energy requirement values. The floor area of the ground contact is 2152 m², the total area of the window is 1442.42 m², and the total area of the doors is 13.57 m². The total area of the wall in the project is 6693.45 m², and the total terrace and roof area is 2092.97 m². The total m² measurement for the closed area of the hotel is 13253.04 m². In this study, for the analytic assessment in uninsulated (Case I) and insulated (Case II) conditions were separately addressed.

4.2. Results of the Analysis and Evaluations

During energy audits of the hotel, the analyses for Case I and Case II conditions examined at two-way, which were defined m² consumption and the occupancy rate. These parameters were analyzed separately considering annual consumptions.. The energy consumption distributions for both analyses are given in Table 1.

Table 1 Table 1 Energy consumption distributions of the hotel for the years of Case I and Case II

| Case | Energy | Distribution | Unit Cost | Cost | Distribution | Unit Energy Cost |
|-------------|------------|--------------|-----------|-----------|--------------|------------------|
| Case I | (kWh/year) | % | \$/unit | \$/Total | % | \$/unit |
| Electricity | 1389970.37 | 0.5599 | 0.091 | 126384.12 | 0.7609 | 0.091 |
| Natural gas | 1092611.46 | 0.4401 | 0.296 | 39713.14 | 0.2391 | 0.036 |
| Total | 2482581.83 | | | 166097.26 | | 0.067 |
| Case II | | | | | | |
| Electricity | 1406277.33 | 0.5969 | 0.164 | 230629.48 | 0.8505 | 0.164 |
| Natural gas | 949498.50 | 0.4031 | 0.41 | 40551.05 | 0.1495 | 0.043 |
| Total | 2355775.83 | | | 271180.53 | | 0.115 |

For Case I and Case II, the energy consumption for the hotel was 230.22 Toe and 211.85 Toe, respectively; the unit energy annual cost was found 0.067 \$/kWh for Case I and 0.115 \$/kWh for Case II. The energy consumption assessments for the hotels are generally performed using m² as a reference. However, the occupancy rates in hotels are directly affected by the cost effectiveness. In this study, energy savings potentials were calculated using the m² and the occupancy rate as references.

According to the audit results, the standard annual average m² consumption for the Case I was found 16.83 kWh/m², and the target consumption was defined 12.43 kWh/m² with a decreasing rate of 36.6%. For the Case II, the standard consumption was 14.81 kWh/m², and the target consumption was 7.64 kWh/m² with a rate of 48%. Similar analyses were conducted using the energy consumption per capita, which is dependent on the occupancy rate of the hotel. The occupancy rates for an insulated building in Case I and Case II were found 74.64% and 51.77%, respectively. Standard consumption was calculated as 1.56 kWh/person in Case I and 1.95 in Case II. Considering capacity, the target consumptions were 1.13 kWh/person in Case I and 1.10 kWh/person in Case II. According to this distribution, the annual average energy savings for Case II was 59.7% for m² and the savings per capita was 43.8%; in Case I, the savings rates per m² and per capita were 36.6% and 27.3%, respectively

Based on the audit of a building, the cumulative total values chart (CUSUM) was only created for Case II. Based on the total consumption values for Case II, the CUSUM chart was generated using the least squares method, as shown in Fig. 2.

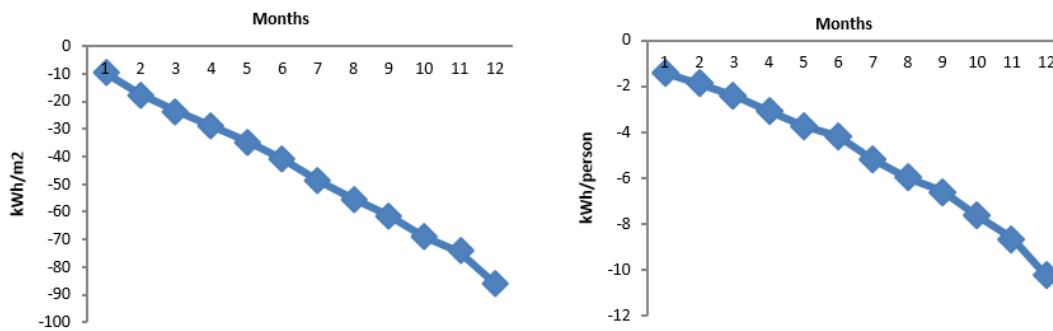


Fig.2. CUSUM charts

According to the CUSUM analyses, the savings potential was 7.16 kWh for m² and 48.4% and 0.86 kWh and 43.9% per person depending on the occupancy rate. The difference was less than 10% for both potentials. The audit results, which are dependent on insulated and uninsulated conditions of the hotel, indicate a significant savings potential for the hotel. Based on these assessments, energy and exergy analyses of the hotel were made separately.

The energy sources in the hotel were natural gas and electric. The analyses were performed for the consumptions of the mechanical system by employing the consumed energy charges to satisfy the need for energy produced from the loss of heat outside of the kitchen and hot water required for laundry. The energy consumption distributions for both situations are given in Fig.3.

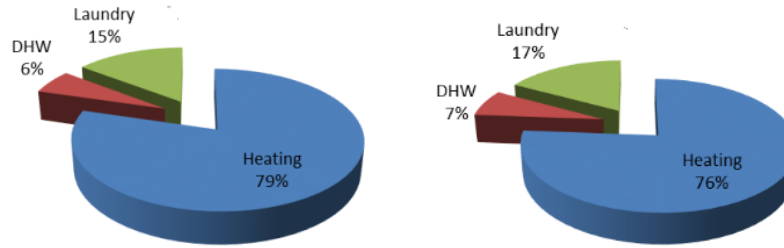


Fig.3. Energy consumption distribution for the hotel

In both usage conditions, the % variation in the energy consumption distribution is approximately 4.25%. Insulation support provided savings at a rate of 43.08%. When disregarding the effect of external air changes, the annual energy consumption decreased to 348203.5 kWh/year from 611323.1 kWh/year. From these data, the monthly energy efficiencies of the hotel were calculated; the distributions are shown in Fig. 4.

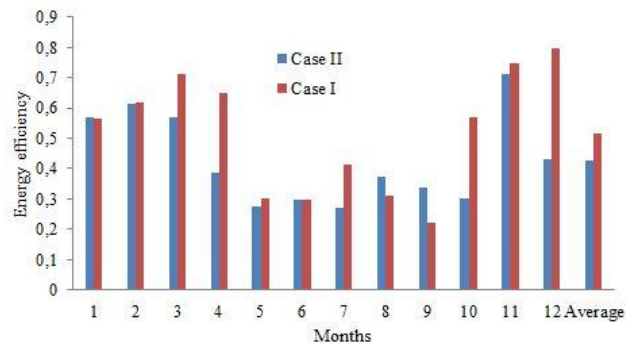


Fig.4. Energy efficiency in the hotel for Case I and Case II

In the analyses, reference values were calculated by considering the hot water demand of facilities, the individual hot water demand and loss of heat analyses. The results of the analyses indicate that the efficiency of the system is higher for uninsulated usage. The average energy efficiency was 51.72% and 42.84% in Case I and Case II, respectively. Although there is an improving effect of insulation at the rate of 43.08% in the heating requirement, other consumptions in the hotel create significant losses due to operational inefficiencies.

These results indicate that the distribution of energy consumption was directly affected by the occupancy rate of the hotel. The results of an important advantage, such as insulation, did not provide sufficient savings because a control could not be applied that was dependent on the occupancy rate of the hotel or the system did not allow this application. This distribution was also obtained with the unit hour energy consumption of energy based on the demand for natural gas. The unit energy consumption distribution for the hotel for both situations is shown in Fig. 5.

The monthly unit energy consumptions do not exhibit significant differences. An analysis of these values reveals that the annual average unit energy consumption is higher for the insulated year at a rate of 3.19%. The average unit consumption for Case I was 0.779 kWh, whereas the average unit consumption for Case II was 0.804 kWh. The difference of 30.7% in the occupancy rate of the hotel is important. No system was able to control this change in the mechanical infrastructure of the hotel.

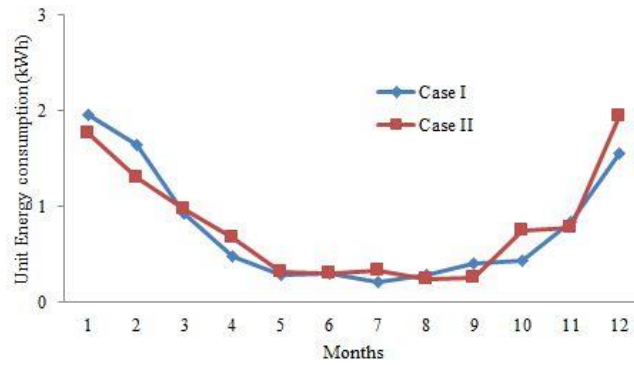


Fig.5. Energy consumption distribution for Case I and II

Concerning energy analyses of the total system distribution, the effect of consumption also yielded results that were similar to the exergy distribution. Building exergy analyses can be performed separately based on fuel and building exergy demands. If building demands cannot be directly measured in a system, the exergy analyses and efficiency of the system can be determined regarding fuel. Both approaches were analyzed in this study. The exergy consumption of the system was separately analyzed with fuel consumption as a reference, and the monthly average exergy efficiency of the hotel was calculated. The average exergy efficiency for both situations is shown in Fig. 6.

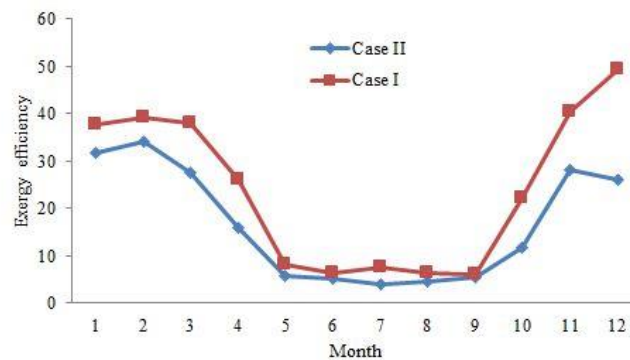


Fig.6. Exergy efficiencies of the hotel based on the fuel

As in the energy analyses, the average exergy efficiency in Case I was higher than the average exergy efficiency in Case II at a rate of 30.57%. The average exergy efficiency for both years was 23.02% (Case I) and 15.97%, respectively. These assessments were performed by considering the charge analyses, such as loss and gain of heat, mechanical systems, boiler and laundry, and the results were compared. In the exergy demand analyses, the efficiency was 27.31% in Case I and 16.26% in Case II. These values are close to the results obtained from the fuel exergy approach at an average error rate of 10%. To display the operating charges, the results from the demand exergy approach require more detailed analyses. Thus, these charge values can be used to define the improvement potentials related to irreversibility caused by the energy consumptions of the hotel. Entropy production based on equation (14) and the related improvement potential were calculated separately. Only data for Case II were employed for future scenarios. The entropy production and improvement potential of the exergy consumption for Case II are shown in Fig. 7.

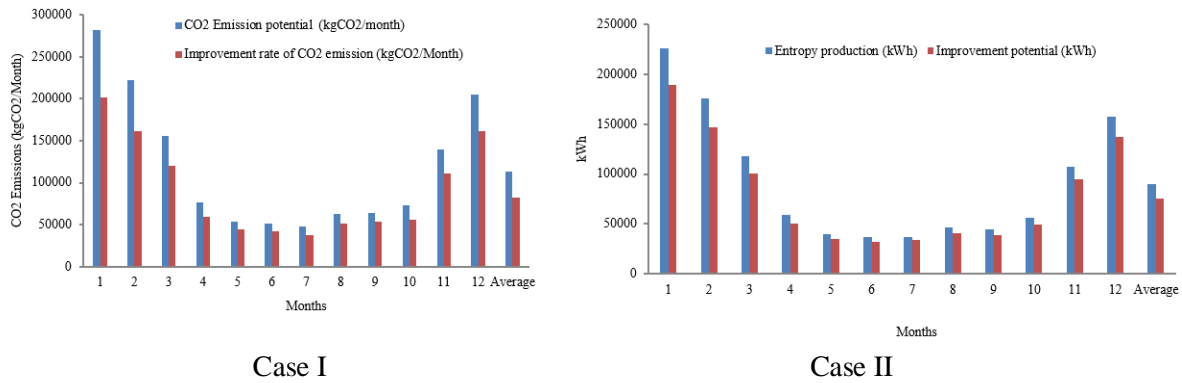


Fig.7. Entropy production and improvement potential of the hotel

In the exergy production of the hotel for the year Case II, the irreversibility for monthly average, lost exergy or entropy production amount to 89800.36 kWh. The improvement potential of this effect was 56657.29 kWh. The improvement in this potential increases the exergy efficiency of the hotel at the rate of 80.15%. With adequate energy management of the hotel and effective energy usage, the improvement of this potential and emission release based on energy consumption will be positively affected.

Emission approaches in energy systems differ in many aspects. The carbon release metric was employed in this study, and CO₂ emission savings based on the improvement potential with current emission release in the system were separately calculated; the results are shown in Fig. 8.

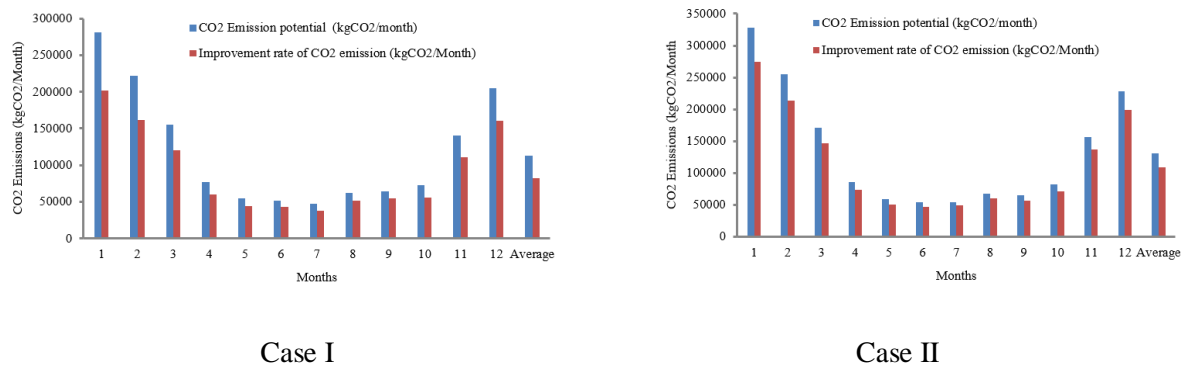


Fig.8. CO₂ Emission potential and improvement rate of the hotel

Regarding energy consumption, the monthly average for the year Case I was 77946.93 kWh, and the CO₂ emission potential for the hotel causing entropy production was 113.24 Gt. Considering the improvement rate, emission savings at a rate of 39.68% emerges in the monthly average of this potential. The exergy loss of the hotel based on the irreversibility in Case II was 89800.36 kWh. The improvement potential based on the exergy efficiency of the system was 83.74%. The average monthly CO₂ emission potential of the system was 130.46 Gt.CO₂. This potential can be reduced at a rate of 23.62% via an improvement based on this potential improvement rate.

For buildings and building elements, a comparative methodology framework as namely cost-optimal methodology, which is levels of minimum energy performance requirements, was published by the European Commission on 30 June 2011.

This methodology evaluates the energy performance considering the lowest cost during the estimated economic life-cycle, cost-optimal methods have many units related to energy consumption[20,21]. In this study, the present value of energy consumption is used for cost-optimal considering target consumptions of the energy audit in insulated and uninsulated conditions. Occupancy rate and m^2 parameters were taken references and results were given Fig.9.

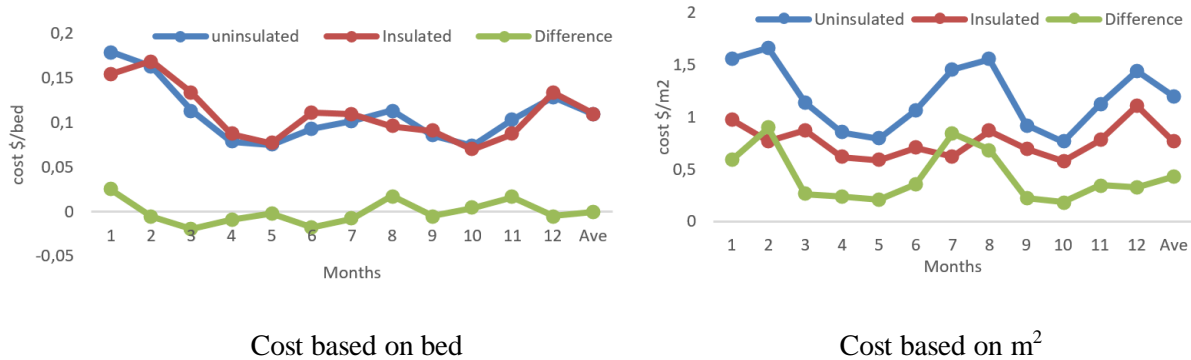


Fig.9. The global cost of the energy consumption for bed and m^2

Energy consumptions in hotels must be evaluated together with climatic conditions. But the energy consumption is also an important aspect of cost-effectiveness except for the efficiency. In this context, the global cost has been found both for occupancy rate and m^2 referred to objective consumptions by present value. According to this evaluation, energy consumption per bed for isolated and un-isolated buildings have been found respectively 0.108 \$/bed and 0.1097 \$/bed. Global costs for consumptions have been found meanly 1,194 \$/ m^2 and 0,765 \$/ m^2 at the same conditions.

5. Conclusions

In this study, an analytic method referred to as the exergetic approach was developed as the reference for the energy management considering thermodynamic and environmental analyses. The results of the study show that not only the construction specifications but also the operating structure should be evaluated as essential parameters in hotels. In this context, the improvement between uninsulated and insulated conditions with a rate of 43.08% were found except for the problems in the energy management structures of the hotel. The results taken from the analysis were given as follows:

- a. According to the results received from the energy audit of the hotel, the annual average energy savings of Case I was 59.7% for m^2 and 43.8% for saving per capita. The savings rates for m^2 and per capita for Case II were 36.6% and 27.3%, respectively.
- b. The savings potential of the hotel as a cumulative total based on occupancy rate was of 43.9% with 0.86 kWh per capita energy consumption and 48.4% with 7.16 kWh energy consumption for m^2 .
- c. Although high-efficiency elements are used in the energy system of the hotel, the energy efficiency was 51.72% for Case I and 42.84% for Case II. The significant loss potential in the system was defined.
- d. When assessing the exergy efficiency of the hotel based on fuel, the average exergy efficiency rate of 30.57% in Case I was higher than the exergy efficiency in insulated structure. The average exergy efficiency for both years was 23.02% (uninsulated structure) and 15.97%, respectively. However, the

exergy efficiency in the uninsulated structure was 27.31% and 16.26% in insulated structure, depending on the building demand and building usage.

e. The most important contribution of exergy analyses is the ability to define the improvement rate based on the loss potential. The exergetic efficiency of a hotel can be increased to 80.3% depending on the improvement rate of the hotel.

f. The improvement rate in exergetic analyses can be used as a guide to define the CO₂ emission savings potential of the hotel concerning environmental effects. Thus, the CO₂ emission savings rates of the hotel were 39.68% and 23.62% in uninsulated structure and insulated structure, respectively.

g. These analyses demonstrated the importance of structuring an effective energy management system for the considerable consumption of energy by hotels. The positive effects of some improvements in the system, such as insulation, did not result in financial savings for this hotel because the energy could not be effectively managed and efficiently employed. These improvement studies should be based on useful engineering studies.

Hotels have significant potential in the building and tourism sectors and have become prominent due to not only their energy consumption but also their environmental effects. This study is important because it indicates that effective energy management can be ensured with the proposed exergetic approach, mainly through conducting energy analyses. This study was performed using a method for defining the unit energy value in hotels. In this respect, this study has importance for a sustainable environment and sustainable life-cycle cost analyses.

References

- [1] Karataş M., Babür S., Role of Tourism Sector in the Developing World, *KMÜ Journal of Social and Economic Resarches*, 15 (25): 15-24, 2013 (TR)
- [2] WTO, Analysis on Energy Use by European Hotels: Online Survey and Desk Research, Hotel Energy Solutions project publications, Revised version, July 2011, Madrid, Spain, www.unwto.org.
- [3] Lohani S.P. Energy and exergy analysis of fossil plant and heat pump building heating system at two different dead-state temperatures, *Energy* Volume 35, Issue 8, August 2010, Pages 3323-3331.
- [4] Kondo, K. Energy and exergy utilization efficiencies in the Japanese residential/commercial sectors. *Energy Policy* 2009, 37, 3475–3483.
- [5] Gonçalves P., Rodrigues Gaspar A., Gameiro da Silva M., Energy and exergy-based indicators for the energy performance assessment of a hotel building, *Energy and Buildings* 52 (2012) 181–188.
- [6] Xydis G., Koroneos C., Polyzakis A., Energy and exergy analysis of the Greek hotel sector: An application, *Energy and Buildings* 41 (2009) 402–406.
- [7] Kilkis B., An Exergy Aware Optimization and Control Algorithm for Sustainable Buildings, *International Journal of Green Energy*. 01/2004; No. 1:65-77. DOI:10.1081/GE-120027884.

- [8] Alujević V. Z., Energy Use and Environmental Impact from Hotels on the Adriatic Coast in Croatia - Current Status and Future Possibilities for HVAC Systems, Doctoral Thesis, Department of Energy Technology Division of Applied Thermodynamics and Refrigeration Royal Institute of Technology Stockholm, Sweden 2006
- [9] Hepbasli A. Low exergy (LowEx) heating and cooling systems for sustainable buildings and societies, *Renewable and Sustainable Energy Reviews* 16 (2012) 73– 104
- [10] Kedici Ö., Energy management, General Directorate of Electrical Power Resources Survey and Development Administration Energy Resources Studies Department, Ankara, Turkey, 1993
- [11] Koçak S., Şaşmaz C., Atmaca İ., Examination from the technical and economic aspects of a shopping center for degree-days of different regions according to TS825 isolated, *Journal of Installations Engineering* Volume 128, 2012, pp. 76-88
- [12] ECBCS, Annex 37 2013, Energy conservation in buildings and community systems-low exergy systems for heating and cooling of buildings, *Energy Conservation in Buildings and Community Systems* <<http://virtual.vtt.fi/annex37/>> (01.12.13).
- [13] ECBCS, Annex 49, 2013, Energy conservation in buildings and community systems low exergy systems for high performance buildings and communities, *Energy Conservation in Buildings and Community Systems* <<http://www.annex49.com>> (01.12.13).
- [14] Cornelissen R.L. 1997, Thermodynamics and sustainable development: The use of exergy analysis and the reduction of irreversibility, Ph.D thesis, University of Twente, The Netherlands.
- [15] Van Gool W, Energy policy: fairly tales and factualities, In: *Innovation and Technology-Strategies and Policies* (Eds O.D.D. Soares, A. Martins da Cruz, G. Costa Pereira, I.M.R.T. Soares and A.J.P.S. Reis), Kluwer, Dordrecht, 1997;93-105.
- [16] Hammond G.P, Stapleton A.J., Exergy analysis of the United Kingdom energy system. *Proc Instn Mech Engrs* 2001;215(2): 141-162.
- [17] Algedik Ö. Role of Local Government in the Fight Against Climate Change, Civil Climate Summit Report, the Organization of Civil Climate Summit, November, 2013
- [18] Bayram M. The Reference Building Concepts And Energy Classification in calculation Method of Bep-TR, X. National Installation Engineering Congress – April 13/16 /İzmir, page 755-762, 2011
- [19] Sogut M. Ziya, Hamit M., Tahir H. K., and Namik I. Investigation of effects of hydraulic balance in mechanical system based on energetic and exergetic efficiency in industrial buildings", *International Journal of Exergy*, 2016.

- [20] Becchio C., Ferrando D. G., Fregonara E., Milani N., Quercia C., Serra V., The cost optimal methodology for evaluating the energy retrofit of an ex-industrial building in Turin, *Energy Procedia* 78 (2015) 1039 – 1044.
- [21] Pearce C., *Harmonised Cost Optimal Methodologies for the Energy Performance in Buildings Directive, EEB Principles to Calculate Minimum Energy Performance, Requirements in Buildings*, April 2010, European Environmental Bureau (aisbl); Blvd de Waterloo 34, 1000 Brussels, Belgium

ORGANIC MATERIAL POTENTIAL AND ENERGY ANALYSIS FOR BIOGAS APPLICATION OF BATMAN

Muhammed Enis YILDIZ¹, Özbay ÇAĞIRTEKİN², Adem YILMAZ³

With the decrease of fossil fuels in the world, increasing energy costs caused the countries to turn to different kinds of energy sources. One of these sources is biogas energy which is a renewable energy source. Biogasorganic is a kind of energy resulting from the fermentation of domestic and industrial wastes indoor environment.

In this study, biogas amounts and energy analysis which can be obtained by determining the potentials of organic (animal and herbal) wastes belonging to Batman province have been made. As a result of the researches, 52% of the total wastes in the province of Batman are composed of organic wastes. According to the data obtained in the calculations; It has been found that the biogas production potential in Batman province is 115,745 m³ / day biogas and 544,000 KWh / day electrical energy from the wastes and 1.563 m³ / day biogas and 7.346 KWh / day electrical energy from the vegetable wastes. The obtained data are given in table and graph

Key words: Biogas, Fermentation, Animal Waste, Herbal Waste


1. INTRODUCTION


Nowadays, it is seen that fossil fuels are gradually decreasing and countries are turning to renewable energy sources within the scope of their efforts to diversify their energy needs. Biogas which does not harm to environment is seen as a renewable energy source cause it can be obtained continuously in nature. Biogas energy, agriculture and livestock activities as a result of the production of vegetable and animal waste produced by biogas production facilities by oxygen-free respiration (fermentation) by bacteria is broken by the resulting methane (CH₄) is used as fuel and energy products. It's also evaluate that like as a result of fermentation in fertilizers for use in agriculture.

As a result of the reduction in natural energy resources and the search for new resources, biogas production from organic wastes is considered as an alternative source. The use of organic wastes in the production of biogas is an effective waste management step in both waste disposal and energy generation.[1]

Biogas is a colorless, flammable gas, depending on the structure and process of organic matter, containing 60-70% CH₄, 30-40% CO₂ and low amount H₂S, N, H, CO. The fuel equivalent of biogas is 0.60-0.65 L petroleum / m³ biogas [2],[3].

¹ Graduate School Of Natural And Applied Sciences /Batman University (mymenis@hotmail.com)  <https://orcid.org/0000-0002-7276-6385>

² Graduate School of Natural And Applied Sciences /Batman University (ozbaycagirtekin@hotmail.com)  <https://orcid.org/0000-0002-9812-4268>

³ Faculty Of Technology /Batman University (adem.yilmaz@batman.edu.tr)  <http://orcid.org/0000-0001-7266-0866>

It is important to evaluate that biomass energy, which is one of the renewable energy sources, has increased in recent years, increase in utilization rates, and within the scope of energy efficiency applications and the diversity of energy resources. For this purpose, there are various breakthroughs in the world. In the coming years, it is predicted that the biofuel products that will be obtained with the conversion of traditional biomass to the bioenergy in modern facilities will have an important place among the renewable energy sources. [4]

In our country, animal manure is burned for heating and cooking purposes. The use of animal manure in agricultural production is more economical than conversion to energy. Animal manure has superior properties than artificial fertilizers. It is possible to prevent the incineration of animal manure and to give it to the agricultural land by giving a new energy to the rural area to replace this energy. This energy is biogas that can be obtained from animal manure.[5]

Which can be related to the biomass potential that exists in our country with statistical data of Turkey's annual biomass potential of about 32 MTOE, while total converted to bioenergy potential is said to be about 16.92 MTOE. [6] 73 units in Turkey biogas, biomass, waste heat and power plant pyrolysis oil. The total installed capacity of these power plants is approximately 395.0 MW. [7]

Considering the studies on the use of biogas energy; The biogas energy produced from animal wastes in our country shows that the energy value is between 3 and 3.5 billion m^3 / year. [8]. If the biogas potential of urban solid wastes is 4,850 million kWh / year and 1% of the processed agricultural land is used for energy plant cultivation, it is determined that the biogas potential will be 25.95 billion kWh / year and that the biogas potential of animal manure will be 14.26 billion kWh / year [9]. The annual biogas energy potential for animal waste originating from Iğdır city is estimated to be 21.441 million m^3 [10]. It has been shown that approximately 87,645 m^3 / daily biogas can be produced from biogas plants from animal manure in Malatya. [11]. When the theoretical biogas energy value which can be produced from organic wastes for Ankara city is considered as m^3 / day, it is found as 277.348 m^3 / daily from animal wastes, 38.493 m^3 / daily from agricultural wastes and 160.380 m^3 / daily from kitchen wastes [12].

In Batman province, agricultural activities have gained importance with the development of irrigation conditions as well as animal husbandry. In many fields wheat, corn and lentil cereal products are planted. However, after harvesting the crops, unfortunately, the remaining stubbles are burned unconsciously and they endanger human health while damaging the environment and natural life. While many land becomes a flame ball, an important energy source is wasted in front of us.

Batman province has a significant waste potential both in livestock and agriculture and their evaluation is of great importance both for the solution of environmental problems and for alternative energy sources.

2. METHOD

Statistical data and web pages were used to determine the amount of organic waste in Batman province. The different data obtained have been brought into tables and graphs. The collected data were calculated by using scientific calculations and transformations. Biogas potential and daily / yearly energy analyzes were calculated from animal and vegetable wastes in Batman province. While the data were collected, the changes in the last few years were taken into consideration. Calculations have been made by taking into account the serious decreases and increases that may occur in years.

In order to calculate the amount of fertilizer to be formed from animal wastes, animal manure production volume (ton / year) and the amount of biogas (m^3 / year) that can be obtained are given according to animal species. The electrical energy that can be produced on an annual basis according to the amount of 4.70 kWh electricity corresponding to 1 m^3 biogas is calculated. Energy production potentials which are mixed with the amount of biogas obtained from agricultural wastes are calculated daily and yearly.

The energy value of methane gas obtained from cattle, sheep and poultry and the amounts of energy that can be taken from agricultural wastes are shown as numerical data, graphs and tables.

3. DISCUSSION

When the amount of solid waste in Batman province is examined, organic wastes constitute the biggest share with 52%. Organic waste is divided into two different categories. The first is animal waste. These are the wastes of cattle, sheep and poultry and slaughter waste. The second is herbal waste. These are straw, finely chopped stalks, maize residues, sugar beet leaves, and waste from the untreated parts of plants..

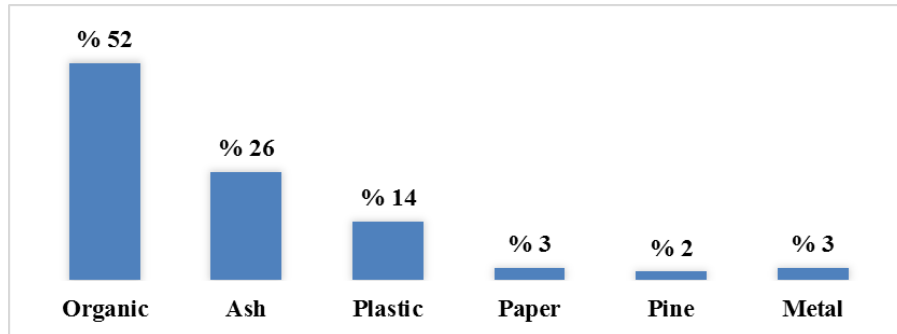


Figure 1. Waste Composition in Batman Province in 2017[13]

3.1. Animal Wastes

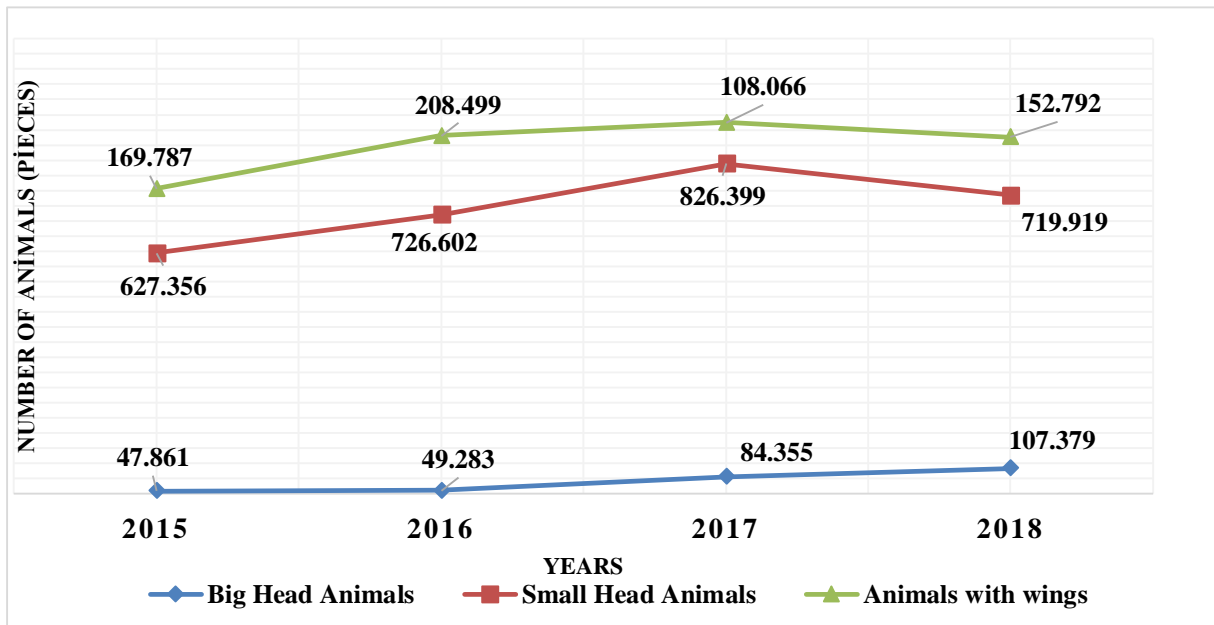


Figure- 2 Batman Province Animal Numbers by Years [14]

When we look at the statistical data of Batman province in animal husbandry field, in 2018, we see that most small small head animals (719.919) followed by animals with wings (152.792) and finally big head animals (107.379). When we look at the data of the last four years, it is observed that there is generally an increase in cattle and sheep and livestock breeding but there is a decrease in poultry husbandry. Table 1 below shows the number of animals on the basis of districts.

When the number of animals raised in Batman province is examined, it is seen that the number of big head animals in terms of biogas potential is less than the number of small head animals. According

to the population density of Batman province, the majority of big head animals are raised in Kozluk and the majority of small cattle and poultry are grown in the central and central villages.

Table 1 Number of Cattle, Sheep and Poultry by Batman Province [14]

| District Name | Big Head Animals | Small Head Animals | Animals With Wings |
|---------------|------------------|--------------------|--------------------|
| Merkez | 22.038 | 291.817 | 77.010 |
| Beşiri | 6.861 | 163.286 | 53.350 |
| Gercüş | 4.662 | 68.418 | 11.142 |
| Hasankeyf | 1.095 | 17.380 | 140 |
| Kozluk | 42.469 | 123.427 | 4.000 |
| Sason | 30.254 | 55.591 | 7.150 |
| Total | 107.379 | 719.919 | 152.792 |

When the average amount of fertilizer and biogas obtained from animal sources is examined, 5-6% of the big head animals weight is obtained in kg fertilizer / day, while 4-5% of sheep and goat weight is in kg fertilizer / day and 3-4% in chicken weight. 3 kg of fertilizer / day can be obtained. [15]

In order to calculate the biogas potential, the research results are used in Table 2 below.

Table 2. Energy Quantities from Animal Wastes [15]

| Animal Type | Age Fertilizer Tons / Year | Biogas m ³ / year |
|---------------------------|-------------------------------|---------------------------------|
| Big Hed Animals | 3,6 | 33 |
| Small Head Animals | 0,7 | 58 |
| Animals With Wings | 0,022 | 78 |

According to the data in the table according to the total number of animals in the province of Batman age fertilizer and biogas calculation;

For big head animals; = 386.564 tons / year fertilizer,
 For small head animals; 503.943 tons / year fertilizer,
 For animals with wings ; 3.361 tons / year of manure was found.

When the results are obtained, it is seen that the maximum amount of fertilizer can be obtained from small head animals in Batman province. Although the amount of biogas can be obtained from big head animals according to the table, the majority of biogas production potential constitutes the amount of fertilizer that can be obtained from small head animals because of small animal husbandry production in Batman province.

When the biogas calculation can be obtained from these collected fertilizers;
 For big head animals; = 12.756.612 m³ / year or 34.949 m³ / day biogas
 For small head animals; = 29.228.694 m³ / year or 80.078 m³ / day biogas
 For animals with wings; = 262.158 m³ / year or 718 m³ / day biogas was obtained.

The daily energy amounts that can be obtained from 1 m³ biogas under normal conditions are shown in Table 3 [16]

Table 3. Thermal Values of Biogas

| | | |
|----------------------------|-------------------|-------------------------------|
| 1 m ³ Biogas | Quantity of heat | 4700-5700 kcal/m ³ |
| | Oil | 0.62 lt |
| | Wood Coal | 1.46 kg |
| | Wood | 3.47 kg |
| | Butane Gas | 0.43 kg |
| | Turd | 12.3 kg |
| | Electrical Energy | 4.70 kWh |
| | Diesel | 0.66 lt |
| | Gasoline | 0.75 lt |
| | Propane | 0.25 m ³ |

4.70 kWh of electrical energy can be obtained from 1 m³ biogas. It was calculated that the total amount of biogas obtained from animal wastes for the province of Batman is converted into electrical energy and 544.000 KWh of electricity can be obtained daily. Table 4 below shows the amount of biogas and energy that can be obtained daily in Batman province according to animal species.

Table 4. Biogas and Electricity Quantities Obtained from Animal Wastes in Batman Province

| Animal Type | Amount of Biogas (m ³ /day) | Electrical Energy (kWh/day) | Available TL / day Price |
|---------------------------|--|-----------------------------|--------------------------|
| Big Hed Animals | 34.949 | 164.260 | 73.917 TL |
| Small Head Animals | 80.078 | 376.366 | 169.364 TL |
| Animals With Wings | 718 | 3.374 | 1.518 TL |

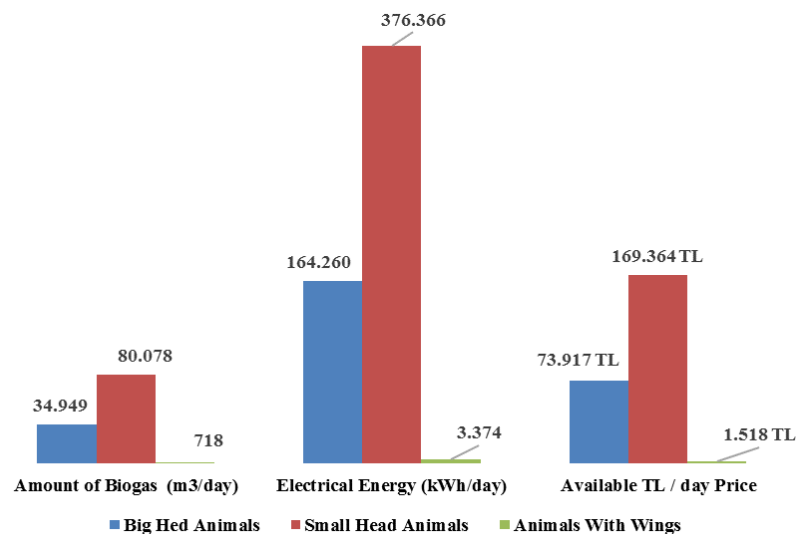


Figure-3 Biogas and Electricity Amounts Obtained from Animal Wastes for Batman Province

Turkey Statistics 1 kWh of electricity for the amount paid for housing, according to the Agency according to the average of 12:45 per month of June 2018 is. [17] According to the calculations, it was found that biogas from animal wastes would provide an economic contribution of approximately 244.799 TL in one day in Batman province.

When calculating the amount of biogas that can be obtained, the amount of energy that can be obtained if all of the organic wastes are collected is calculated. However, it is estimated that the loss rate will be around 30% when the fertilizers are collected in the pastures. When calculated according to this, the amount of energy that can be obtained daily in Batman province will be 380,800 kWh electricity energy.

3.2. Herbal Wastes

According to the data obtained from Batman Agriculture and Livestock Provincial Directorate of Agriculture for the province of Batman, biogas potential and daily / annual energy analyzes obtained from vegetable wastes were calculated. The data and the results of the research given in Table 5 are used for this purpose.

Table 5. Batman Province Herbal Product Amounts [14]

| SN | Name of the product | Planted Area (da) | Yield (kg/da) | Production (ton) |
|-----------------|---------------------|-------------------|---------------|------------------|
| 1 | Egypt | 45.858 | 1446 | 66.353 |
| 2 | Cotton (Mass) | 2.524 | 550 | 1.389 |
| 3 | Corn Silage | 6.000 | 4825 | 28.950 |
| 4 | Wheat | 64.862 | 375 | 24.346 |
| 5 | Wheat Juicy | 23.245 | 638 | 14.839 |
| 6 | Wheat Juicy | 32.423 | 519 | 16.835 |
| 7 | Wheat (Other) Dry | 416.180 | 341 | 142.169 |
| 8 | Barley (Other) Dry | 46.675 | 310 | 14.892 |
| 9 | Red Lentils Dry | 141.031 | 191 | 26.945 |
| 10 | Chickpeas Dry | 1.785 | 164 | 294 |
| Sown Area Total | | 780.583 | | |

The daily and annual production amounts of the biogas produced by the biogas calculation that can be obtained from the vegetable wastes collected in Batman province and the amount of daily and annual electricity energy of these products and the value added to be added to the country's economy are indicated in Table 6.

Approximately 10% of the total production amounts of wheat, corn, barley, chickpea and lentils are straw that can be used in biogas production. 1 kg. about 0.017 m³ of biogas can be obtained daily from the straw. [18]

With these data, the biogas production of the agricultural products that can be used in the biogas production of Batman province is calculated; 1.563 m³ / day biogas will be obtained from the straw of the products such as corn, lentil, wheat, barley and chickpea. Approximately, 60% of the obtained biogas is composed of methane gas. This is equivalent to about 937.8 m³ / day of methane gas. 1 m³ of methane is 10 kWh of energy. [18]

The daily and annual production amounts of the biogas produced when the biogas calculation can be obtained from the vegetable wastes to be collected in Batman province and the amount of daily and annual electricity energy of these products and their value added will be given in Table 6.

Table 6. Methane Gas and Electricity Quantities Obtained from Agricultural Wastes in Batman Province

| Agricultural Waste | Amount of Biogas | | Electrical Energy | | Available TL | |
|--|-----------------------|------------------------|-------------------|------------|--------------|---------------|
| | (m ³ /day) | (m ³ /year) | (kWh/day) | (kWh/year) | TL/day Price | TL/year Price |
| Corn, Wheat, Lentil, Chickpea, Barley (Straw, Stalk) | 1.563 | 570.495 | 7.346 | 2.681.290 | 3.305 | 1.206.580 |

According to the calculations, a biogas production of approximately 3.305 TL per day was calculated from vegetable wastes in Batman province.

According to the data in Table 6, when the total vegetable waste and biogas calculation is done in Batman province;

Corn, Wheat, Lentil, Chickpea, Barley (Straw) = 335.593 tons / year

When the biogas calculation can be obtained from these products;

For Corn, Wheat, Lentil, Chickpea, Barley (Straw, Stalk); = 570.495 m³ / year or 1.563 m³ / day biogas will be obtained.

4. RESULTS

In this study, biogas potential of Batman province and cost analysis in terms of savings are examined. According to the results, it is seen that there will be a significant economic benefit in case of establishment of plants in biogas production when considering the animal waste potential and agricultural areas in Batman province. In Batman province, organic wastes (animal and vegetable) constitute the largest share in terms of waste materials. Biogas production will reduce the burning of buckets in the villages, stubble fires that cause serious environmental pollution will be prevented. In addition, fertilizers used in biogas plants will be used more economically in post-processing agricultural areas to provide an economic benefit..

As a result of researches, 52% of total wastes in Batman province are composed of organic wastes. According to the data obtained in the calculations; It has been found that the biogas production potential in Batman province is 115,745 m³ / day biogas and 544,000 kWh / day electrical energy from vegetable wastes and 1,563 m³ / day biogas and 7,346 kWh / day electrical energy can be obtained from vegetable wastes. The results show that animal wastes are more advantageous in biogas production. However, the use of vegetable wastes as a source of biogas to transform both energy and rich fertilizers should not be ignored.

Our country is considered as an agricultural country in terms of its geographical location and economic structure. This potential needs to be evaluated and awareness raising should be established to increase biogas production. It is important to solve the energy problem of our country and to increase the renewable energy resources. At this point, more efficient use of solid wastes for biogas production will be useful.

5. REFERENCES

- [1] Mao C, Feng Y, Wang X, Ren G. "Review on research achievements of biogas from anaerobic digestion". Renewable and Sustainable Energy Reviews, 45, 540-555, 2015.
- [2] Speece RE. Anaerobic Biotechnology for Industrial Wastewater., Tennessee, USA, Arche Press 1996.

- [3] Deublein D, Steinhauser A. *Biogas from Waste and Renewable Resources*, ISBN: 978-3-527-32798-0, Weinheim, Germany, Wiley, 2008.
- [4] Marmara regions Magazine Issue 30, July - 2014 S.97-125 world and in Turkey Usage Status of Biomass Energy
- [5] Y. Ulusoy, H. Ünal ve K. Alibaş, “Biyogaz Üretimi Prosesi”, Uludağ Üniversitesi, Bursa.
- [6] Balat, M. (2005). “Use Of Biomass Sources For Energy In Turkey And AView To Biomass Potential”, *Biomass and Bioenergy*, Number: 29(2005,) p. 32-41.
- [7] Adem Y., Sinan Ü., Tufan K.,Abdulkadir K. *Biogas Production and Biogas Production Statistics Information in Turkey ISS-2017*
- [8] Arıkan B. *Investigation of the Efficiency of Biogas Production in Anaerobic Environment from Organic Domestic Solid Wastes*. Master Thesis, Çukurova University, Adana, Turkey, 2008
- [9] Özcan M, Öztürk S, Yıldırım M. “Determination of the biogas potential according to different resource types in Turkey”. *Energy Efficiency and Quality Symposium*, Kocaeli, Turkey, 12-13 May 2011
- [10] Altıkat S. Çelik A. “Biogas potential from animal waste of ığdır province”. *İğdır University. Journal of Graduate School of Natural and Applied Sciences*, 2(1), 61-66, 2012
- [11] Nilüfer Nacar Koçer, Gizem Kurt *Livestock potential and biogas production in Malatya*. *Sakarya University Journal of Science* 17. Skin, 1. Number, s. 1-8, 2013 SAU J. Sci. Vol 17, No 1, p. 1-8, 2013
- [12] Halil ŞENOL, Emre Aşkın ELİBOL, Ünsal AÇIKEL, Merve ŞENOL *Main Organic Waste Sources of Ankara for Biogas Production* *BEU Journal of Science* 6(2), 15-28, 2017
- [13] *Batman Provincial Directorate of Environment and Urbanization, Environmental Situation Report 2017*, pp 29
- [14] *Statistics Report of Batman Provincial Directorate of Agriculture*, 2018
- [15] <http://www.yegm.gov.tr/yenilenebilir/biyogaz.aspx> date access: 20.10.2018
- [16] <http://www.enerji.gov.tr/tr-TR/sayfalar/biyokutle> date access: 21.10.2018
- [17] <http://tuik.gov.tr/PreHaberBultenleri.do?id=27666> date access: 21.10.2018
- [18] Akbulut, A., Dikici, A., (2004). *Biogas Potential and Cost Analysis of Elazig Province, Eastern Anatolia Region*.

APPLICATION OF DECISION TREE METHODS FOR WIND SPEED ESTIMATION


H. Selcuk NOGAY^{1}, T. Cetin AKINCI²*


An area's wind speed forecasting is very important to investigate whether the area is available for wind power. The wind speed estimation has been carried out by means of other machine learning methods, mostly artificial neural networks. Because, in such methods, it is aimed to estimate the wind speed with the highest accuracy along with the decimal. However, if a wind farm is to be installed, the wind speed, which is a variable in the range of 0-20 m / s, can easily be estimated with round values. If the wind speed values obtained with round values are forecasted with a high accuracy rate, the wind speed that is necessary for the establishment of a wind power plant in a region is obtained by a shorter and easier way. In this study, the decision tree method was used in order to reach wind speed information with an easier method and with a very short training period. Decision tree methods were examined in three different structures and three different decision tree models were designed. Additionally the estimation results of all three methods were very high, the most accurate estimation was obtained by the "Coarse Decision Tree" method which is much simpler and faster than the others.

Key words: *Wind speed, Coarse, Fine , Medium, Decision Tree, Forecasting*

1. Introduction

Decision tree method is an effective method used to solve classification problems. As can be seen from many publications in the literature, the decision tree method has so far only been used for the classification of two-variable data [1]. In other words, usually the respond have two values, such as 1 and 0. Therefore, decision tree method is not generally preferred for the purpose of predicting any parameters in renewable energy sources. However, if the output variable in the data set is divided into classes, the decision tree method can be used to estimate and classify different parameters such as power quality in the field of renewable energy [2]. Because wind speed values in renewable energy sources can not be classified as too many varieties. However, in some studies, decision tree method has been used for wind speed classification [3]. Evaluation of wind sources and approvals to be taken for a wind farm are usually the longest activities in the development of the wind energy project. These can take up to 4 years for a large wind farm, which requires extensive environmental impact research. The installation of the wind farm can normally be completed roughly within a year. Precise determination of

¹ Kayseri University, Mustafa Çıkrıkçıoğlu Vocational Collage, Turkey, (nogay@erciyes.edu.tr) 

² Department of Electrical Engineering, Istanbul Technical University, Turkey, (akincitc@itu.edu.tr) 

the wind source at a given site is the biggest and first step in realizing a wind energy project. Because the wind source can significantly affect the cost of the wind farm. It is recommended that wind speed measurement be carried out for at least one year before the feasibility studies required to establish a wind farm in a field [4]. It is a controversial issue whether the estimation of the wind velocity with its the decimal expression is required. However, the estimation of round wind velocity values with a high accuracy rate may be sufficient to decide on the establishment of the wind farm [4]. If the wind speed can be estimated in a fast and simple way, rather than simply high accuracy, then the fastest and simplest method can be preferred over other machine learning methods. In this study, wind speed estimation was performed by decision tree methods. Estimation was made by three decision tree approach. The estimation results of these three models were compared with each other and the fastest and most attractive method with the highest accuracy rate was tried to be found.

After the introduction in the first part of the study, in the second part, the theoretical framework of the study is briefly explained. In this section, the structure and approach methods of decision trees are given.

In the third part of the study, the preferred method for performing the study was introduced. The stages of the study are explained.

In the results section, numerical results and graphs obtained from the study are given.

In the last section, evaluation of the results is given. It is discussed which method is more advantageous than others and how the results can be evaluated from the obtained graphs.

2. Theoretical Framework

Decision Trees (DT) are a classification and pattern recognition algorithm that has been widely used in literature in recent years. The most important reason for the widespread use of this method is that the rules used to create DT structures are understandable and simple. A multi-step or sequential approach is used in performing the DT classification process. Although other methodologies such as neural networks can be used for classification, decision trees provide an advantage for decision makers in terms of easy interpretation and intelligibility [5]. DT have some advantages compared to other classification methods. Some of these include low cost, easy-to-understand convenience, and compatibility with databases. Because of these advantages, it is widely used in many classification problems. Classification in decision trees is carried out in two steps: learning and classifying. In the learning step, the model is designed with an edited training data. The trained DT model is defined as classification rules or decision tree. In the classification step, test data is used to determine the accuracy of the classification rules or DT. If high accuracy is obtained in the test result, the rules are used to classify new data. It should be determined which fields in the training data should be used to form the tree in which order [6, 7].

The basic structure of a DT consists of three basic parts called nodes, branches and leaves. In this tree structure, each attribute is represented by a node. Branches and leaves are other elements of the DT structure. The last part of the DT is called a leaf and the top part is called a root. Portions between roots and leaves are expressed as branches [7, 8]. In other words, a tree structure consists of a root node containing data, internal nodes (branches), and end nodes (leaves). By using the attribute information of the training data, the basic principle in establishing a DT structure can be expressed as a series of questions about the data and concluding in the shortest time by acting on the answers obtained. In this way, the DT collects the answers to the questions and creates decision rules. The root node, which is the

first node of the tree, begins to be asked questions for the classification of the data and the formation of the tree structure. This process continues until leaves or nodes without branches are found. The test data is used to determine the generalization capability of the generated tree for a new data set. A test data that is new to the tree structure created by the training data enters the root of the tree. This new data tested in the root is sent to a lower node according to the test result. This process is continued until it reaches a specific leaf of the tree. There is only one way or a single decision rule from root to every leaf. Figure 1 shows a simple (coarse type) tree structure consisting of four-dimensional attribute values of four classes. The tree structure in Figure 1 is the DT of the coarse type algorithm designed in this study. In Figure 1, the “VarNameA” attribute values; VarNameA <a, b, c, d and e values are the threshold values for branching. 1, 2, 3 and 4 show the class labels. Depending on the number of variables used in each stage of tree formation, there are single variable or multivariate decision tree structures [9-11].

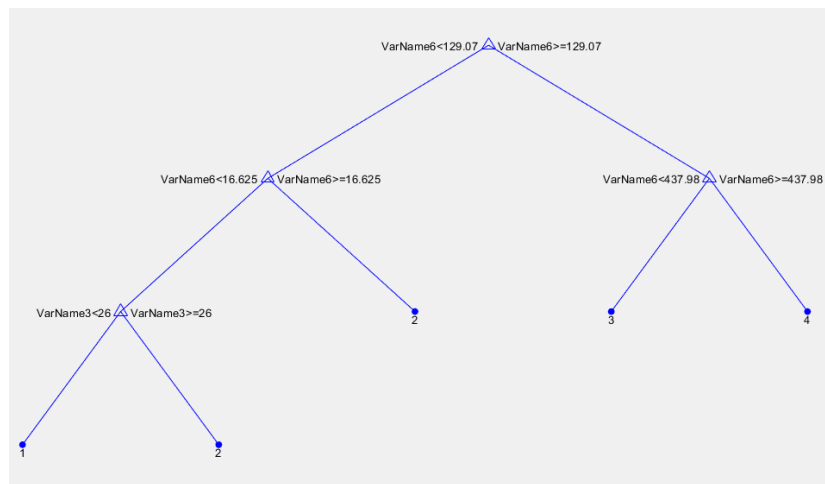


Figure 1. Coarse DT

By testing a single attribute in each internal node of the univariate decision tree, the data are divided into two or more subgroups. In this way, division continues until the decision tree repeatedly reaches a leaf node of the input data. The specific values of the decision limits in an univariate decision tree are experimentally estimated from the training data. In the case of persistent data, the $x_i > c$ shaped logical test is carried out, where x_i shows a characteristic in the data space of each internal node at the internal node, and that ‘ c ’ is a threshold value in the observed range of x_i . The threshold value ‘ c ’ can be determined using certain conditions, such as maximizing differences or minimizing similarity in descent nodes [12-14]. The most important step in the creation of decision trees is to determine the criteria for tree branching. There are various approaches developed to solve this problem. The most important of these are the ‘information gain’ and ‘information gain ratio’, the ‘gini-index’, the ‘towing rule’, and the ‘square probability table statistic’ approaches. ID3, C4.5, C5.0, CART, CHAID and QUEST algorithms are examples of algorithms using these approaches. According to the method of information gain, ‘information theory’ which includes ‘entropy rules’ is used in order to determine which according to characteristic to make branches in decision tree. Entropy is a measure of irregularity or uncertainty in a system. In single variable decision trees, ID3 algorithm uses informagion gain approach. The C4.5 algorithm, which is an improved version of this algorithm, uses the gain ratio approach calculated by taking advantage of the information gain. Gini Index approach was used in this study. All

variables are assumed to be continuous according to the Gini Index. It is assumed that there are many possible distinctions for each variable [14].

If a T data set contains ' N ' samples from ' n ' different classes, the gini index, $gini(T)$ is calculated as follows:

$$gini(T) = 1 - \sum_{j=1}^n p_j^2 \quad (1)$$

p_j denotes the relative frequency of the class j in T .

If the T data set is divided into two N_1 and N_2 magnitudes as T_1 and T_2 respectively, the gini index for the allocated data is:

$$gini_d(T) = \frac{N_1}{N} gini(T_1) + \frac{N_2}{N} gini(T_2) \quad (2)$$

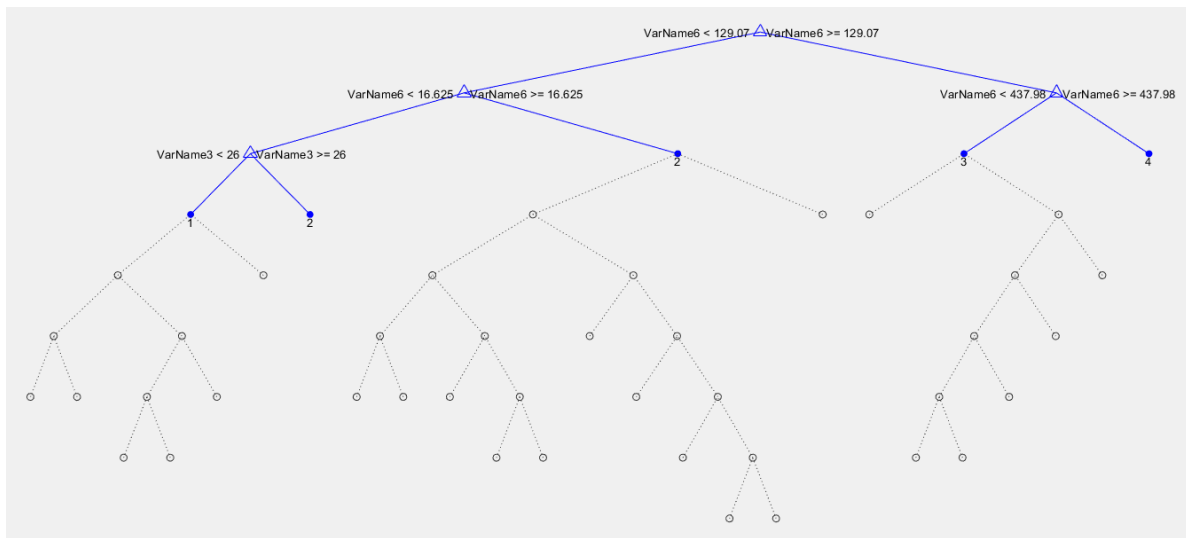


Figure 2. Fine decision tree model

The variable with the lowest gini value is selected. Another important point in the DT formation is the pruning of the tree structure. The DT classifier divides the training data into subsets that contain only one class, resulting in a very large and complex tree structure. Therefore, it may be possible to place a leaf in the decision tree instead of a sub-tree. In this way, the processing decision tree is called pruning [15-19]. With pruning, the parts of the decision tree which do not affect the accuracy of the classification are removed. Thus, a less complex and more understandable tree is obtained. Two methods are generally used to simplify the tree structure and reduce the process complexity by pruning. The first one is the pruning method which is decided to be reduced while the tree structure is formed, and the other is the last pruning method where the pruning is made after the tree structure is formed. If the pruning of the sub-tree with a single leaf or the most used branch of this tree will reduce the expected error rate, the tree is truncated. As the error rate in the sub-branches is reduced, the error rate for the whole tree will decrease. At the end of the pruning process, a tree with a minimum error rate is obtained. 2 shows a sample that can be prone to pruning in the *fine* type decision tree used in this study [16 – 19].

3. Methodology

The study was performed using Classification Toolbox in MATLAB environment. In this environment, decision trees are given as three separate structures. The first building is the most complex 'Fine' decision trees among the three. The second is 'Medium' and the third is the 'Coarse' decision tree structure. In this study, these three each of DT structures were designed to estimate wind speed. The Gini index was selected for all three decision trees. The data set was obtained and arranged before the decision tree models were created. Table 1 shows a summary of the data set used for each of the three models. Table 1 also shows the definitions of variables. The first 6 variables are "Predictor" and the last variable is "Respond". "Respond" in the data set shows the wind speed for 50 meter high. The data set, used for this study was obtained from "Turkish State Meteorological Service in 2014". The data set consists of meteorological data for Turkey Amasra district.

Table 1. Summary of the data set

| Data | Predictors | | | | | | Respond |
|----------------------------|--------------------------------|--------------------------------|---|-----------------------------------|--------------------------------------|---|---------------------------------|
| Variable Label | VarName1 | VarName2 | VarName3 | VarName4 | VarName5 | VarName6 | VarName7 |
| Variable Definition | Daily average temperature (C°) | Daily average temperature (K°) | Daily average soil temperature 20 cm (C°) | Daily local relative humidity (%) | Ro, Air density (kg/m ³) | P/A, Wind power intensity (W/m ²) | Daily average wind speed, (m/s) |
| Min | -1.11 | 272.04 | 4.45 | 37 | 1.16 | 0.19 | 0.49 |
| Max | 29.40 | 302.55 | 27.6 | 96 | 1.29 | 10308.76 | 18.49 |

Since the DT method is a classification method, it is necessary to enumerate the wind speed data by classifying them in order to use this method for estimation purposes. Table 2 shows the numbering of the actual respond of the data set. In other words, the wind speed data representing the output of the model is divided into four parts and a new output is obtained.

Table 2 Numbering of respond

| Win Speed 50 m (m/s) | Numbering |
|----------------------|-----------|
| 0_3 | 1 |
| 3_6 | 2 |
| 6_9 | 3 |
| 9 => | 4 |

In the study, three separate decision tree models were designed. The first model is the Coarse decision tree model with a very simple structure. Figure 1 shows the structure of this model. The second model is the Fine decision tree model. The Fine decision tree model shown in Fig.2 is 7-dimensional. Figure 3 shows the branches on the left side of the Fine decision tree created. At each node, the variables are given with their threshold values, whether they are large or small. The numbers in the last sections of each branch represent the wind speed.

Figure 4 shows the branches, nodes, and leaves in the middle of the Fine decision tree. In Figure 4, the thresholds at each node are compared with the corresponding variables. Figure 5 shows the right-hand branch and threshold values of the Fine DT. The third DT model designed in the study is less complicated than the Fine DT. Figure 6 shows the third model that is the Medium decision tree model.

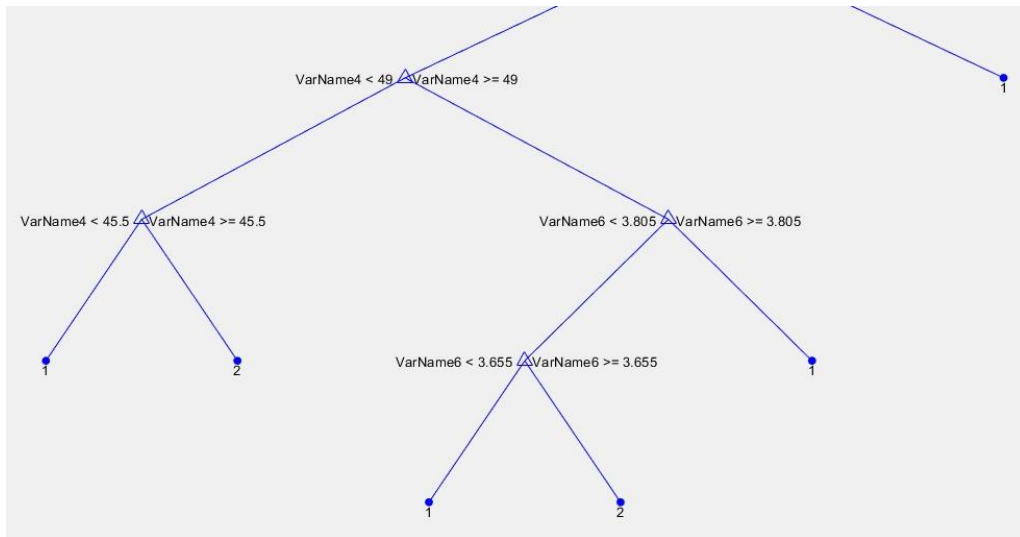


Figure 3. Left side of fine decision tree

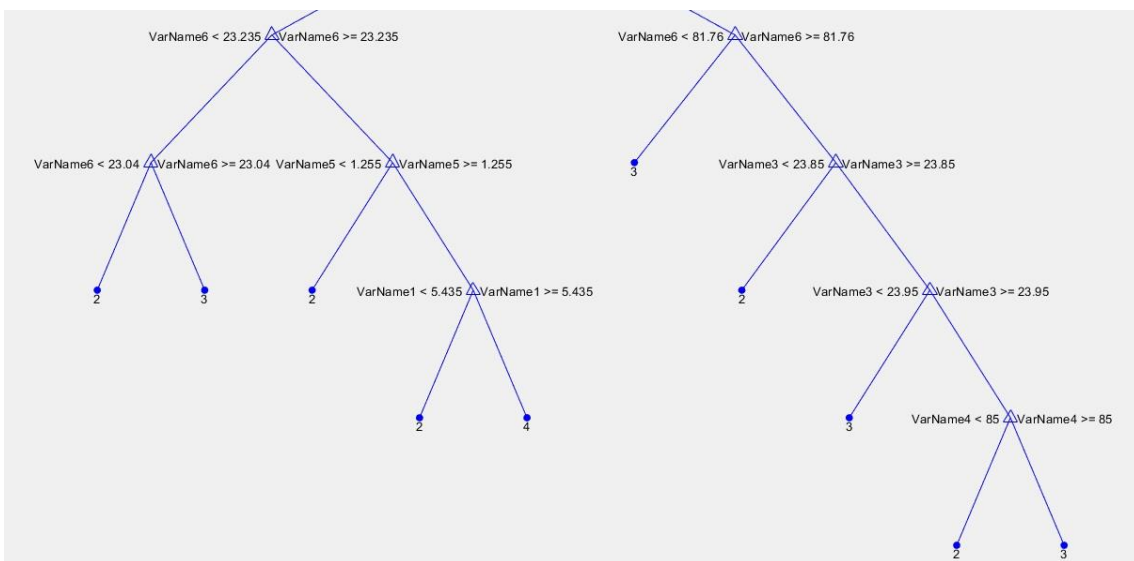


Figure 4. Middle part of decision tree

As can be seen from Figure 6, although Medium DT consists of fewer branches than Fine DT, it has the same number of exit points and answers. Also in Figure 7, middle part of Medium DT is illustrated.

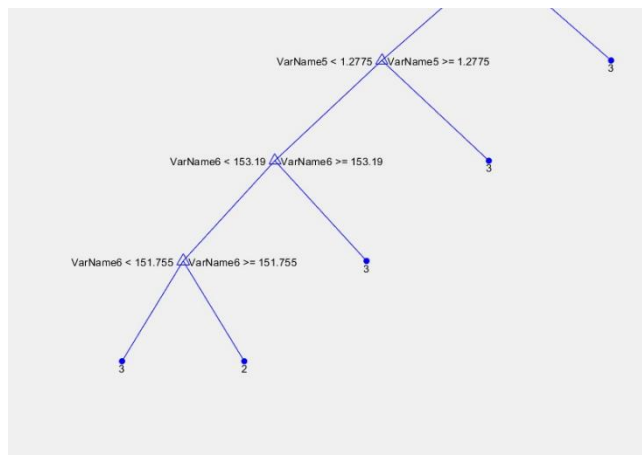


Figure 5. Right side of fine decision tree

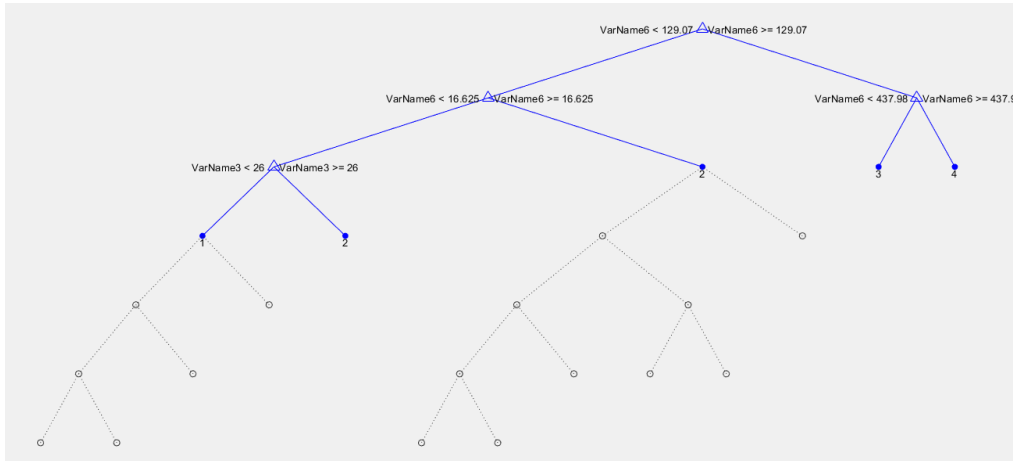


Fig.6 Medium decision tree

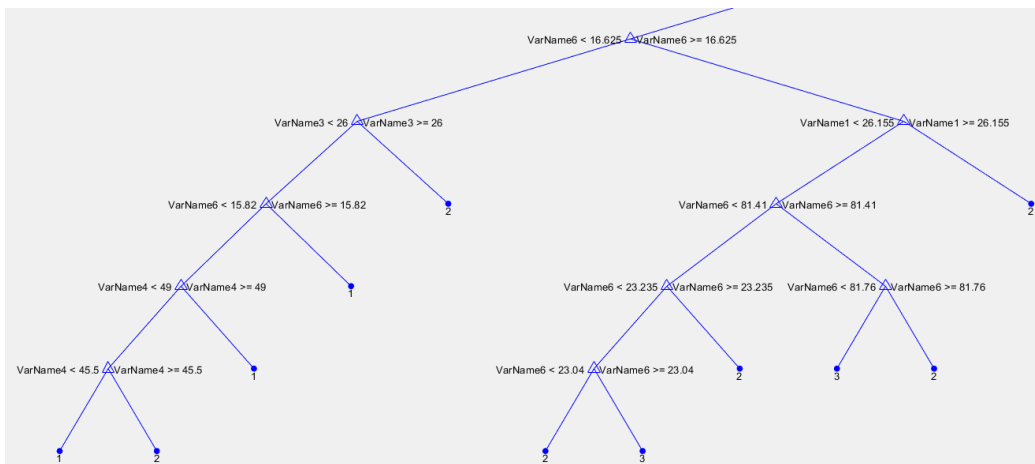


Figure 7. Middle part of medium decision tree

4. Results

Table 3 shows the results obtained from the study. Estimates were obtained at high accuracy rates in all three decision tree methods.

Table 3 The results of applications

| | Accuracy (%) | Prediction speed (obs/sec) | Training time (sec) | Maximum number of split |
|------------------|--------------|----------------------------|---------------------|-------------------------|
| Fine DT | 95.6 | 1400 | 0.93103 | 100 |
| Medium DT | 95.9 | 8200 | 2.0152 | 20 |
| Coarse DT | 96.7 | 39000 | 0.52248 | 4 |

Figure 8 shows how two variables affect output. The Scatter plot is only available between VarName6 and VarName1. Figure 9 shows the ROC curves obtained for all three decision tree models

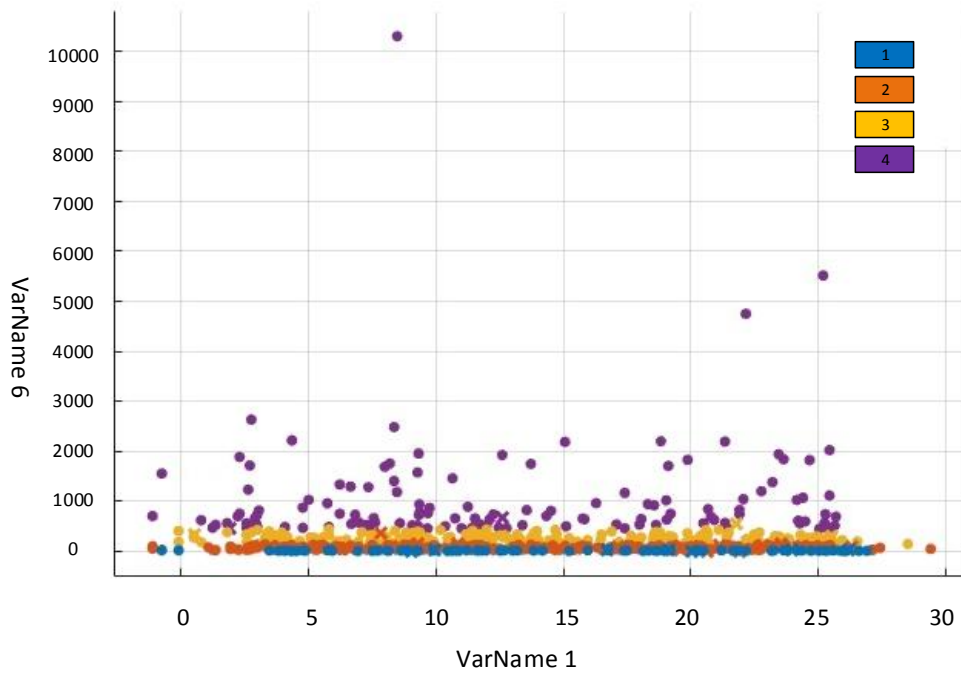


Figure 8. Scatter plot for fine tree

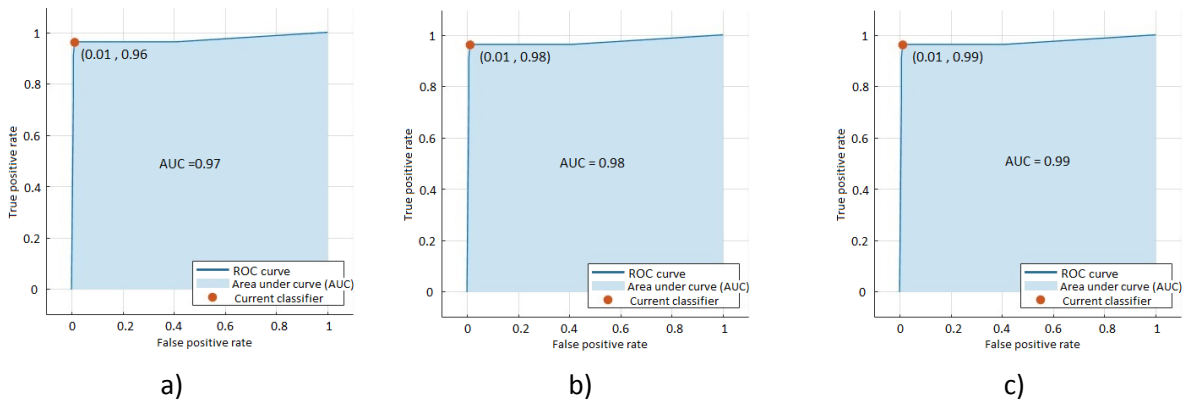


Figure 9. ROC curves of a) Fine DT, b) Medium DT, c) Coarse DT

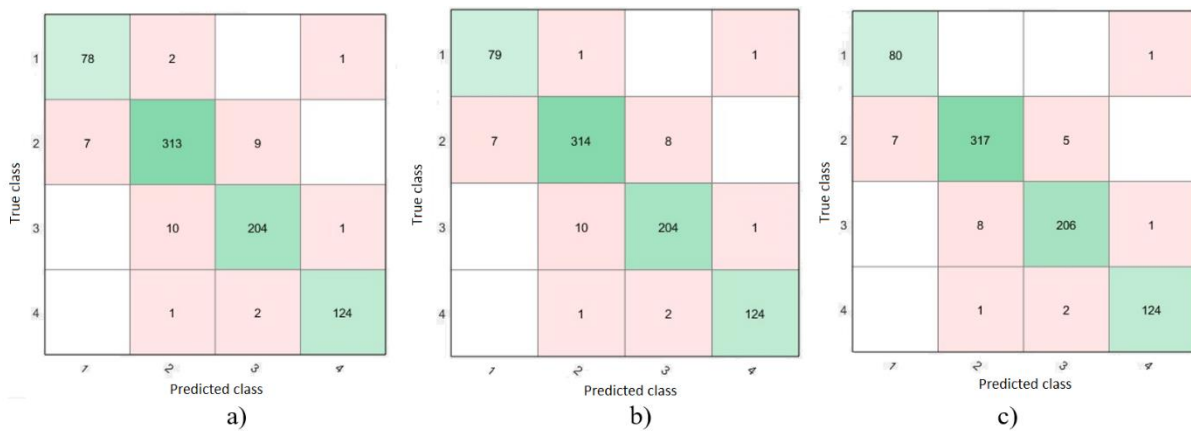


Figure 10. Confusion matrices of a) Fine DT, b) Medium DT, c) Coarse DT

Figure 10 shows the confusion matrices obtained according to the estimation results of all three models. With this confusion matrix, it is also possible to understand the reason for each prediction and which output is correct or incorrect for which output.

5. Conclusions

The following results can be obtained from the study.

1. From Table 3, it can be observed that the Coarse Tree has reached the highest accuracy rate. Coarse tree is the simplest decision tree method. Therefore, as can be seen from Table 3, it has a higher estimation rate than other methods. At the same time, the duration of training is shorter than the duration of the other methods. In the Coarse decision tree method, the maximum number of splits is considerably less than the others, depending on the fact that the tree is not complex.
2. According to the ROC curves in Figure 9, the AUC (Area Under the Curve) values of medium and coarse decision trees are equal to each other and are higher than the Fine decision trees. As can be seen from the ROC curves, all three decision trees are successful in the forecastings. In addition, the simplest and most understandable Coarse DT method can be said to be more successful and acceptable.
3. According to the confusion matrices in Figure 10, if the diagonal figures of the 4x4 matrix (green ones) are examined and the values of the confusion matrix belonging to each decision tree method are compared to each other, the superiority of the coars can be noticed. Diagonal numbers indicate the number of accurately predicted data. It is obvious that the maximum number is in Coars. Figures in other regions indicate incorrect estimates.
4. As a result, the decision trees method produces satisfactory estimates by replacing the artificial neural networks when the correct numbering and correct calculation option and the correct decision tree method are used. These estimates, however, are predetermined rounded output values, as indicated above. It is understood from this study that it is possible to find wind speed estimations needed for any region with decision tree close to reality.

References

- [1] Gupta, B., Rawat, A., Jain, J., Arora, A., Dhami, N. (2017). Analysis of Various Decision Tree Algorithms for Classification in Data Mining. *International Journal of Computer Applications*, 163(8), 15-19.
- [2] Ray, P.K., Kishor, N. (2014). Optimal Feature and Decision Tree-Based Classification of Power Quality Disturbances in Distributed Generation Systems. *IEEE Transactions on Sustainable on Energy*, 5(1), 200-208.
- [3] Sangita B.P., Deshmukh, S.R. (2011). Use of Support Vector Machine, decision tree and Naive Bayesian techniques for wind speed classification. *International Conference on Power and Energy Systems Power and Energy Systems (ICPS)*.
- [4] Retscreen Engineering & Cases Textbook, Clean Energy Project Analysis, Clean Energy Decision Support Centre ISBN: 0-662-35670-5 Catalogue no.: M39-97/2003E-PDF, © Minister of Natural

Resources Canada 2001 - 2004.

http://unfccc.int/resource/cd_roms/na1/mitigation/Module_5/Module_5_1/b_tools/RETScreen/Manuals/Wind.pdf, last access date: Feb 27th, 2019

- [5] Chien, C. F., Chen, L. F. 2008. Data Mining to Improve Personnel Selection and Enhance Human Capital: A Case Study in High-Technology Industry. *Expert Systems with Applications*, 34, 280-290.
- [6] Tsang, S., Kao, B., Yip, K.Y., Ho, W.S., Lee, S.D. (2011). Decision Trees for Uncertain Data, *IEEE Transaction on Knowledge and Data Engineering*, 23(1), 67-78.
- [7] Rokach, L., Maimon, O. (2014). *Data Mining with Decision Trees Theory and Applications*. 2nd edition, 81, World Scientific Publishing Co. Pte. Ltd.
- [8] Quinlan J.R, (1993). *C4.5: Programs for Machine Learning*. Morgan Kaufmann, San Mateo, CA, 302.
- [9] Dougherty, G., *Pattern Recognition and Classification*. Springer New York Heidelberg Dordrecht London.
- [10] Loh, W.Y., Shih, Y.S. (1997). Split Selection Methods for Classification Trees, *Statistica Sinica*, 7(4), 815-840.
- [11] Friedl, M.A., Brodley C.E., (1997). *Decision tree classification of land cover from remotely sensed data*. *Remote Sensing of Environment*, 61, 399–409
- [12] Safavian S.R., Landgrebe D. (1991). A survey of decision tree classifier methodology. *IEEE Transactions on Systems Man and Cybernetics*, 21, 660-674
- [13] Tan, P.N., Steinbach, M., Kumar, V. (2006). *Introduction to Data Mining*. Pearson Addison-Wesley.
- [14] Maimon, O., Rokach, L. (2010). *Data Mining and Knowledge Discovery Handbook*, Springer 2010.
- [15] Suneetha, N., Hari, Ch.V.M.V., Kumar, S. (2010). *Modified Gini Index Classification: A Case Study of Heart Disease Dataset*. *International Journal on Computer Science and Engineering*, 2(6),1959-1965
- [16] Breiman L., Friedman J.H., Olshen R.A. and Stone C.J. (1984). *Classification and Regression Trees*. Monterey, CA: Wadsworth, 358 s.
- [17] Raileanu L.E., Stoffel, K., *Theoretical Comparison between the Gini Index and Information Gain Criteria*. *Annals of Mathematics and Artificial Intelligence*, 41(1):77-93.
- [18] Teknomo, K. (2012). *Decision Tree Tutorial*. [www. revoledu.com](http://www.revoledu.com) Online edition.
- [19] Mingers J., (1989). *An empirical comparison of pruning methods for decision tree induction*. *Machine Learning*, 4, 227–243.

THE EFFECT OF GRAPHENE OXIDE ON THE STRUCTURAL AND ELECTRICAL PROPERTIES OF YTTRIUM FERRITE BASED NANOPOWDERS

Handan AYDIN


In this study, Yttrium Ferrite based nano electroceramics were prepared by the doping at various ratios of graphene oxide by the hydrothermal method. The obtained doped and undoped samples were characterized by XRD, SEM, FTIR, DTA, UV-VIS-NIR spectroscopy, temperature dependent electrical resistance changes and dielectric measurements. From the XRD results, it is observed that the obtained samples are polycrystalline with an Orthorhombic structure. The crystal parameters are changed with the doping of graphene oxide. FTIR spectra indicate that the graphene oxide changes the peak intensities. This confirms the incorporation of the graphene oxide into the ceramic structure. The doping of the graphene oxide changes the optical band gaps of the samples. The dielectric constants of the samples are changed with the graphene oxide. The DC electrical conductivity measurements confirm the semiconducting behavior of the samples. The obtained results indicate that the electronic and nanostructure of the synthesized electroceramics can be controlled by the doping of graphene oxide for electronic and energy applications.

Keywords: Hydrothermal method, Graphene oxide, Hummers method, Nano electroceramic, structural properties.

1. Introduction

Over the last years, research on the nano-structured electroceramics has been increasing. These materials have played an important role in advanced technology applications [1] such microwave industries [2], electronics [2], data storage devices [2, 3], gas-sensitive sensors [4], digital disk recording[2] and actuator applications [2]. Efforts have been made for the improving of specific properties and potential applications [5] of nano electroceramics ABO_3 type (where A is a rare or alkaline earth metal and B is a first-row transition metal) [6, 7]. The materials in this formula are often referred to as rare earth orthoferrites [8]. Orthoferrites have attracted attention due to their a wide range of Ferro-, piezo-, pyroelectrical properties and electro-optical effects[7]. Yttrium ferrite ($YFeO_3$) is a member of this class. It has perovskite structure with an orthorhombic unit cell [5, 8, 9] and a p-type semiconductor ($E_g=2.58$ eV) [4].

Recently, the studies on the structural and electrical properties of yttrium ferrite are increasing. In this context, the scientists have investigated and concentrated zoom in on improving the properties of Yttrium Ferrite with a different dopant and various element.

Handan AYDIN, Department of Metallurgy and Materials Engineering, Engineering Faculty, University of Munzur, Tunceli, TR, (handanaydin23@gmail.com)  <https://orcid.org/0000-0002-0141-9773>

Received: 22 May 2019; Accepted: 25 June 2019

Doi: <https://doi.org/10.36222/ejt.569114>

In recent years, to produce these materials have been used different synthesis process such as solvothermal [2], sol-gel [2, 5, 6, 8-11], , hydrothermal method [6, 8, 9], coprecipitation [8, 9], solid state reaction method [5, 6, 9, 10], self-propagating combustion synthesis [5], alkoxide method [5, 10], , pulsed laser deposition [5, 10], microwave-assisted [5, 9, 10], sonochemical synthesis [2, 5, 10]. Among these production methods, hydrothermal synthesis can be preferred due to its advantages such low temperature, control of particle size, without any calcination or milling step and not purity phase [12]. In this scientific study, pure and Graphene oxide doped Yttrium Ferrite nano electro-ceramics were synthesized by the Hydrothermal Process. The structural, morphological, chemical and physical electrical properties of the obtained samples were investigated.

2. Experimental Details

2.1. Synthesis of Graphene Oxide

Graphene oxide was prepared by a modified Hummers method. In this method, 1 g graphite powder, 0.5 g sodium nitrate and 23 ml sulfuric acid were mixed into a beaker and exposed stirring for 30 min in an ice bath. Then 3 g potassium permanganate was slowly added to mixture solution by magnetic stirring through 6 hours. Subsequently, after the solution was kept in the ultrasonic machine for 2 hours and 100 ml distilled water and 2ml H₂O₂ (30%) were added by using a magnetic stirrer. Finally, the solution was washed with de-ionized water and filtered until pH value reached to 7.

2.2. Synthesis of YFeO₃ via Hydrothermal Method

Synthesis of YFeO₃ nano electroceramics were carried out by hydrothermal route. The precursor solution was prepared using Yttrium (III) nitrate hexahydrate (N₃O₉Y) (Abcr, %99,9), Iron (III) Chloride Hexahydrate (FeCl₃.6H₂O) (Merck, %99) and potassium hydroxide (KOH) (Merck, %85) as mineralizer and de-ionized water as a reaction medium. For the production process of the samples, the schematic diagram about with Hydrothermal method is given in Fig. 1. In this reaction procedure, four solutions containing N₃O₉Y, 5.5 mmol FeCl₃.6H₂O, and 9 mol KOH were prepared. 6.1 mmol of N₃O₉Y was added into 55mL of de-ionized water with constant magnetic stirring followed by the addition of 6.1 mmol of FeCl₃.6H₂O. The solutions were stirred at room temperature for 1 h to obtain a homogeneous solution. Thereafter, KOH was slowly added to the above Y-Fe solution to co-precipitate. The solution was kept at room temperature °C for 2 h under stirring. After, each graphene oxide solution was added to the precursor solution. The final mixture is here after called LFO, LFO20, LFO50 and LFO100, respectively. The suspension solution was poured into full-automatically hydrothermal system (Fytronix HT-100) for the hydrothermal process. The process was carried out for 6 h at temperature of 200 °C. After completion of the hydrothermal reaction, the autoclave was cooled naturally to the room temperature. The products were filtered and dried at room temperature for 24 h. The obtained powders were formed by hydraulic press machine under a uniaxial pressure of 10 MPa at room temperature.

2.3. Characterization of Samples

The crystalline phase of the products was recognized using a BRUKER ADVANCE D8 X-ray diffractometer with Cu K α radiation ($\lambda = 1.5406 \text{ \AA}$) in the 2 θ range from 20 to 80° with 0.02 °/min. at room temperature. The morphology of nano electro-ceramics were investigated with the a High-Resolution Scanning electron microscope (JEOL JSM-7001F). High-Resolution Transmission electron microscope (JEOL JEM-2100F) was performed at an accelerating voltage of 200 kV, by placing the powder on a copper grid to observe the microstructure of the powders. The optical spectrum was recorded by a SHIMADZU 3600 UV-VIS-NIR spectrophotometer in the wavelength range of 200–1400

nm at room temperature. The thermal analysis of the powders were determined by SHIMADZU DTG-60AH from room temperature to 900 °C in Argon ambient at a scan rate of 10 °C/min. FTIR spectra studies were made with Thermo Scientific Nicolet IS5 mark Fourier transform infrared spectrometer with an ID5 ATR sample holder in the wavenumber range from 400 to 4000 cm⁻¹. The dielectric and alternating current conductivity properties were investigated using a HIOKI 3532-50 LCR HITESTER at room temperature. The ferroelectric properties were studied using Radiant Precision Premier II Technology. The electrical conductivity of the samples was measured as a function of temperature using a KEITHLEY 6517A electrometer.

3. Results and Discussion

3.1. Structural and morphological characterization of Produced Nano Electroceramics

The XRD patterns of pure and GO doped YFeO₃ nanostructure powder samples are shown in Fig.1. The observed all peaks in Fig.1. revealed that YFeO₃ are polycrystalline structure with the orthorhombic structure. The crystalline phases were identified by reference to the Joint Committee on Powder Diffraction Standards (JCPDS 01-073-1345) files. XRD pattern of the samples were appeared at 2θ values, 33.462°, 35.956° and 54.361° corresponding to (200), (120) and (310) reflections, respectively. As seen in the XRD peaks, the intensity of peaks is changed with increasing Graphene oxide doping. This indicates that Graphene oxide is incorporated into sites of YFeO₃.

The lattice parameters (a, b and c) of the orthorhombic perovskite structure of YFeO₃ at various graphene oxide contain were determined according to the following relations [6, 13,30]:

$$\frac{1}{d_{hkl}^2} = \frac{h^2}{a^2} + \frac{k^2}{b^2} + \frac{l^2}{c^2} \quad (1)$$

Where (h, k, l) are the indices of every peak of crystallographic plane obtained from XRD patterns. d is the interplanar distance, (a, b, c) are the lattice constants. Average crystallite sizes were estimated using the Debye-Scherrer equation [1, 14-19,31]:

$$D = \frac{0.9 \lambda}{\beta \cdot \cos \theta} \quad (2)$$

The crystallite parameters of the unit cells of the samples are given in Table 1. As seen in Table 1, with the addition of graphene oxide, the crystallite size was changed for (200) crystal plane.

Table 1. The calculated values of the crystallite parameters of the unit cells of the samples.

| | 2 θ (°) | Crystal Structure | FWHM | Crystallite Size (nm) | d (nm) |
|---------------|---------|-------------------|-------|-----------------------|--------|
| YFO | 33,462 | Orthorhombic | 0,304 | 27,30 | 0,2675 |
| YFO20 | 33,484 | Orthorhombic | 0,330 | 25,15 | 0,2674 |
| YFO50 | 33,312 | Orthorhombic | 0,225 | 36,87 | 0,2687 |
| YFO100 | 33,352 | Orthorhombic | 0,209 | 39,69 | 0,2684 |

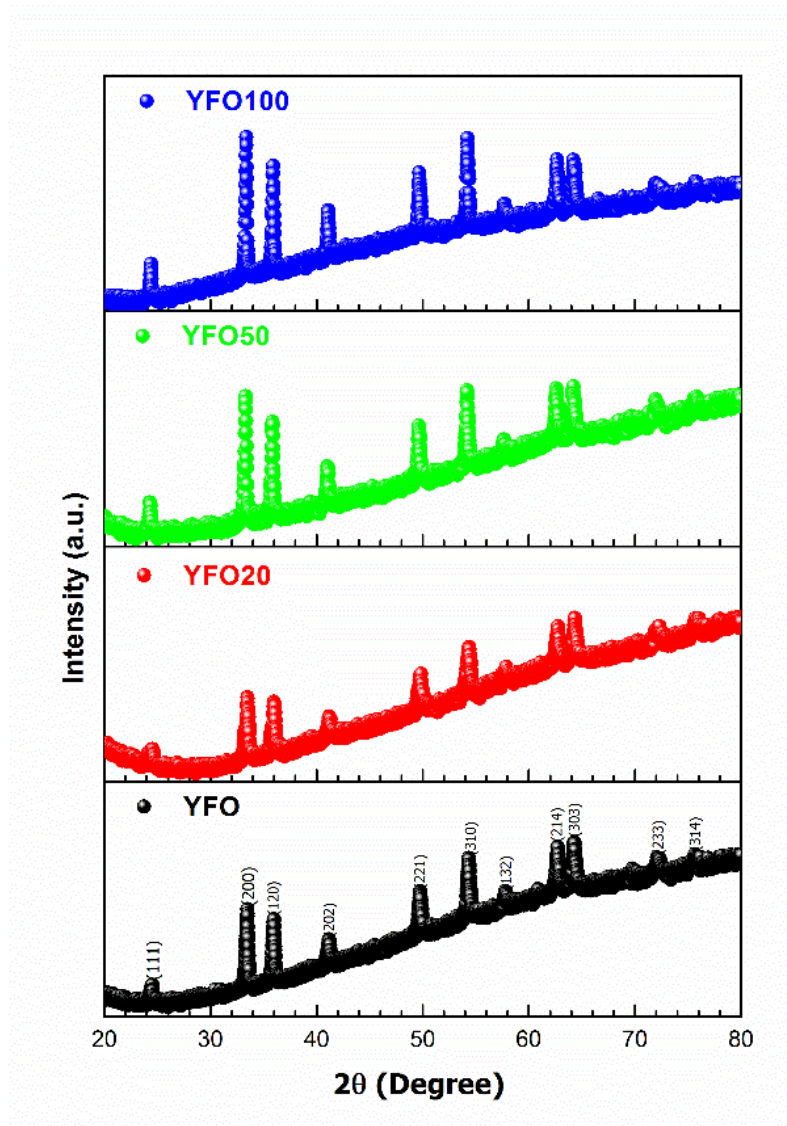


Figure 1. XRD spectrum of Samples

In order to determine the surface morphologies of undoped and graphene oxide-doped YFeO_3 samples prepared by using the hydrothermal method they were analyzed with Scanning Electron Microscope (SEM). Fig.2. shows SEM images of the prepared samples. When the SEM images in Fig.2. were examined, it was seen that the grains on the surface of the sample were large and small, were randomly oriented, and were not distributed homogeneously and there were partial accumulations formed by grain stacks. It could be clearly seen that the samples formed in composite structure made of nano-sized grains and there were morphological differences in surface structure. The surface structure of the samples was generally composed of grains with similar size and morphology. It was very obvious that the surface morphologies of the samples changed with the graphene oxide dopant [32]. The change of crystallite size and particle size with the amount of graphene oxide are portrayed in Fig.3.

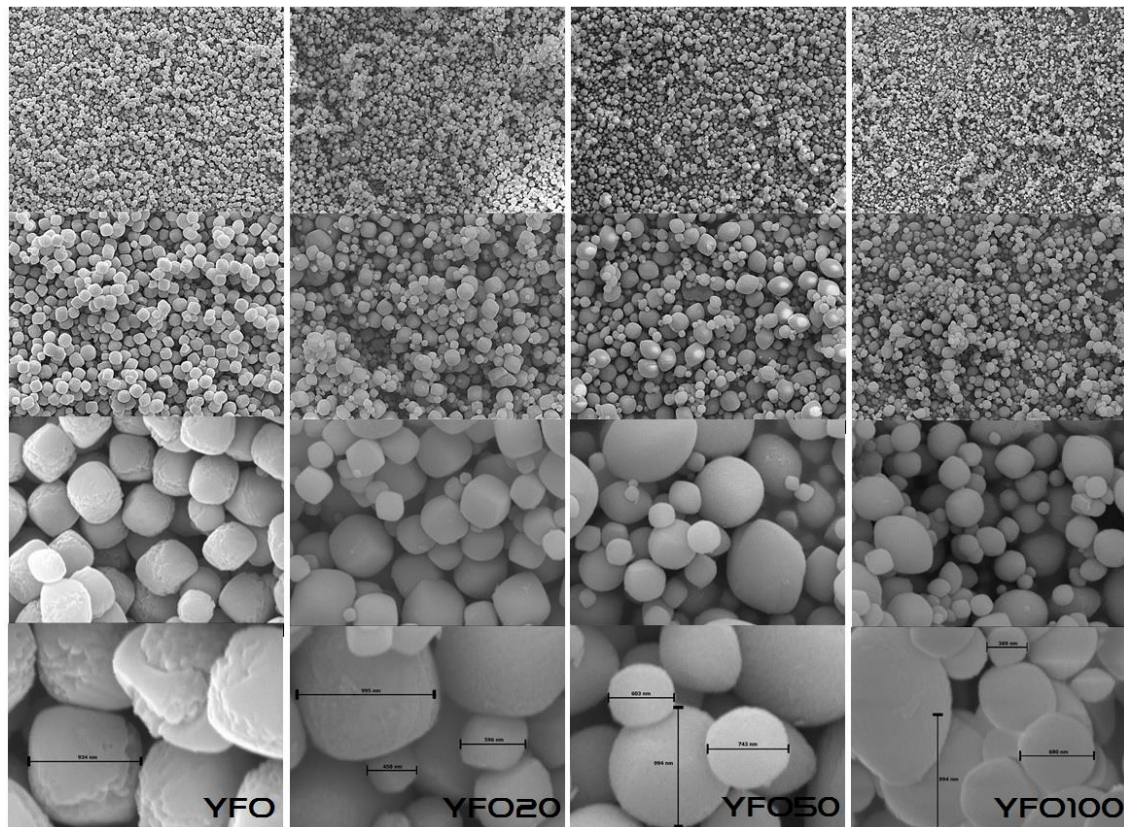


Figure 2. Scanning Electron Microscopy photographs of the Yttrium Ferrite nanopowders

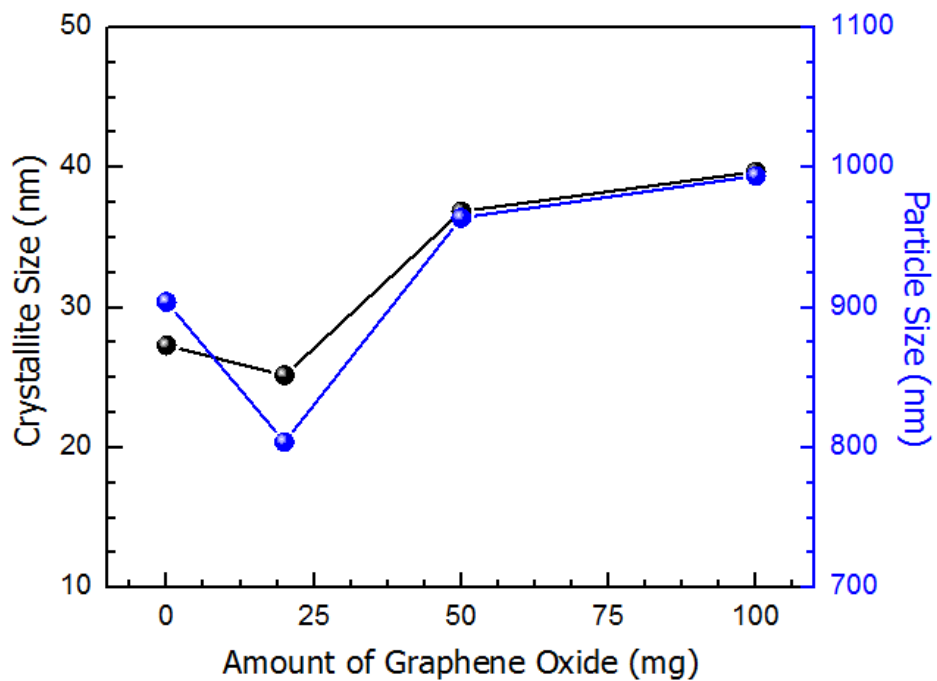


Figure 3. The change of crystallite size and particle size with the amount of graphene oxide

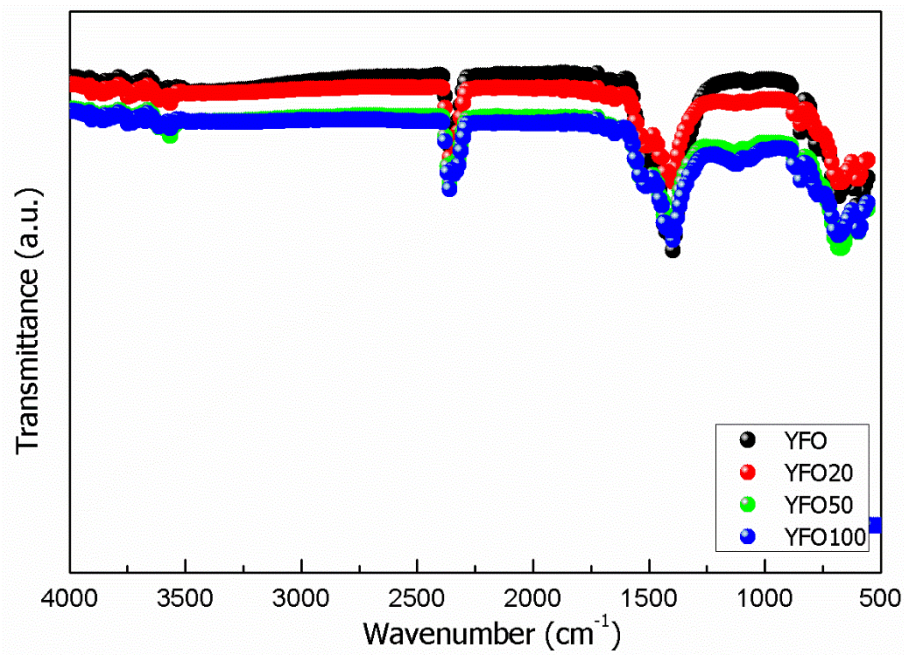


Figure 4 FT-IR spectra of synthesized yttrium ferrite nano powders

The FTIR spectra of the samples are shown in Fig. 4., and the as-detected bands can be explained as follows. The band detected at 1507 cm^{-1} is attributed to the bending mode of H_2O band. The characteristic band of CO_2 is detected at 2364 cm^{-1} . The band at 1397 cm^{-1} is due to the $\text{C}=\text{O}$ bond. The band observed at $1320\text{--}1360\text{ cm}^{-1}$ is related to the NO_3^- stress vibration mode. The band at 592 cm^{-1} is related to the bending vibration mode of $\text{Fe}-\text{O}$ bond.

Fig. 5. shows both DTA curves in the range from room temperature to $900\text{ }^\circ\text{C}$ for each sample. There are one exothermic peaks in the DTA thermograms of all the samples. At the temperatures below the this peak, the weight losses are due to the elimination of the adsorbed water from the samples.

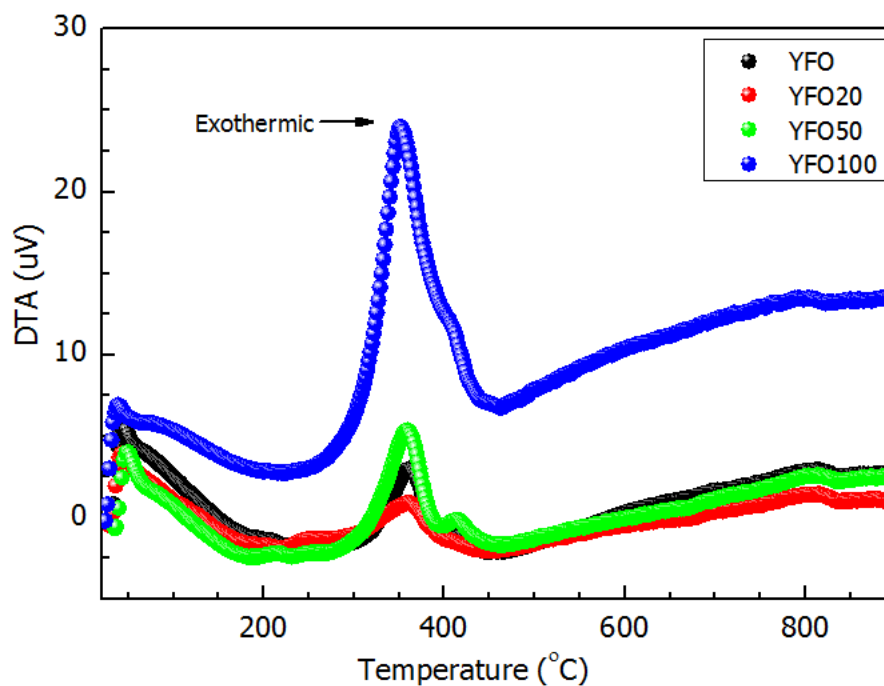


Figure 5. DTA curves for the nanopowders

For the peaks for each sample, these losses may be due to the elimination of some oxygen-containing functional groups. While the peak is detected at 358, 352, 355 and 348 °C for YFO, YFO20, YFO and YFO100, respectively. As can be easily seen from DTA thermograms, these peaks detected at the above-mentioned temperatures are due to the weight loss for each sample. These findings mean that the amount of the additive affects significantly the thermal stability of the GO.

3.2. Optical characterization

Reflection spectra of undoped and graphene oxide doped YFeO_3 samples are presented in Fig. 6. As shown in Fig. 6, the reflection curves of the samples show a rapid decrease in a wavelength of about 600 nm. This peak varies depending on graphene oxide adding. This confirms that the optical band gaps of the films change with graphene oxide doping. With graphene oxide doping, the reflectance values of the samples increase compared to the undoped YFeO_3 sample. The change in optical reflectance may be due to the morphological change in the samples because the aspect ratio of the crystallites varies depending on the sample surfaces. The results obtained confirm the results obtained in the SEM photographs. The sample with the highest reflectance value is the undoped YFO50 sample. Besides, the reflectance values decreased at shorter wavelengths. The reason for this may be the reflection of photons due to the decrease in their energy and thus less interaction with electrons, atoms, or crystal molecules.

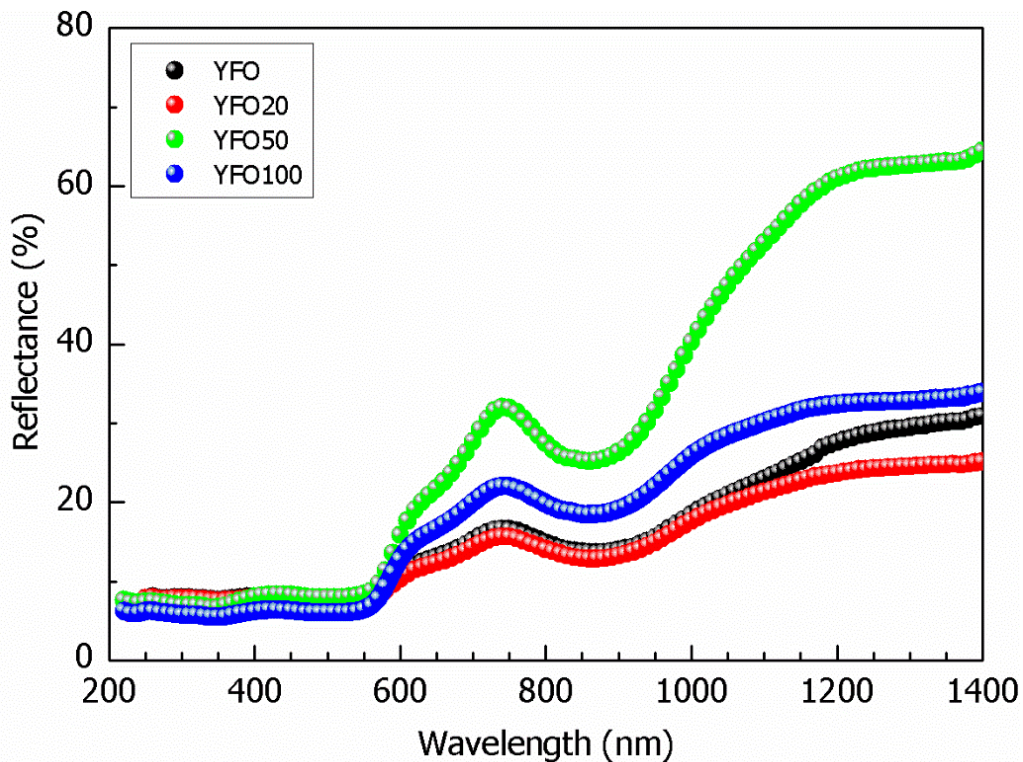


Figure 6. The reflectance spectra of samples as a function of wavelength

The optical band gap (E_g) had a direct effect on the optical properties of the semi-conductive samples. The diffuse reflectance spectra given in the Fig. 6. were used to determine the band gaps (E_g) of the undoped and graphene oxide doped YFeO_3 nano powders by using the Kubelka-Munk function. Kubelka-Munk function [18] can be defined as follows [1, 13, 16, 17, 19-24,33-35] :

$$\left(\frac{F(R)hv}{t}\right) = A \cdot (hv - E_g)^n \quad (3)$$

Where R is diffuse reflectance; $F(R)$ is Kubelka-Munk function corresponding to the absorption value; t is the thickness of the sample; A is an energy-independent constant, hv is photon energy, and E_g is band gap and n is $\frac{1}{2}$ for direct transitions.

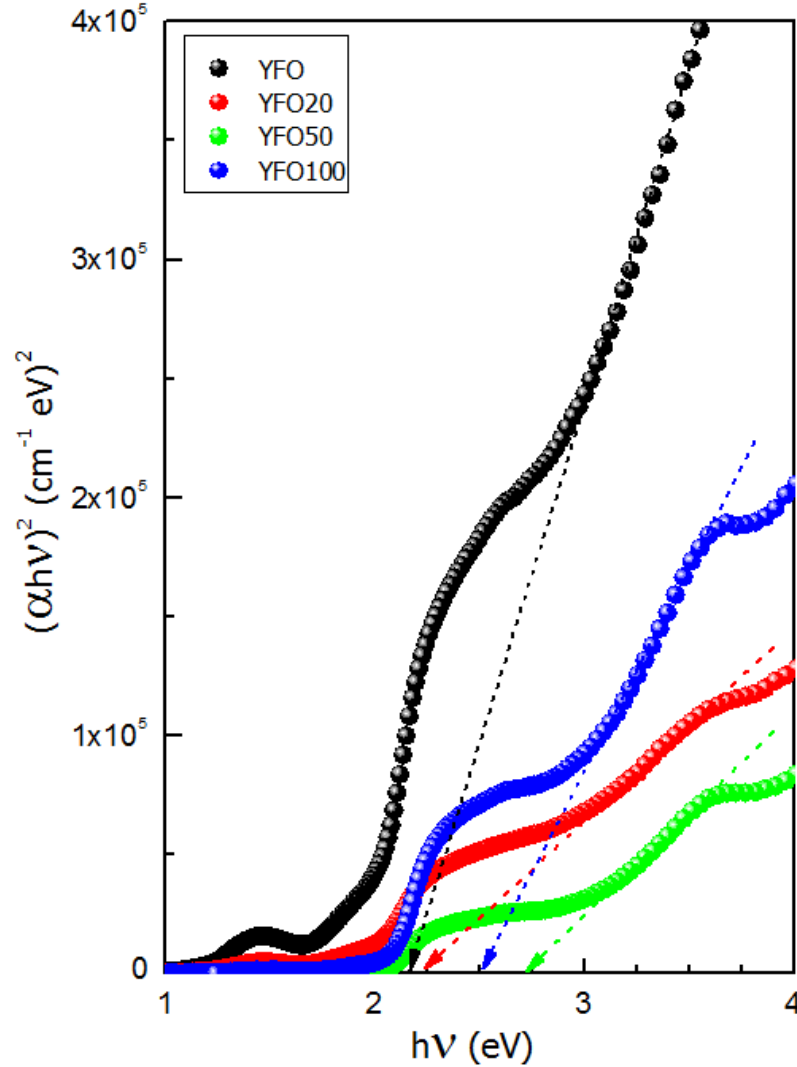
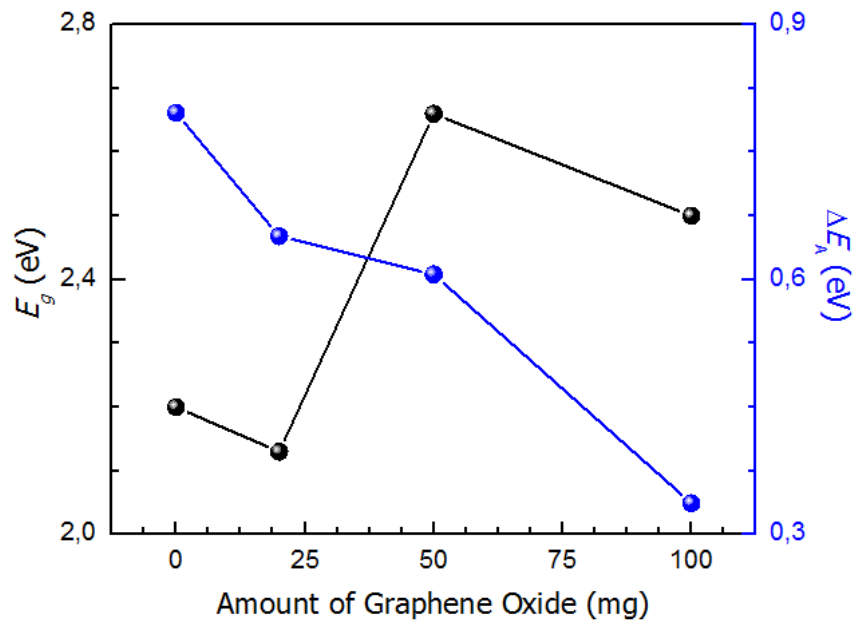


Figure 7. The plot of Kubelka–Munk relation for the yttrium ferrite nano electroceramics

The $hv-(\alpha hv)^2$ graphs of the samples were drawn and the point where the line opposite to the linear part of the graph intersected the axis hv at 0 was determined. Fig.7. shows the $hv-(\alpha hv)^2$ graphs of the samples. The values of the band gap (E_g) calculated with the help of these curves were shown in the Table 2. As can be seen from the Table 2, E_g values of the samples increased as the atomic rate of the doped Fe increased. The reason of the increase in the band gaps of the samples was the increase in the crystal size. Since the optical properties are were affected by the changes in the size of the nano-structure. The change in the band gap with the doping process is known as "Burstein-Moss" effect. The energy band gap is in the visible region and hence the $YFeO_3$ nanopowders in the current study are a good candidate for optical applications[25]. The variation of band gap and activation energy with the amount of graphene oxide are presented in Fig. 8.

Table 2. Optical band gap (E_g) and the activation energy (ΔE_A) of the nanopowders

| | E_g (eV) | Activation Energy (ΔE_A) (eV) | σ_{dc} (S/cm) (30°C) |
|---------------|------------|---|-----------------------------|
| YF0 | 2,20 | 0,796 | $1,09 \times 10^{-6}$ |
| YFO20 | 2,13 | 0,651 | $4,11 \times 10^{-7}$ |
| YFO50 | 2,66 | 0,606 | $3,53 \times 10^{-6}$ |
| YFO100 | 2,50 | 0,337 | $1,16 \times 10^{-6}$ |

**Figure 8.** The variation of band gap and activation energy with the amount of graphene oxide

3.3. Electrical characterization

The dielectric properties of the YFeO_3 samples were investigated in the frequency range from 1 kHz to 5 MHz. The relative permittivity (ϵ'), dielectric loss (ϵ'') and alternating current conductivity (σ_{ac}) were calculated using the following relations, respectively

The relative permittivity (ϵ'), dielectric loss (ϵ'') and alternating current conductivity (σ_{ac}) values of the samples were determined by the following relations [26, 27,36]:

$$\epsilon' = \frac{C_p \cdot t}{\epsilon_0 \cdot A} \quad (4)$$

$$\epsilon'' = \tan \delta \cdot \epsilon' \quad (5)$$

$$\sigma_{ac} = \frac{l}{Z \cdot A} \quad (6)$$

where ϵ_0 is the permittivity of free space, A is the area of the electrode, C is the capacitance, l is the thickness of the sample, $\tan \delta$ is the loss tangent and Z is the impedance. Using the equations from 2 to 4, the relative permittivity (ϵ'), dielectric loss (ϵ'') and alternating current conductivity (σ_{ac}) values were computed and their changes with increasing frequency were also plotted in Figs. 9, 10 and 11, respectively.

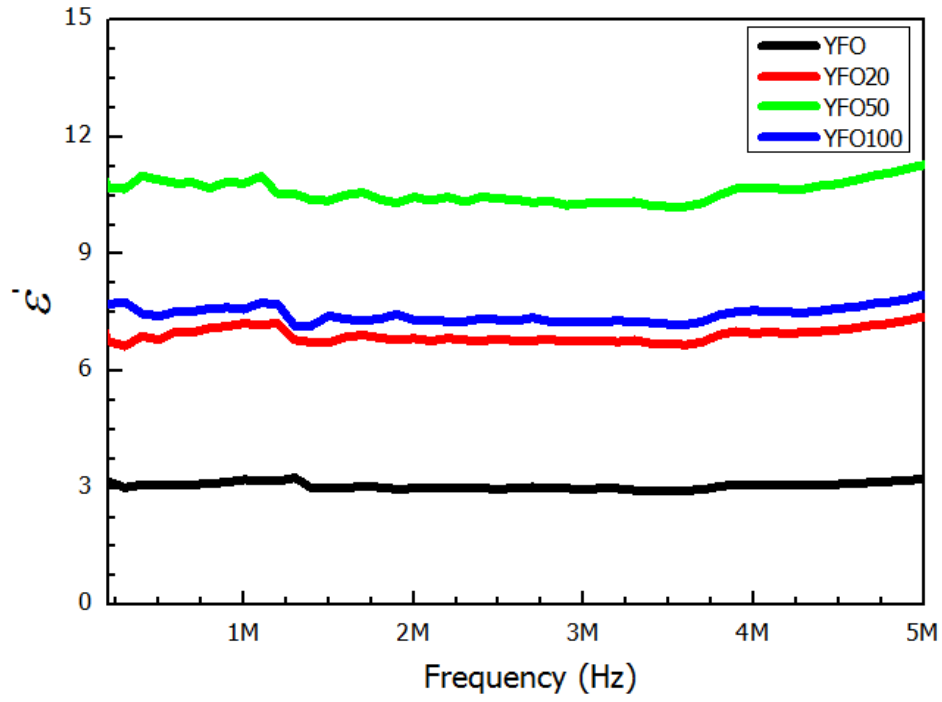


Figure 9. Relative permittivity as a function of frequency plots of the samples

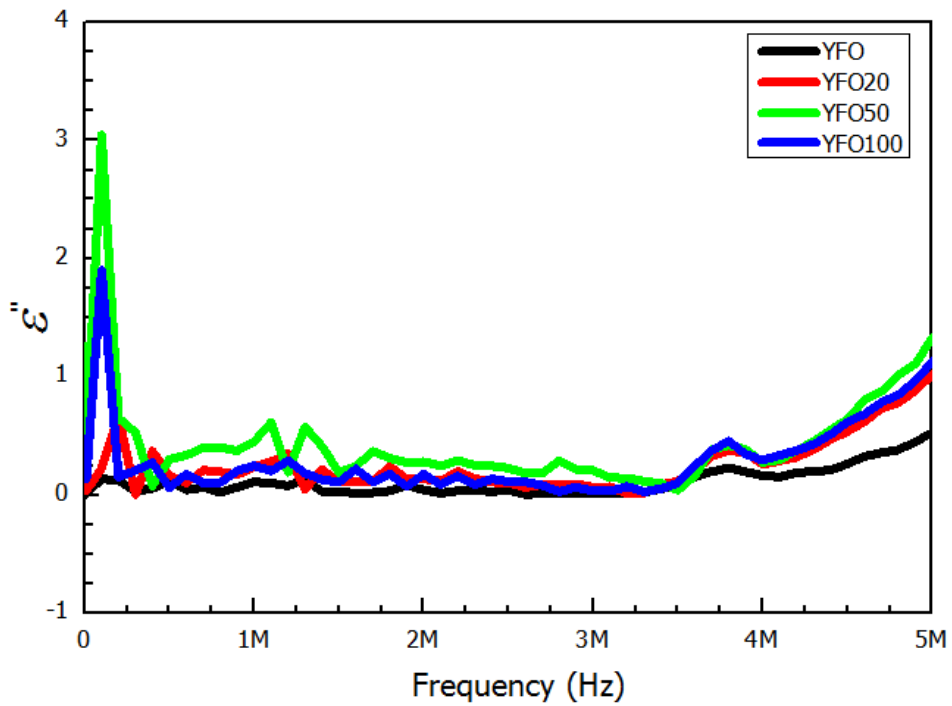


Figure 10. Dielectric loss as a function of frequency plots of the samples

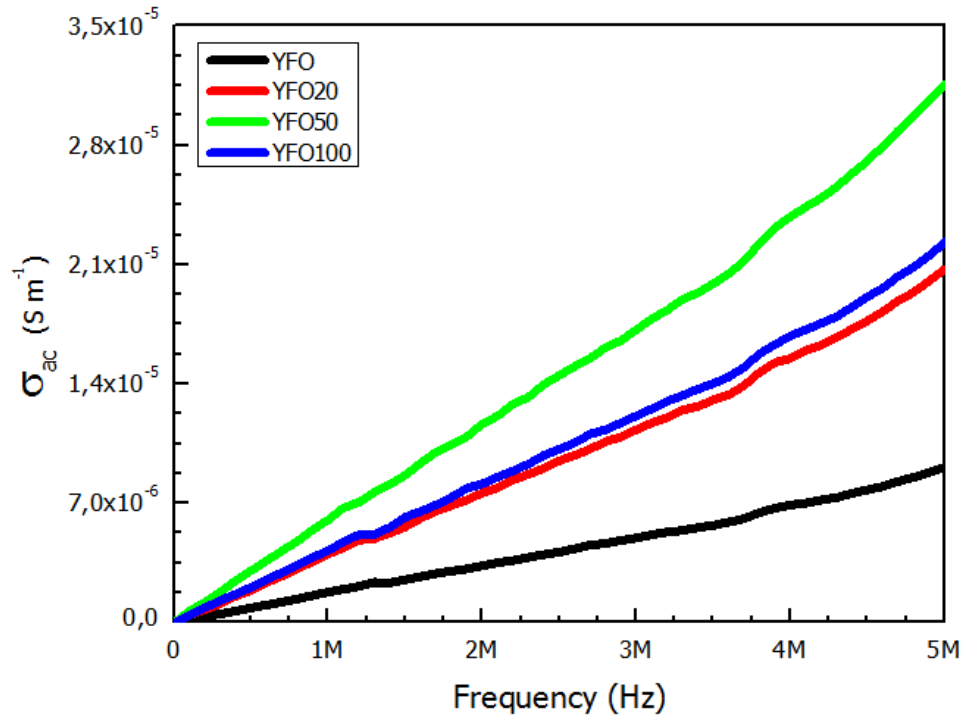


Figure 11. Alternating current conductivity vs. frequency plots of the samples

As can be seen from Figs. 9, 10 and 11, the relative permittivity (ϵ'), dielectric loss (ϵ'') and alternating current conductivity (σ_{ac}) are significantly affected by graphene oxide content, respectively. While the values of ϵ' and ϵ'' decrease with increasing of frequency, the σ_{ac} increases linearly, for each sample. In brief, graphene oxide-doping into YFeO_3 affects its dielectric properties and alternating current conductivity values. The relative permittivity value for each sample decreases at the higher frequencies in comparison to the lower ones since the contribution of the dipolar polarization is small at the higher frequencies because of the inertia of the molecules and ions. At the same time, the orientation of dipoles cannot adapt to the higher applied alternating fields, and this leads to the dielectric loss. The increase in the dielectric permittivity with the different graphene oxide-amount can be a sign of a percolation transition from an insulator to conductor.

The relative permittivity values of the nano electroceramic samples at different frequencies were given in Table 3.

Table 3. The relative permittivity values of the samples at different frequencies

| | ϵ' | | | | | | | | |
|---------------|---------------------------|----------------------------|-----------------------------|-----------------------------|---------------------------|---------------------------|---------------------------|---------------------------|---------------------------|
| | $\epsilon'_{1\text{kHz}}$ | $\epsilon'_{10\text{kHz}}$ | $\epsilon'_{100\text{kHz}}$ | $\epsilon'_{500\text{kHz}}$ | $\epsilon'_{1\text{MHz}}$ | $\epsilon'_{2\text{MHz}}$ | $\epsilon'_{3\text{MHz}}$ | $\epsilon'_{4\text{MHz}}$ | $\epsilon'_{5\text{MHz}}$ |
| YFO | 3,161 | 1,459 | 3,597 | 3,090 | 3,213 | 2,990 | 2,970 | 3,095 | 3,240 |
| YFO20 | 7,330 | 3,349 | 8,037 | 6,797 | 7,219 | 6,833 | 6,776 | 6,966 | 7,391 |
| YFO50 | 13,039 | 6,284 | 11,767 | 10,897 | 10,804 | 10,457 | 10,288 | 10,698 | 11,283 |
| YFO100 | 8,575 | 3,349 | 7,400 | 7,406 | 7,580 | 7,307 | 7,263 | 7,551 | 7,957 |

In order to determine the temperature-dependent variation of the produced undoped and graphene oxide-doped nano electroceramics and their electrical transmission mechanism, the temperature-dependent conductivity curves were used. The conductivity curves were analyzed using the equation known as Arrhenius equation [19, 20, 24, 28, 29,37] :

$$\sigma_{dc} = \sigma_0 \cdot \exp\left(\frac{\Delta E_A}{kT}\right) \quad (7)$$

In Equation 7, σ_0 ; is the exponential function, k ; Boltzmann constant and E_a represents the activation energy. In the light of the data, $\ln\sigma-1000/T$ change graphs were drawn for all samples and activation energies corresponding to the donor level were calculated.

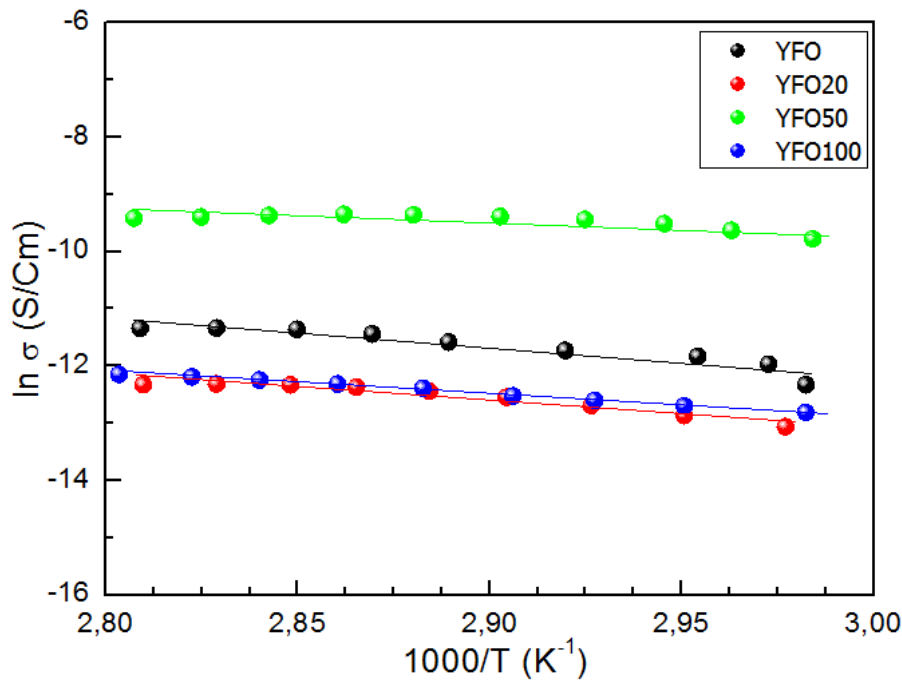


Figure 12. Temperature dependence of DC electrical conductivity of the yttrium ferrite samples

Fig.12. shows $\ln\sigma-1000/T$ graph of the samples. As seen in Fig.12., electrical conductivity of the samples changed as the amount of graphene oxide dopant changed. The highest conductivity value was observed in YFO50 sample. It was also clearly seen that as the temperature increased, the conductivity increased. For all the samples, a single conductivity mechanism occurred in the measured temperature range. This conductivity mechanism formed by the thermal excitation of the carrier loads. As the temperature increased, the electrons were thermally stimulated to the conductivity band from the donor levels. With increasing temperature, more load carrier contributed to the electrical conductivity by exceeding the activation energy barrier. The activation energy of the samples was calculated from the slope of the lines in the graph and was given in Table 2. When the values in Table 2 were examined, activation energies decreased in parallel with the increasing graphene oxide ratio. YFO100 sample had the lowest activation energy value. In addition, the conductivity values of the samples at room temperature changed based on the graphene oxide dopant. Table 2 shows the conductivity values of the samples at room temperature.

4. Discussion

Undoped and different mass ratio graphene oxide doped YFeO_3 based nanocomposite samples were prepared via hydrothermal method. Structural, morphological, chemical, optical and electrical properties of the samples were investigated. All of the results obtained from characterization show a change with graphene oxide contribution. As a result, in this study is especially important in terms of, nanoceramic semiconducting materials, which have an important place in technological applications, can be produced especially at low cost and easily and also offering the possibility to dope of graphene oxide, which is characterized as the superior feature material of our time. In addition, this article is an important guide for future studies on researching of physical and chemical properties of YFeO_3 based organic semiconductors with doping different elements and exploring the potential for use in advanced electronic applications.

References :

- [1]. Aydin, H.; El-Nasser, H. M.; Aydin, C.; Al-Ghamdi, A. A.; Yakuphanoglu, F. Synthesis and characterization of nanostructured undoped and Sn-doped ZnO thin films via sol-gel approach. *Applied Surface Science*, 350, (2015), pp.109-114.
- [2]. Ahmad, T.; Lone, I. H.; Ansari, S. G.; Ahmed, J.; Ahamad, T.; Alshehri, S. M. Multifunctional properties and applications of yttrium ferrite nanoparticles prepared by citrate precursor route. *Materials & Design*, 126, (2017), pp. 331-338.
- [3]. Zhang, C.; Wang, Z.; Yan, H.; Wang, X.; Kang, D.; Li, L. Structural and magnetic properties in $\text{YFe}_{0.8}\text{Mn}_{0.2}\text{O}_3$ ceramics. *Materials Letters*, 136, (2014), pp. 15-17.
- [4]. Zhang, Y.; Yang, J.; Xu, J.; Gao, Q.; Hong, Z. Controllable synthesis of hexagonal and orthorhombic YFeO_3 and their visible-light photocatalytic activities. *Materials Letters*, 81, (2012), pp. 1-4.
- [5]. Shen, T.; Hu, C.; Yang, W. L.; Liu, H. C.; Wei, X. L. Theoretical investigation of magnetic, electronic and optical properties of orthorhombic YFeO_3 : A first-principle study. *Materials Science in Semiconductor Processing*, 34, (2015), pp. 114-120.
- [6]. Ding, J.; Lü, X.; Shu, H.; Xie, J.; Zhang, H. Microwave-assisted synthesis of perovskite ReFeO_3 (Re: La, Sm, Eu, Gd) photocatalyst. *Materials Science and Engineering: B*, 171, (2010), pp. 31-34.
- [7]. Grabowska, E. Selected perovskite oxides: Characterization, preparation and photocatalytic properties—A review. *Applied Catalysis B: Environmental*, 186, (2016), pp. 97-126.
- [8]. Racu, A. V.; Ursu, D. H.; Kuliukova, O. V.; Logofatu, C.; Leca, A.; Miclau, M. Direct low temperature hydrothermal synthesis of YFeO_3 microcrystals. *Materials Letters*, 140, (2015), pp.107-110.
- [9]. Jabbarzare, S.; Abdellahi, M.; Ghayour, H.; Chami, A.; Hejazian, S. Mechanochemically assisted synthesis of yttrium ferrite ceramic and its visible light photocatalytic and magnetic properties. *Journal of Alloys and Compounds*, 688, (2014), pp. 1125-1130.
- [10]. Stevens, F.; Cloots, R.; Poelman, D.; Vertruyen, B.; Henrist, C. Low temperature crystallization of yttrium orthoferrite by organic acid-assisted sol-gel synthesis. *Materials Letters*, 114, (2014), pp. 136-139.

- [11]. Zhang, Y.; Feng, J.; Xu, J.; Chen, G.; Hong, Z. Solvothermal Synthesis and Visible-Light Driven Photocatalytic Properties of YFeO₃ Nanoparticles. *Integrated Ferroelectrics*, 151, (2014), pp. 108-115.
- [12]. Cho, Y. S.; Burdick, V. L.; Amarakoon, V. R. Hydrothermal preparation and morphology characteristics of Y₃Fe₅O₁₂. *Journal of the American Ceramic Society*, 80, (1997), pp. 1605-1608.
- [13]. Al-Hazmi, F. S.; Al-Ghamdi, A. A.; Bronstein, L. M.; Memesh, L. S.; Shokr, F. S.; Hafez, M. The influence of sintering temperature on the structure, optical and magnetic properties of Yttrium iron oxide YFeO₃ prepared via L α -alanine assisted combustion method. *Ceramics International*, 43, (2017), pp. 8133-8138.
- [14]. Lü, X.; Xie, J.; Shu, H.; Liu, J.; Yin, C.; Lin, J. Microwave-assisted synthesis of nanocrystalline YFeO₃ and study of its photoactivity. *Materials Science and Engineering: B*, 138, (2007), pp. 289-292.
- [15]. Aydin, C.; El-Nasser, H. M.; Yakuphanoglu, F.; Yahia, I. S.; Aksoy, M. Nanopowder synthesis of aluminum doped cadmium oxide via sol-gel calcination processing. *Journal of Alloys and Compounds*, 509, (2011), pp. 854-858.
- [16]. Aydin, C.; Al-Hartomy, O. A.; Al-Ghamdi, A. A.; Al-Hazmi, F.; Yahia, I. S.; El-Tantawy, F.; Yakuphanoglu, F. Controlling of crystal size and optical band gap of CdO nanopowder semiconductors by low and high Fe contents. *Journal of Electroceramics*, 29, (2012), pp. 155-162.
- [17]. Aydin, C.; Mansour, S. A.; Alahmed, Z. A.; Yakuphanoglu, F. Structural and optical characterization of sol-gel derived boron doped Fe₂O₃ nanostructured films. *Journal of Sol-Gel Science and Technology*, 62, (2012), pp. 397-403.
- [18]. Aydin, H.; Aydin, C.; Al-Ghamdi, A. A.; Farooq, W. A.; Yakuphanoglu, F. Refractive index dispersion properties of Cr-doped ZnO thin films by sol-gel spin coating method. *Optik*, 127, (2016), pp. 1879-1883.
- [19]. Aydin, C.; Khusayfan, N. M.; Al-Ghamdi, A. A.; El-Tantawy, F.; Farooq, W. A.; Yakuphanoglu, F. Facile synthesis, electrical and optical properties of Cu-doped GaN nanorods by sol-gel technique. *Journal of Sol-Gel Science and Technology*, 78, (2016) pp. 68-75.
- [20]. Aydin, C.; Benhaliliba, M.; Al-Ghamdi, A. A.; Gafer, Z. H.; El-Tantawy, F.; Yakuphanoglu, F. Determination of optical band gap of ZnO:ZnAl₂O₄ composite semiconductor nanopowder materials by optical reflectance method. *Journal of Electroceramics*, 31, (2013), pp. 265-270.
- [21]. Aydin, H.; Mansour, S. A.; Aydin, C.; Al-Ghamdi, A. A.; Al-Hartomy, O. A.; El-Tantawy, F.; Yakuphanoglu, F. Optical properties of nanostructure boron doped NiO thin films. *Journal of Sol-Gel Science and Technology*, 64, (2012), pp. 728-733.
- [22]. Orhan, A.; Aydin, C.; Aydin, H.; Al-Ghamdi, A. A.; El-Tantawy, F.; Yakuphanoglu, F. Synthesis and optical properties of iron doped gallium nitride nanostructures by sol gel method. *Microsystem Technologies-Micro-and Nanosystems-Information Storage and Processing Systems*, 21, (2015) pp. 1219-1224.
- [23]. Benhaliliba, M.; Benouis, C. E.; Yakuphanoglu, F.; Tiburcio-Silver, A.; Aydin, C.; Hamzaoui, S.; Mouffak, Z. Detailed investigation of submicrometer-sized grains of chemically sprayed (Sn_{1-x}Al_x, O-2) (0 ≤ x ≤ 0.085) thin films. *Journal of Alloys and Compounds*, 527, (2015), pp. 40-47.

- [24]. Guler, O.; Guler, S. H.; Yo, F.; Aydin, H.; Aydin, C.; El-Tantawy, F.; Duraia, E. M.; Fouda, A. N. Electrical and Optical Properties of Carbon Nanotube Hybrid Zinc Oxide Nanocomposites Prepared by Ball Mill Technique. *Fullerenes Nanotubes and Carbon Nanostructures*, 23, (2015) pp. 865-869.
- [25]. Wang, M.; Wang, T.; Song, S. H.; Ravi, M.; Liu, R. C.; Ji, S. S. Effect of calcination temperature on structural, magnetic and optical properties of multiferroic YFeO₃ nanopowders synthesized by a low temperature solid-state reaction. *Ceramics International*, 43, (2017), pp. 10270-10276.
- [26]. Kaygili, O.; Dorozhkin, S. V.; Ates, T.; Canan Gursoy, N.; Keser, S.; Yakuphanoglu, F.; Birkan Selçuk, A. Structural and dielectric properties of yttrium-substituted hydroxyapatites. *Materials Science and Engineering: C*, 47, (2015), pp. 333-338.
- [27]. Kaygili, O.; Tatar, C.; Yakuphanoglu, F. Structural and dielectrical properties of Mg₃-Ca₃(PO₄)₂ bioceramics obtained from hydroxyapatite by sol-gel method. *Ceramics International*, 38, (2012), pp. 5713-5722.
- [28]. Kaygili, O.; Keser, S.; Ates, T.; Yakuphanoglu, F. Synthesis and characterization of lithium calcium phosphate ceramics. *Ceramics International*, 39, (2013), pp. 7779-7785.
- [29]. Aydin, C.; Abd El-sadek, M. S.; Zheng, K. B.; Yahia, I. S.; Yakuphanoglu, F. Synthesis, diffused reflectance and electrical properties of nanocrystalline Fe-doped ZnO via sol-gel calcination technique. *Optics and Laser Technology*, 48, (2013), pp. 447-452.
- [30]. Aydin, C. Synthesis of SnO₂:rGO nanocomposites by the microwave-assisted hydrothermal method and change of the morphology, structural, optical and electrical properties. *Journal of Alloys and Compounds*, 771, (2019), pp. 964-972.
- [31]. Aydin, C. Synthesis of Pd:ZnO nanofibers and their optical characterization dependent on modified morphological properties. *Journal of Alloys and Compounds*, 777, (2019), pp. 145-151.
- [32]. Aydin, H.; Yakuphanoglu, F.; Aydin, C. Al-doped ZnO as a multifunctional nanomaterial: Structural, morphological, optical and low-temperature gas sensing properties. *Journal of Alloys and Compounds*, 773, (2019), pp. 802-811.
- [33]. Aydin, H.; Gündüz, B.; Aydin, C. Surface morphology, spectroscopy, optical and conductivity properties of transparent poly(9-vinylcarbazole) thin films modified with graphene oxide. *Synthetic Metals*, 252, (2019), pp. 1-7.
- [34]. Aydin, C.; Aydin, H.; Taskin, M.; Yakuphanoglu, F. A Novel Study: The Effect of Graphene Oxide on the Morphology, Crystal Structure, Optical and Electrical Properties of Lanthanum Ferrite Based Nano Electroceramics Synthesized by Hydrothermal Method. *Journal of Nanoscience and Nanotechnology*, 19, (2019), pp. 2547-2555.
- [35]. Aydin, C. The functionalization of morphological, structural and optical properties of Fe doped SnO₂ nanocrystals synthesized by the sol-gel method. *Journal of Materials Science: Materials in Electronics*, 29, (2018), pp. 20087-20096.
- [36]. Aydin, C. Tin Oxide Based Nano Electroceramics Obtained from Sol-Gel Process: The Modified of the Structural and Opto-Electrical Properties with the Al Doping. *Journal of Nanoelectronics and Optoelectronics*, 13, (2018), pp. 1460-1467.
- [37]. Aydin, C. Variation of structural and electrical properties of gallium nitride-based nanomaterials with nickel dopant at different atomic ratios. *Ceramics International*, 44, (2018), pp.17473-17478.

THE EVALUATING OF WIND ENERGY POTENTIAL OF DİYARBAKIR USING WEIBULL AND RAYLEIGH DISTRIBUTION

Fatih KOÇYİĞİT^{1}*

In comparison to fossil fuel that pollutes the lower layer of the atmosphere, wind energy is an alternative clean source of energy. Wind speed is the parameter with primary importance in designing and studying the wind energy conversion systems. In this study, the statistical analysis of the parameters of wind power density and wind speed distribution was investigated using the wind speed data of Diyarbakır province between the years 2014 and 2018 that were hourly measured by the General Directorate of Meteorology. Wind data are used to derive probability distributions, and their distributional parameters are determined. Two probability density functions are suited to the measured probability distributions on a yearly basis. The Weibull and the Rayleigh models are used to analyze the wind energy potential of the location. This modeling process was evaluated according to R^2 , RMSE and χ^2 parameters. In conclusion, the values obtained by the Weibull model gave better results than the values obtained by the Rayleigh model in the wind data analysis of Diyarbakır province.

Key words: *Wind Energy, Rayleigh Distribution, Weibull Distribution*

1. Introduction

As the world population grows rapidly, the demand for energy increases proportionally. Despite the increasing demand for energy, limited fossil fuel reserves, quality energy and the efficient use of energy produced have become important issues especially in developing countries like Turkey. Turkey has a fairly high level of renewable energy sources to meet a certain part of the total demand for energy [1]. Wind energy has a renewable property and is also known as an environmentally clean energy source among these energy sources [2]. There is no transport problem in wind energy, and also its use does not require a high technology. Wind is formed by the temperature and pressure difference caused by the warming and cooling of the atmosphere. Wind is a stable, reliable, continuous and kinetic energy source. Especially in recent years, investments in converting wind power potential into electric energy have been increasing much faster along with the development of turbine technology. In order to benefit from wind energy which exists as long as the sun and the world exist and is a renewable energy source, it needs to be converted to another form of energy [3]. With the help of meteorological data, distributions of the most suitable regional wind regimes can be determined by using various computer programs [4-5]. In addition, in many studies, meteorological data were used for statistical analysis in solar energy applications [6-9]. In the studies carried out in the literature, the wind speed frequency distribution is

¹ Department of Airframes and Powerplanets, School of Civil Aviation, Dicle University, Turkey (fatih.kocyigit@dicle.edu.tr) 
<http://orcid.org/0000-0001-6383-3163>

shown using different distributions such as Gamma, log normal, Rayleigh. On the other hand, the two-parameter Weibull distribution and the one-parameter Rayleigh distribution are the methods that have been used to represent the wind distribution of many regions of the world in recent years. The reasons for using these methods are the factors such as their good compliance with the wind distribution, the flexibility of the distributions, the ease of determination of parameters, small number of parameters, predictability of different heights after determining parameters for a height [10]. Hourly average wind speed data measured at a height of 30 meters at Diyarbakır meteorological station of the Turkish State Meteorological Service between the years 2014 and 2018 were used in this study. Weibull and Rayleigh functions were analyzed statistically to determine the wind energy potential of Diyarbakır province. Statica and Matlab programs were used in the analyses of the study. Weibull and Rayleigh probability density function, cumulative distribution function, average wind speed, standard deviation of wind speed, maximum wind speed and wind power density were determined in statistical analyses. The root mean square error (RMSE), Chi-square (χ^2) and correlation coefficient (R2) were used to evaluate the performance of Weibull and Rayleigh functions.

2. Wind speed data

In this study, hourly time series wind speed data in Diyarbakır that were measured between the years 2014 and 2018 were statistically analyzed. Wind speed data were continuously recorded at a height of 30 m using a cup-generator anemometer located at the Diyarbakır station of the Turkish State Meteorological Service. The continuously recorded wind speed data were averaged over 1 hour and stored as hourly values.

3. Performance analysis

The model selection criteria required in determining the optimal statistical distribution for the observed wind speed are introduced in this section.

3.1. Statistical criteria

In the literature, there are studies on the wind speed statistics [11-24]. Rayleigh distributions, where the two parameter Weibull and Weibull shape parameters are 2, are the most widely used distributions. Rayleigh distribution is less flexible than Weibull since it is single parameter, but the calculation of parameters is easier. It is known that the wind speed distribution approaches the Rayleigh distribution in the case where annual average wind speed is greater than 4.5 [10].

The general expression of the two parameter Weibull probability density function is presented in Eq. 1.

$$f_w(v) = \left(\frac{k}{c}\right) \left(\frac{v}{c}\right)^{k-1} \exp\left[-\left(\frac{v}{c}\right)^k\right] \quad (1)$$

Here, k and c are the shape and scale parameters, respectively. The scale parameter c also has a reference value in the wind data. Weibull cumulative distribution function is determined by Eq. 2.

$$F_w(v) = 1 - \exp\left[-\left(\frac{v}{c}\right)^k\right] \quad (2)$$

The shape parameter is around 1 near the equator, 2 at temperate latitudes and around 3 for continuous wind areas [25].

The probability density function of the Rayleigh distribution and the cumulative distribution function are presented by Eq. 3 and Eq. 4.

$$f_w(v) = \frac{2v}{c^2} \exp\left[-\left(\frac{v}{c}\right)^2\right] \quad (3)$$

$$F_R(v) = 1 - \exp\left[-\left(\frac{v}{c}\right)^2\right] \quad (4)$$

The biggest advantage of Rayleigh distribution is the determination of the distribution only with the average wind speed. The validity of Rayleigh distribution in wind studies was shown in many references [26]. In this study, the least squares method was used to find the parameters of the Weibull and Rayleigh distributions [10, 26]. The average wind speed and the standard deviation of the wind speed are calculated using Eq. 5 and Eq. 6, respectively.

$$v_m = c \Gamma\left(1 + \frac{1}{k}\right) \quad (5)$$

$$\sigma = \sqrt{c^2 \left[\Gamma\left(1 + \frac{2}{k}\right) - \Gamma^2\left(1 + \frac{1}{k}\right) \right]} \quad (6)$$

where $\Gamma(\cdot)$ is the gamma function.

Based on the Weibull distribution, the wind speed with the largest frequency is calculated from Eq. 7 [8].

$$V_{\text{mod}} = c \left(1 - \frac{1}{k}\right)^{1/k} \quad (7)$$

Maximum wind speed is found by Eq. 8 [6].

$$V_{\text{max}} = c \left(\frac{k+2}{k}\right)^{1/k} \quad (8)$$

When it is $k=2$ in the above-mentioned formulas, calculations are made for the Rayleigh distribution. The average wind power density is most generally calculated from Eq. 9:

$$P_m = \int_0^{\infty} P(v) f(v) dv \quad (9)$$

The average power density for the Weibull distribution is obtained from Eq. 10 as follows [10].

$$P_W = \frac{1}{2} \rho c^3 \left(1 + \frac{3}{k} \right) \quad (10)$$

The average power density for Rayleigh distribution is determined by Eq. 11:

$$P_R = \frac{3}{\pi} \rho (v_m)^3 \quad (11)$$

In this study, the coefficient of determination (R^2) based on the theoretical and observed probabilities of distributions, root mean square error (RMSE) and chi-square (χ^2) criteria were selected as Eq. 12, Eq. 13 and Eq. 14 in the statistical modeling of wind speed data of distributions:

$$R^2 = \frac{\sum_{i=1}^N (y_i - z_i)^2 - \sum_{i=1}^N (x_i - y_i)^2}{\sum_{i=1}^N (y_i - z_i)^2} \quad (12)$$

$$\chi^2 = \frac{\sum_{i=1}^N (y_i - x_i)^2}{N - n} \quad (13)$$

$$RMSE = \left[\frac{1}{N} \sum_{i=1}^N (y_i - x_i)^2 \right]^{1/2} \quad (14)$$

where y_i is the measured data, z_i is the mean value, x_i is the predicted data with the Weibull or Rayleigh distribution, N is the number of observations and n is the number of constants. Thus, the more distribution function can be selected by the highest value of R^2 and the lowest values of RMSE and χ^2 . R^2 ranges between 0 and 1 as a measure of the predictive power of a model and its approaches to 1 indicates that predictive power of the model has increased [26].

4. Results and discussion

The monthly mean wind speeds are presented in Figure 1. As it can be seen in Figure 1, the mean wind speed varies between 1.78 m/s and 3.14 m/s, with a yearly mean of 2.64 m/s. Maximum value of the mean wind speed is 4.5 m/s in July of 2016, whereas minimum value is 1.30 m/s in November of 2014.

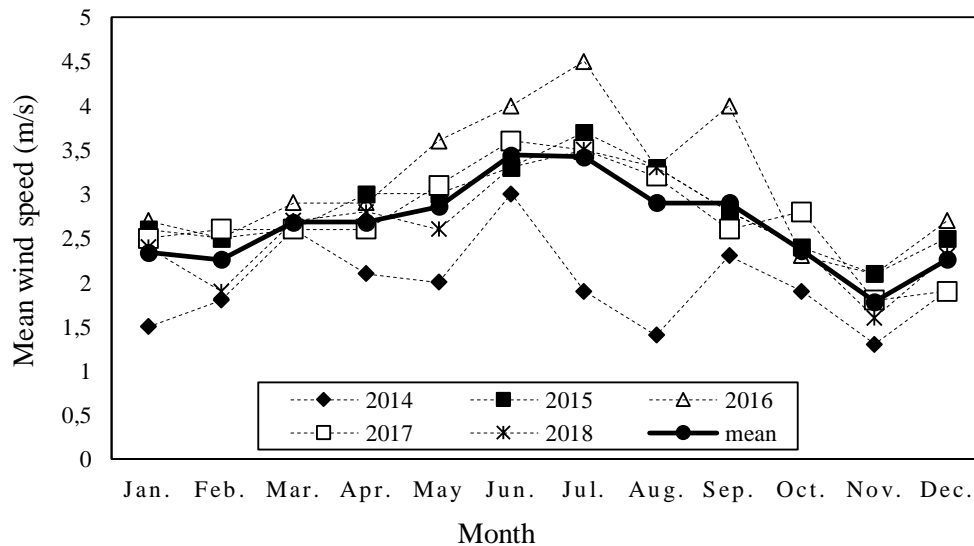


Figure 1. Monthly mean wind speed in Diyarbakır

The diurnal variation of the mean wind speed values is plotted in Figure 2. According to the yearly average results, the wind speed is the lowest as 0.98 m/s the hours of 03:00 in 2014, and is the highest as 4.33 m/s the hours of 13:00 in 2016.

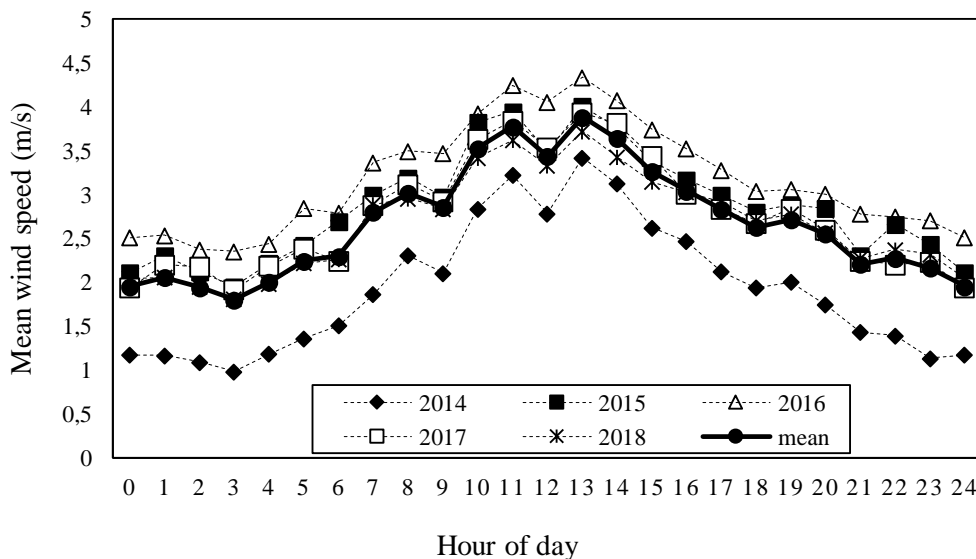


Figure 2. Diurnal variation of mean wind speed for the period of 2014–2018 in Diyarbakır

In Table 1, available time-series data were arranged as frequency distribution format for the period between 2014 and 2018. In the second column of Table 1, wind speed is grouped into classes. In the third column, mean wind speeds are calculated for each speed class intervals. The fourth column shows the frequency of the occurrence of each speed class. The probability density distribution is presented in the fifth column. In the last columns, the theoretical frequency values calculated from the Weibull and Rayleigh distributions are presented, respectively.

Table 1. Comparison of the actual probability distribution of wind speeds derived from measured data with Weibull and Rayleigh approximations for whole years

| j | v_j | $v_{m,j}$ | Actual data | Weibull distribution | Rayleigh distribution |
|----|-------|-----------|-------------|----------------------|-----------------------|
| 1 | 0-1 | 0.5 | 0.1398264 | 0.1511543 | 0.1808638 |
| 2 | 1-2 | 1.5 | 0.2055449 | 0.2271100 | 0.2467099 |
| 3 | 2-3 | 2.5 | 0.2752245 | 0.2466999 | 0.2156508 |
| 4 | 3-4 | 3.5 | 0.1630558 | 0.1856827 | 0.1543006 |
| 5 | 4-5 | 4.5 | 0.0865043 | 0.0967622 | 0.0959776 |
| 6 | 5-6 | 5.5 | 0.0524023 | 0.0360599 | 0.0515152 |
| 7 | 6-7 | 6.5 | 0.0372452 | 0.0103187 | 0.0236582 |
| 8 | 7-8 | 7.5 | 0.0203999 | 0.0024959 | 0.0093202 |
| 9 | 8-9 | 8.5 | 0.0106799 | 0.0005762 | 0.0031719 |
| 10 | 9-10 | 9.5 | 0.0048804 | 0.0001505 | 0.0009396 |
| 11 | 10-11 | 10.5 | 0.0023715 | 4.95245E-05 | 0.0002440 |
| 12 | 11-12 | 11.5 | 0.0009869 | 1.90944E-05 | 5.58849E-05 |
| 13 | 12-13 | 12.5 | 0.0005129 | 7.72884E-06 | 1.13513E-05 |
| 14 | 13-14 | 13.5 | 0.0003252 | 3.1318E-06 | 1.93884E-06 |
| 15 | 14-15 | 14.5 | 0.0001313 | 1.25641E-06 | 3.17865E-07 |

The yearly probability density and the cumulative distributions derived from the time-series data of Diyarbakır are presented in Figures 3 and 4, respectively. The yearly probability density and the cumulative distributions are presented in Figure 5 for all years.

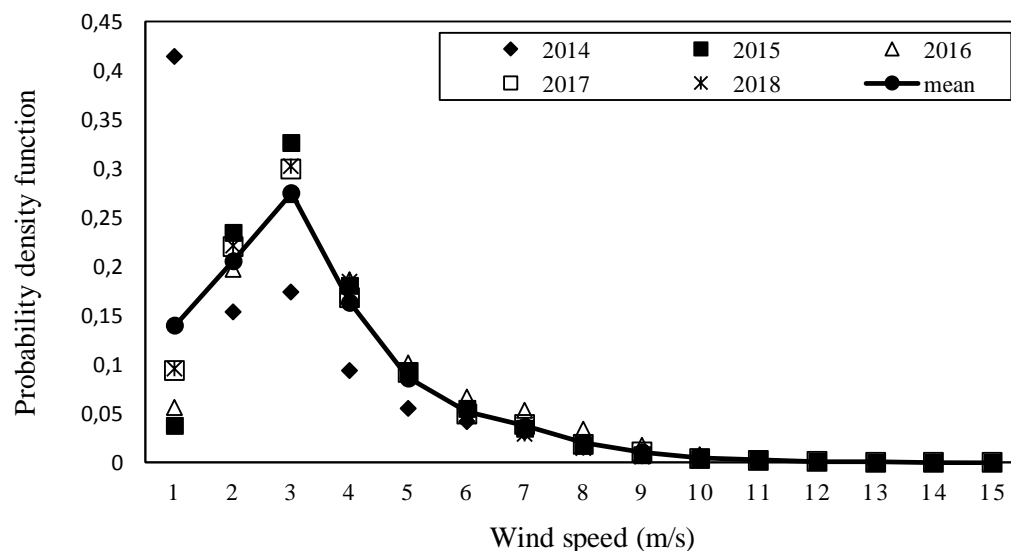


Figure 3. Yearly wind speed probability density distributions, derived from the measured hourly time series

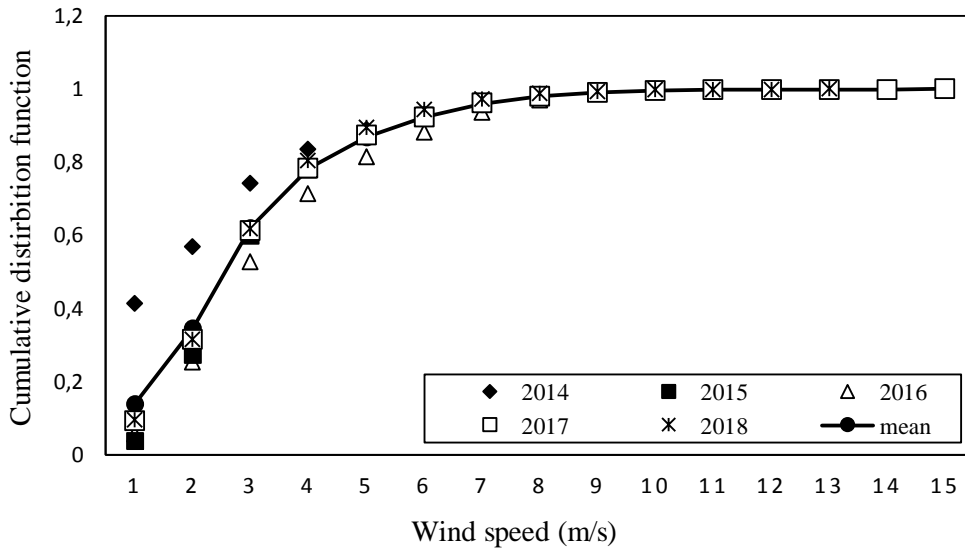


Figure 4. Yearly wind speed cumulative probability distributions, derived from the measured hourly time-series.

The monthly mean wind speed values (v_m) and standard deviations (σ) are presented in Table 2 to Weibull distribution for Diyarbakır, the period of 2014–2018. Most of the monthly mean wind speed values are between 1.0 m/s and 4.0 m/s, but only a few of them are over 4.0 m/s and under 2.0 m/s. In general, it is determined that the highest mean wind speed values are in June and July, and the lowest mean wind speed values are in November and December. After analyzing 48 months of the wind speed data, it is possible to conclude that the wind speed distribution significantly differs from one month to the next. The monthly and yearly standard deviation values are mostly between 1.0 m/s and 3.0 m/s, with only a few under 4.0 m/s.

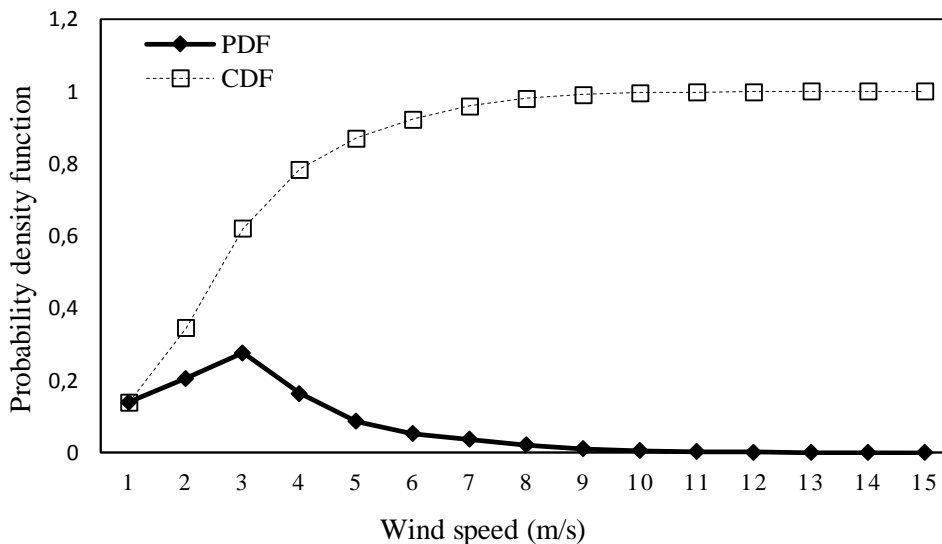


Figure 5. Yearly wind speed probability density and cumulative probability distributions derived from the measured data for whole years

Table 2. Monthly mean wind speed and standard deviations to Weibull distribution

| Years | 2014 | | 2015 | | 2016 | | 2017 | | 2018 | |
|------------------|-------|----------|-------|----------|-------|----------|-------|----------|-------|----------|
| | v_m | σ | v_m | σ | v_m | σ | v_m | σ | v_m | σ |
| January | 1.180 | 0.323 | 2.820 | 1.517 | 2.832 | 1.182 | 2.967 | 1.583 | 2.977 | 1.584 |
| February | 2.531 | 1.598 | 3.011 | 2.613 | 3.058 | 2.692 | 2.824 | 1.125 | 2.497 | 1.033 |
| March | 2.812 | 0.871 | 3.005 | 2.746 | 3.358 | 2.768 | 3.074 | 2.597 | 3.037 | 2.393 |
| April | 2.466 | 1.899 | 3.278 | 2.784 | 3.362 | 2.066 | 3.114 | 2.521 | 3.271 | 2.716 |
| May | 2.365 | 1.088 | 2.298 | 1.170 | 2.297 | 1.395 | 2.258 | 1.145 | 3.124 | 2.737 |
| June | 1.803 | 1.206 | 2.317 | 1.437 | 2.976 | 1.066 | 2.282 | 1.843 | 2.295 | 1.741 |
| July | 2.409 | 0.869 | 2.992 | 1.056 | 2.980 | 1.316 | 2.309 | 1.927 | 2.290 | 1.985 |
| August | 1.056 | 0.969 | 2.313 | 1.455 | 2.311 | 1.567 | 2.287 | 1.317 | 2.282 | 1.006 |
| September | 1.599 | 0.664 | 3.392 | 2.049 | 2.305 | 1.991 | 3.115 | 2.770 | 3.398 | 2.317 |
| October | 2.601 | 1.401 | 2.974 | 1.549 | 2.867 | 1.488 | 3.214 | 1.640 | 3.016 | 2.423 |
| November | 1.593 | 0.564 | 2.833 | 1.326 | 2.570 | 1.867 | 2.440 | 1.920 | 2.396 | 1.856 |
| December | 2.535 | 1.298 | 2.814 | 1.230 | 3.127 | 2.595 | 2.420 | 1.890 | 2.711 | 1.071 |

The yearly values of the two Weibull parameters, the scale parameter c (m/s) and shape parameter k (dimensionless), calculated from the long term wind data for Diyarbakır are presented in Table 3. Furthermore, monthly values of k and c are also presented in Table 3. It is obvious that the parameter k has a much smaller, temporal variation than the parameter c . The range of k is between 0.861 and 3.42, while the c value varies between 0.923 to 5.70 m/s. The lowest value of the scale parameter is 0.923 m/s and is found in July of 2014, while the highest value is 5.70, which occurred in July of 2016. The highest k value is in December of 2014 and the lowest is found in June of 2014. The mean k and c values are 2.47 and 3.27 m/s, respectively. The mean wind intensity and standard deviation values are important in predicting the shape and scale parameters.

Table 3. Monthly shape parameter (k) and scale parameter (c) values distribution for period of 2014-2018

| Years | 2014 | | 2015 | | 2016 | | 2017 | | 2018 | |
|------------------|--------|--------|--------|--------|--------|--------|--------|--------|--------|--------|
| | k | c | k | c | k | c | k | c | k | c |
| January | 2.1509 | 1.3649 | 3.0342 | 3.0143 | 2.1729 | 3.1172 | 2.7634 | 3.1698 | 2.7378 | 3.2835 |
| February | 1.5694 | 2.7567 | 3.0341 | 3.1927 | 2.9882 | 3.2845 | 2.0884 | 3.1645 | 2.7785 | 2.7825 |
| March | 1.3298 | 3.0348 | 3.3374 | 3.1696 | 2.3797 | 3.6661 | 2.6394 | 3.3692 | 2.2728 | 3.3516 |
| April | 1.0493 | 1.9211 | 2.9098 | 3.4049 | 3.0479 | 3.5854 | 2.2860 | 3.4716 | 2.5746 | 3.5141 |
| May | 1.1825 | 1.1309 | 2.9503 | 3.7306 | 2.3783 | 4.2768 | 2.3694 | 4.0386 | 2.8424 | 3.3962 |
| June | 0.8618 | 2.1454 | 2.5112 | 4.2356 | 2.6510 | 4.7366 | 2.6246 | 4.5460 | 3.0244 | 4.1953 |
| July | 1.5072 | 0.9238 | 2.7949 | 4.6279 | 2.8789 | 5.7097 | 2.9261 | 4.4236 | 2.5325 | 4.7439 |
| August | 1.6694 | 1.0230 | 2.8323 | 4.0554 | 3.0107 | 4.0496 | 2.6403 | 4.0432 | 3.1674 | 4.3388 |
| September | 0.9979 | 1.6627 | 2.9533 | 3.6205 | 2.2008 | 4.9795 | 2.9385 | 3.3787 | 3.2850 | 3.6799 |
| October | 1.2652 | 2.5233 | 2.9344 | 3.1827 | 3.0083 | 3.0936 | 2.5876 | 3.4361 | 2.3261 | 3.3562 |
| November | 1.3567 | 1.6558 | 2.7325 | 3.0730 | 2.2164 | 2.8545 | 2.7242 | 2.7005 | 2.6145 | 2.6851 |
| December | 3.4263 | 2.7561 | 2.6878 | 3.0041 | 2.6328 | 3.3703 | 2.7104 | 2.6788 | 2.3312 | 3.0085 |

In Figure 6, the variation of the Weibull probability distribution with wind speed is plotted by years. The highest probability value according to the Weibull probability distribution function was obtained as 0.35 in 2014.

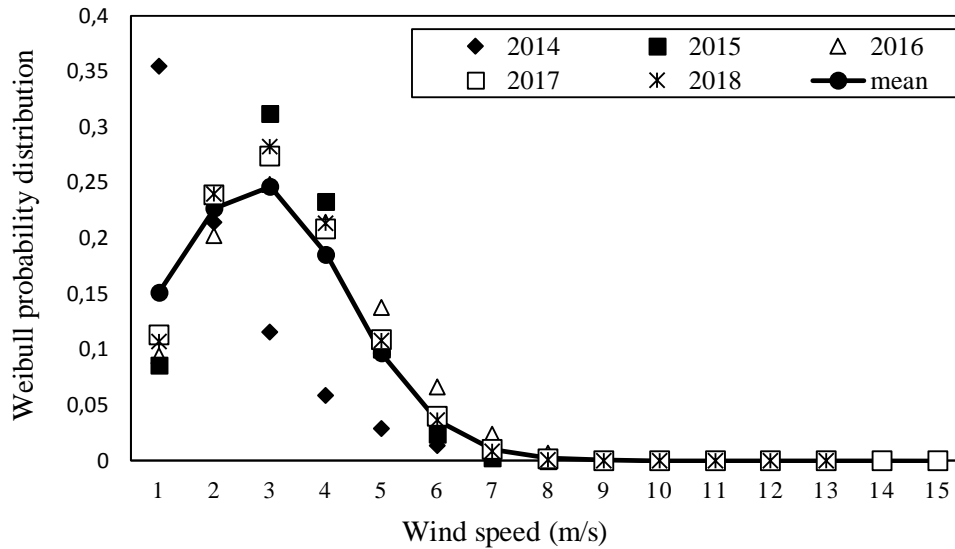


Figure 6. Yearly Weibull probability density distributions for the period of 2014-2018 in Diyarbakir

The Weibull and Rayleigh approximations of the actual probability distribution of wind speeds are presented in Figure 7, while a comparison of the two approximations is presented in Table 4. In Figure 7, the probability distribution of the actual data, the Weibull probability distribution, and the Rayleigh probability distribution are plotted versus the wind speed according to the average of five years data. The probability ratio of the Rayleigh distribution is higher than the Weibull distribution.

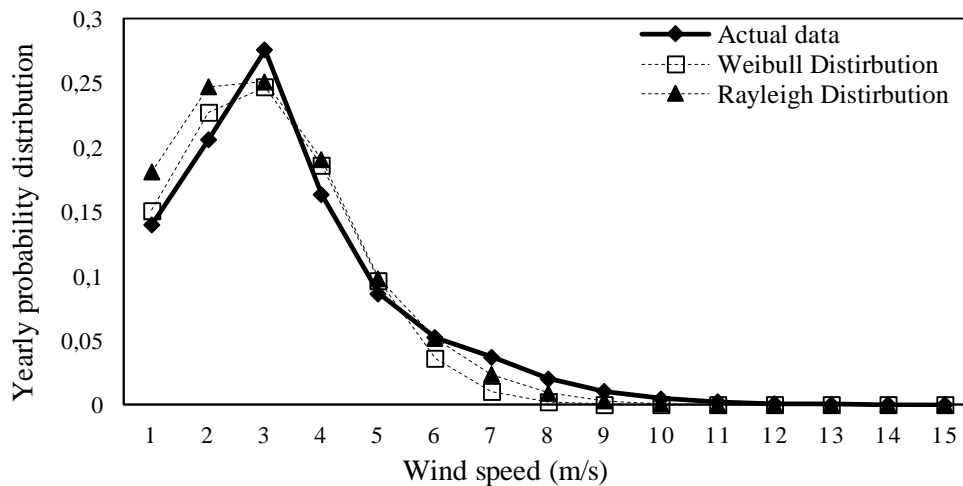


Figure 7. Weibull and Rayleigh approximations of the actual probability distribution of wind speeds

The values of the statistical parameters (R^2 , $RMSE$, and χ^2) obtained from Weibull and Rayleigh distributions are given in Table 4. The R^2 value is found between 0.92-0.98 in the Weibull distribution and 0.90-0.93 in the Rayleigh distribution. The $RMSE$ values range from 1.09×10^{-5} to 4.72×10^{-5} in the

Weibull distribution and from 2.69×10^{-5} to 1.84×10^{-4} in the Rayleigh distribution. The χ^2 values vary between 2.59×10^{-5} and 1.08×10^{-4} in the Weibull distribution and between 6.61×10^{-5} and 3.95×10^{-4} in the Rayleigh distribution. As can be seen in Table 4, the highest R^2 value is obtained by using the Weibull distribution. However, the results have shown that the $RMSE$ and χ^2 values of the Weibull distribution are lower than the values obtained for the Rayleigh distribution. As a result, the Weibull approximation is found to be the most accurate distribution according to the highest value of R^2 and the lowest values of $RMSE$ and χ^2 .

Table 4. The statistical analysis parameters for yearly wind speed distributions in Diyarbakır

| Years | Weibull Distribution | | | Rayleigh Distribution | | |
|-------|----------------------|------------|-----------|-----------------------|------------|-----------|
| | R^2 | RMSE | χ^2 | R^2 | RMSE | χ^2 |
| 2014 | 0.919 | 0.00047219 | 0.0010897 | 0.900 | 0.00184337 | 0.0039501 |
| 2015 | 0.947 | 0.00025287 | 0.0005835 | 0.911 | 0.00068175 | 0.0014609 |
| 2016 | 0.941 | 0.00020512 | 0.0004733 | 0.915 | 0.00029723 | 0.0006369 |
| 2017 | 0.963 | 0.00015103 | 0.0003485 | 0.934 | 0.00026925 | 0.0005770 |
| 2018 | 0.976 | 0.00010960 | 0.0002591 | 0.933 | 0.00030541 | 0.0006617 |

Fig. 8 shows the monthly change in the R^2 obtained from the Weibull and Rayleigh distributions for Diyarbakır using the ten-year data. The range of R^2 values change from 0.89 to 0.93 in the Weibull distribution and 0.89 to 0.97 in the Rayleigh distribution. Because the R^2 value is closer to 1 in the Weibull distribution, it is understood that the Weibull distribution is more suitable for modeling the wind data for Diyarbakır.

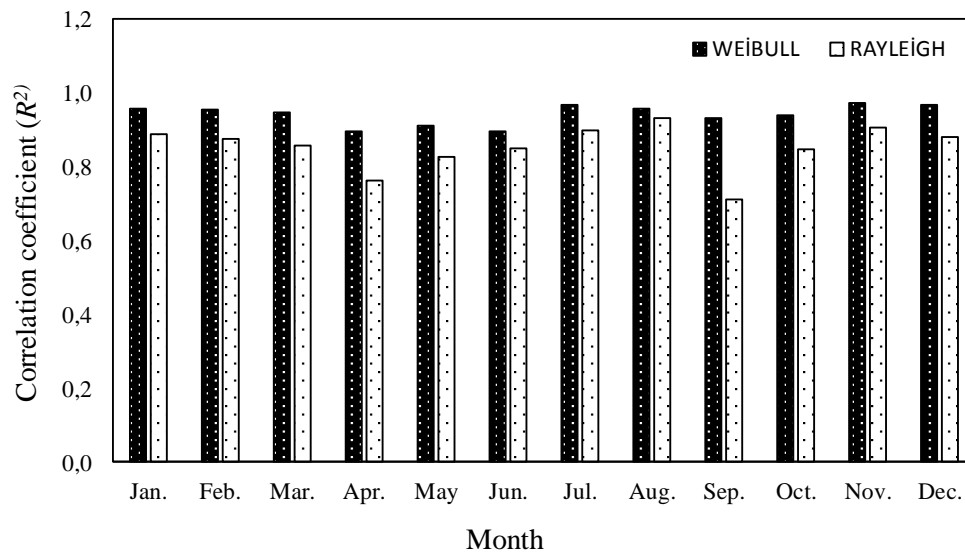


Figure 8. The change of correlation coefficient values obtained from Weibull and Rayleigh distribution to months

The Weibull distribution parameters and the Rayleigh distribution parameters are given in Table 5 and Table 6 according to years, respectively. The maximum mean velocity (V_{max}) in the Weibull distribution ranged from 4.23 to 5.02 m/s and the mean power density (P_w) ranged from 17.87 to 41.99 W/m². In the Rayleigh distribution, V_{max} varied from 2.95 to 5.22 m/s and P_R varied from 11.95 to 26.20 W/m².

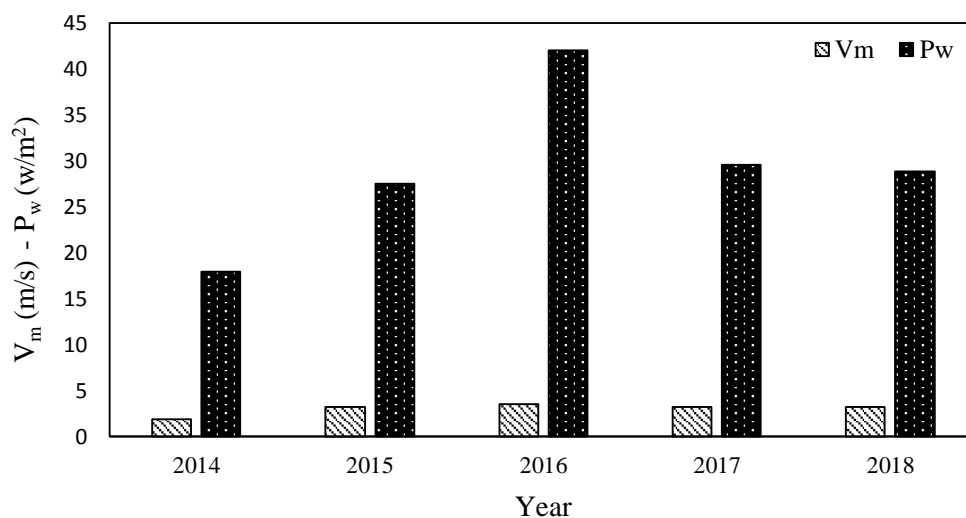
Table 5. Weibull distribution parameters

| Years | k | c(m/s) | V _m (m/s) | σ(m/s) | V _{mod} (m/s) | V _{max} (m/s) | P _w (W/m ²) |
|-------|--------|--------|----------------------|---------|------------------------|------------------------|------------------------------------|
| 2014 | 1.5305 | 1.9082 | 1.79101 | 1.89879 | 0.3530 | 4.2385 | 17.867 |
| 2015 | 2.8927 | 3.5259 | 3.14357 | 3.90231 | 2.9562 | 4.2554 | 27.465 |
| 2016 | 2.6305 | 3.8937 | 3.46241 | 4.16010 | 3.0463 | 5.0254 | 41.991 |
| 2017 | 2.6082 | 3.5350 | 3.14177 | 3.76184 | 2.8014 | 4.5430 | 29.579 |
| 2018 | 2.7073 | 3.5280 | 3.14007 | 3.81948 | 2.8385 | 4.4730 | 28.852 |

Table 6. Rayleigh distribution parameters

| Years | c(m/s) | V _m (m/s) | σ(m/s) | V _{mod} (m/s) | V _{max} (m/s) | P _R (W/m ²) |
|-------|--------|----------------------|---------|------------------------|------------------------|------------------------------------|
| 2014 | 2.3461 | 2.07913 | 2.33091 | 1.4762 | 2.9524 | 11.957 |
| 2015 | 3.2013 | 2.83712 | 3.48380 | 2.6102 | 5.2204 | 26.049 |
| 2016 | 3.2011 | 2.83686 | 3.37859 | 2.8209 | 5.6418 | 26.201 |
| 2017 | 3.0376 | 2.69196 | 3.18978 | 2.5545 | 5.1089 | 22.546 |
| 2018 | 3.1306 | 2.77441 | 3.32709 | 2.5427 | 5.0854 | 24.739 |

The variation of mean wind speed with Weibull power density and Rayleigh power density are showed in Fig. 9 and in Fig. 10 with respect to years, respectively. The mean wind velocity is determined as 2.93 m/s for Weibull distribution and 2.64 m/s for Rayleigh distribution. In the Weibull distribution, the highest power density is 41.99W/m² in 2016 and the lowest power density is 17.87 W/m² in 2014 and the mean power density is 29.15 W/m². In the Rayleigh distribution, the highest and the lowest power density is determined as 26.20 W/m² in 2016 and 11.95 W/m² in 2014, respectively, and but also the mean power density is obtained as 22.29 W/m².

**Figure 9.** Yearly mean power density and wind speed according to Weibull distribution

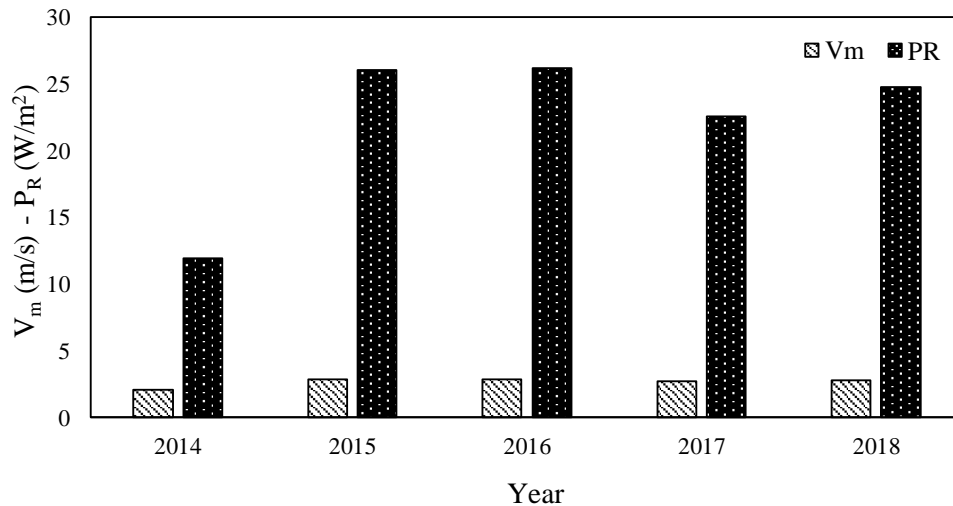


Figure 10. Yearly mean power density and wind speed according to Rayleigh distribution

5. Conclusion

The wind characteristics of Diyarbakır were statistically analyzed. Wind speed data were obtained for five years (2014-2018). Probability density distributions and power density distributions were obtained from time series data and distribution parameters were calculated. Two probability density functions were added to the wind speeds measured on a monthly and yearly basis. Based on the Weibull and Rayleigh models, the wind energy potential of Diyarbakır was investigated. The results can be summarized as the following:

1) Within five years, the Weibull distribution provides a better estimate of wind power potential density than the Rayleigh distribution. This is seen from the results of the correlation coefficient.

2) The Weibull model is generally better in fitting the measured yearly probability density distributions than the Rayleigh model, to the statistical criteria such as R^2 , RMSE and χ^2 . Therefore, it was concluded that it would be better to use the Weibull distribution in the analysis of wind data of Diyarbakır.

3) The values of the shape parameter (k) and scale parameter (c) at Diyarbakır were examined. The yearly mean values of k and c for Weibull distribution were determined as 2.47 and 3.27 m/s over a five year period of 2014-2018. The yearly mean c value for Rayleigh distribution was found 3.39 m/s.

4) It is indicated by the mean value of wind speed and energy intensity measured at the location that economical electricity production is not provided from wind power by the current technology and that the measurements need to be assessed in the long term in line with the technological developments and reduction in the cost of turbines. In conclusion, average monthly power and annual average power densities in Diyarbakır are not appropriate directly to the network support with wind energy systems.

Nomenclature

A : Blade sweep area (m^2)

c : Weibull scale parameter (m/s)

$f(v)$: Probability density function

ff : Frequency of occurrence of each speed class

$F(v)$: Cumulative distribution function

k : Weibull shape parameter

n : Number of wind speed classes

N : Number of hours in the period of time considered, number of observations

P : Power density (W/m^2)

$RMSE$: Root mean square error

R^2 : Correlation coefficient

V : Wind speed (m/s)

x_i : i th measured value

y_i : i th calculated value

z_i : mean value of the experimental data

Subscripts

m : mean

max : maximum

mod : largest frequency

R : Rayleigh

W : Weibull

References

- [1] Kaplan, Y. A. "Evaluation of Wind Energy in Osmaniye Region Using Rayleigh and Weibull Distributions", Süleyman Demirel University, Journal of Natural and Applied Sciences Volume 20, Issue 1, 2016, 62-71
- [2] Karadenizli A, Eker M .K., "Determination of Weibull function parameters by using 6 different methods by using the data of Balıkesir-Balya meteorological station", Dokuz Eylül University Faculty of Engineering Science and Engineering Journal, Volume 17, Issue 3, 2015, s.163-175
- [3] Hepbasli A, Ozgener O. "A review on the development of wind energy in Turkey". Renewable & Sustainable Energy Reviews 2004; 8(3): 257-276.
- [4] Işık, E., İnallı, M., Celik, E. "Approaches to Calculate the Heating and Cooling Degree Day Values: The Case of Provinces in Turkey", Arabian Journal for Science and Engineering, 2019, 1-17
- [5] Işık, E., İnallı, M. "Artificial Neural Networks and Adaptative Neuro-Fuzzy Inference Systems Approaches to Forecast the Meteorological Data for HVAC: The Case of Cities for Turkey", Energy, 2018, 154, 7-16

- [6] Kentli F., and Yılmaz M. "Obtaining the optimum efficiency electrical energy under Diyarbakir conditions using solar tracking system involving PV panel." *Energy Education Science and Technology Part A* 30 (2012): 613-620.
- [7] Yılmaz, M., and Kentli F. "Increasing of electrical energy with solar tracking system at the region which has Turkey's most solar energy potential." *Journal of Clean Energy Technologies* 3.4 (2015): 287-290.
- [8] Yılmaz M. "Real Measure of a Transmission Line Data with Load Fore-cast Model for The Future." *Balkan Journal of Electrical and Computer Engineering* 6.2: 73-77.
- [9] Akkılıç K., Ocak Y.S. and Yılmaz M. "Analysing enhancement of electricity generating capacity with solar tracking system of the most sunning region of Turkey." *Journal of Clean Energy Technologies* 3.4 (2015): 291-295.
- [10] Akpınar E. K, Balpetek N., "Statistical analysis of wind energy potential of Elazığ province according to Weibull and Rayleigh distributions", *Journal of the Faculty of Engineering and Architecture of Gazi University* 34:1 (2019) 569-580
- [11] Turksoy F. "Investigation of wind power potential at Bozcaada, Turkey". *Renewable Energy*, 6(8), 917-923, 1995.
- [12] Tolun S, Menten S, Aslan Z, Yukselen MA. "The wind energy potential of Gokceada in the northern Aegean sea". *Renewable Energy*, 6(7), 679-685, 1995.
- [13] Eskin N, Artar H, Tolun S. "Wind energy potential of Gokceada Island in Turkey". *Renewable & Sustainable Energy Reviews*, 12(3), 839-851, 2008.
- [14] Incecik S, Erdogmus F. "An investigation of the wind power potential on the western coast of Anatolia". *Renewable Energy*, 6(7), 863-865, 1995.
- [15] Sen Z, Sahin AD. "Regional assessment of wind power in western Turkey by the cumulative semivariogram method". *Renewable Energy*, 12(2), 169-177, 1997.
- [16] Durak M, Sen Z. "Wind power potential in Turkey and Akhisar case study". *Renewable Energy*, 25(3), 463-472, 2002.
- [17] Karsli VM, Gecit C. "An investigation on wind power potential of Nurdagi-Gaziantep, Turkey". *Renewable Energy*, 28(5), 823-830, 2003.
- [18] Bilgili M, Sahin B, Kahraman A. "Wind energy potential in Antakya and Iskenderun Regions, Turkey". *Renewable Energy*, 29(10), 1733-1745, 2004.

- [19] Akpınar E.K. “A statistical investigation of wind energy potential”. *Energy Source Part A*, 28(9), 807-820, 2006.
- [20] Gökçek M, Bayülken A, Bekdemir S. “Investigation of wind characteristics and wind energy potential in Kırklareli, Turkey”. *Renewable Energy*, 32(10), 1739-1752, 2007.
- [21] Ucar A, Balo F. “A seasonal analysis of wind turbine characteristics and wind power potential in Manisa, Turkey”. *International Journal of Green Energy*, 5(6), 466-479, 2008.
- [22] Gungör A, Eskin N. “The characteristics that define wind as an energy source”. *Energy Source Part A*, 30(9), 842-855, 2008.
- [23] Şahin B, Bilgili, M. “Wind characteristics and energy potential in Belen-Hatay, Turkey”. *International Journal of Green Energy*, 6(2), 157-172, 2009.
- [24] Ucar A, Balo, F. “Investigation of wind characteristics and assessment of wind-generation potentiality in Uludağ-Bursa, Turkey”. *Applied Energy*, 86(3), 333-339, 2009.
- [25] İmal M., Şekkelı M., Yıldız C. “Kahramanmaraş Sütçü İmam University Wind energy potential research and evaluation in main campus”, *KSU Journal of Engineering Sciences*, Volume 15, Issue. 2, 2012.
- [26] Balpetek N., “Use of Weibull and Rayleigh distributions to investigate the potential of wind energy”, Fırat University, Master Thesis, Elazığ, 2017.

CALCULATING ENERGY-INDUCED CARBON FOOTPRINT: BATMAN UNIVERSITY CASE

Ali Serkan AVCI¹, Hakan KARAKAYA^{2}*


This study determined the energy-induced carbon footprint arising from energy consumption in Batman University. It is important for universities to do acts toward control the greenhouse gas emission based on energy consumption while performing activities. Therefore, there is need to know the components of carbon footprint. Electric energy, natural gas energy, and various oils as the energy consumption components in these institutions were scrutinized. Petrol, diesel fuel, and fuel oil were utilized as types of oil. It is seen that the component which considerably specifies the carbon footprint is 3.161.238 ton CO₂ value and electric energy. Natural gas and fuel oil use contribute to carbon footprint at high ratios in winter months especially arising from heating. 361 ton CO₂ based on natural gas use and 1.256.445 ton CO₂ based on fuel oil use are other components which specify the carbon footprint. As a result, the primary carbon footprint for Batman University was determined by IPCC Methodology and Tier 1 approach; it is 3.162.855,445 ton CO₂ for 2017.


Keywords: *Carbon footprint, Global climate change, Tier approach*

1. Introduction

Greenhouse gas emission and environmental issues have emerged with the development of technology and increasing urbanization and energy consumption. Climate change based on global warming as the result of environmental issues and greenhouse gas emissions is a severe threat for our country and the world. Sustainable development, green axis growth, and environment-friendly policies become crucial in our country as well. In this regard, it is expected from organizations and people to decrease their carbon emission and increase environmental conscience.

It is observed when the literature relating to Carbon Footprint is analyzed to increase the sustainable and ecologic awareness that studies in recent years have gradually increased. Özlem reviewed some of the European countries' approaches based on power generation and consumption about carbon footprint [1]. Toröz analyzed methodology choices, calculations and results in enterprises in our

¹ Department of Energy Systems Engineering, University of Batman, Batman, Turkey, (aliserkan.avci@batman.edu.tr),
 <https://orcid.org/0000-0002-0761-8642>

² Department of Mechanical Engineering, University of Batman, Batman, Turkey, (hakan.karakaya@batman.edu.tr)
 <https://orcid.org/0000-0001-9242-6233>

country, the world and many European countries whose approaches on carbon footprint are different [2]. Yaka determined the carbon footprint of Health Services Vocational High School of Akdeniz University [3]. Ünalđı analyzed green marketing and carbon footprint concepts in detail [4]. Tan et al., evaluated the 30-years background of the transition process of universities in China to green and sustainable campus application [5]. Moreover, Li et al., measured the carbon footprint of students at Shanghai University in China [6].

Sangwan et al., [7] determined carbon footprint in Pilani campus of India. For their research results, indirect emissions have a 99% contribution to the footprint. Gu et al., found total energy footprint, carbon footprint and water footprint in Keele University in England [8]. They developed a conceptual correlation based on the combination of different environmental footprints to evaluate how hydrologic cycle, energy resources, climate with operations and food supply interact with each other. Ozawa-Meida et al., conducted a carbon footprint study based on consumption for a university in England [9]. Bello et al., analyzed the effects of hydroelectric consumption in Malaysia on the environment within four different frameworks as ecologic footprint, carbon footprint, water footprint, and CO₂ emission [10]. Utaraskul evaluated the carbon footprint of 35 students in Rajabhat university based on three criteria. Related criteria are food consumption and energy consumption by using electrical appliances [11].

In this study, it was aimed to point out global climate change and environmental awareness by computing the carbon footprint of Batman University that is one of the institutions that produce science. Carbon footprint shows the amount of carbon dioxide and other greenhouse gas emissions that are produced as the result of daily activities. The main effects on carbon footprints include population, economic output and energy and carbon density of economy. It is significantly associated with not only the energy consumption of corporate sectors but also the consumption of industry by the increase in energy consumption. Prevalence of energy-intensive devices in houses and job environment considerably increased energy consumption. Space heating and cooling systems in buildings to provide better comfort zones increase the energy consumption in the same way.

2. Carbon Footprint and Sustainability

‘‘Sustainable’’ and ‘‘ecologic’’ concepts enter into our daily life by increasing the environmental issues. ‘‘Sustainability’’ concept that first emerged in the international area in 1970 is defined as being provided ecological balance and protected the environment. The issue of ‘‘effect of human activities on environment’’ was discussed in Stockholm Conference in Switzerland in 1972; damages of related activities were highlighted [12]. It was decided to reduce the greenhouse gas emission till 2012 in Kyoto Protocol which was signed by 189 countries in 1997 Greenhouse gas emission [13]. Sustainability is a broad concept which prioritizes conservation and sustainability of natural habitat and inholds the social and economic dimensions at the same time. Sustainable development will actualize when environmental, economic and social sustainability materialize together [14].

Ecological footprint means the size of biologically fertile soil or water area in global hectares. This fertile soil or water is required to destroy the waste and reproduce the resources consumed by a community or activity via available technology and resource management [15]. The biggest share belongs to carbon footprint among the Ecological Footprint components in Turkey in 2007 [16].

Carbon footprint is composed of two parts as the primary and secondary carbon footprint. The primary carbon footprint (direct carbon footprint) is defined as the direct measurement of CO₂ emissions which arise as the result of firing fossil fuels that are used for energy consumption and transportation.

The secondary one (indirect carbon footprint) is the measurement of CO₂ emissions that arise during the whole life cycle from being produced and consumed all the commodities. Carbon footprint is a crucial indicator to reveal the effects of greenhouse gas emissions on the environment and minimize those related effects.

About the Carbon Footprint Change of Turkey and the World countries, G20 countries which meet approximately 85% of the world economy and 80% of the world trade is considered. The carbon footprint of 19 state part of G20 and all the EU countries were evaluated for the period between 1990 and 2016. Figure 1 and 2 shows the carbon footprint values belong to related years on the website of World Carbon Atlas. While China, America, and India were in the leading position for carbon footprint values in 2016; Italy, France, and Argentina were in the last ranks. While America was the leading country in 1990, China reached the top in 2016. Carbon footprint values of Turkey increased approximately 2,5 times from 1990 to 2016 [17].

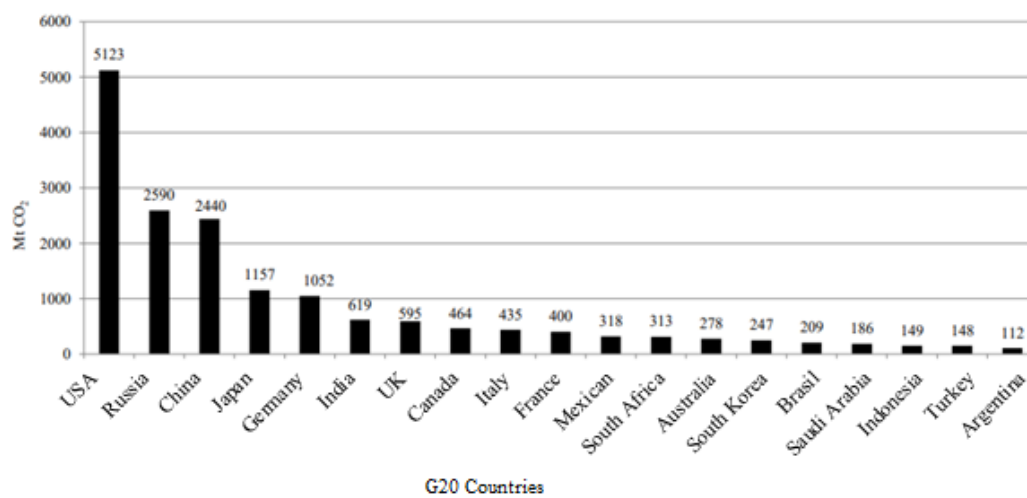


Figure 1. Carbon footprint values of G20 countries in 1990 (Mt CO₂) [18]

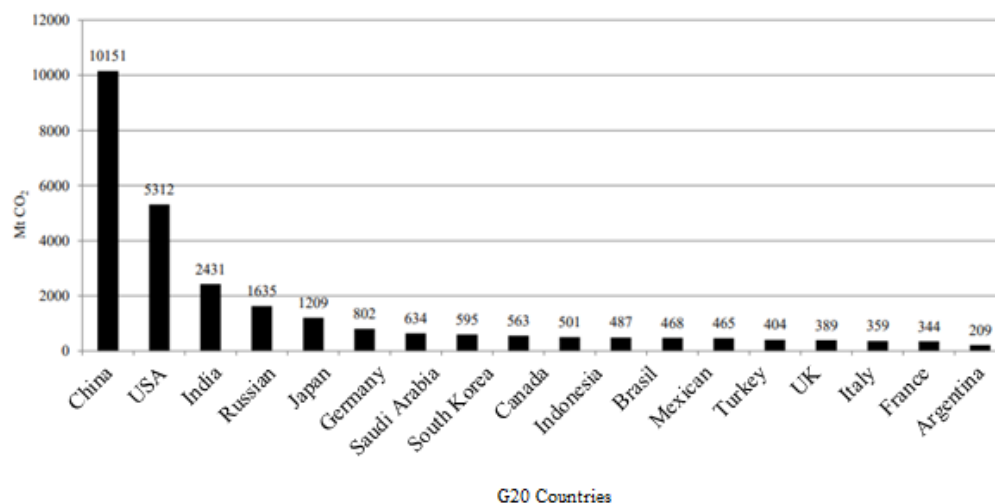


Figure 2. Carbon footprint values of G20 countries in 2016 (Mt CO₂) [18]

Although there has been a 3 times increase in carbon footprint value of Turkey in the last 15 years, there are two main reasons for us to be at last ranks. One of the reasons is that while developed countries increased energy efficiency in other sectors which generate the emission, the yield in these

sectors in Turkey has not increased as of yet. In other words, the share of carbon footprint in total emissions is relatively low in the transportation sector because of the high CO₂ emission. The second reason is that while the mobility (number of trips per person and length of the journey) is more in developed countries, the same mobility is relatively low in developing countries such as Turkey [19].

3. Method

The primary carbon footprint was computed by the IPCC calculated methodology (Tier 1 approach) in this study. In this regard, carbon footprint arising from heating, transportation and electricity consumption of University was computed.

Since the carbon emission based on energy consumption of university was computed in this study, the information in energy title was utilized. 2017 Data of all departments of Batman University were analyzed. Since carbon dioxide emission is directly associated with firing the oil, it can be exactly computed. Firing conditions, technology, emission standards, and oil characteristics need to be known to compute other greenhouse gases. IPCC methodology categorized emission calculation methods at 3 different levels which are accepted as Tier [20].

Tier 1 uses the assumed emission factor in calculation; it does not consider the factors in the region where the activity is found. Resource category of each of the gas emissions and emission factor peculiar to the oil is required in the Tier 2 approach. These emission factors are specified peculiar to this country because of differences in types of oil, burning technology, working conditions, control technology, care quality and age of the equipment used for firing oil. Since the emission factor is intrinsic to country, variability and carbon dioxide emissions need to be calculated in a proper way. Tier 3 approach uses technology variable as the base and includes firing process, properties of oil and other factors that can affect calculation results [20, 21]. This study gave the calculation method relating to the Tier 1 approach in detail; CO₂ emission that has the biggest share in greenhouse gases was computed as well.

Amount of fuel consumption is determined in the calculation of carbon dioxide emissions. Gasoline, diesel, LPG, coal, natural gas and electricity consumption amounts were obtained from the official records of University. IPCC carbon dioxide emission factor, 0,584 ton/mWh that was found in master's thesis of Toröz was used to calculate carbon dioxide emission based on the electric energy [2, 20]. Energy content is computed by multiplying consumption values of fuels by transformed value in IPCC guide. Transformed values are the values in IPCC 2006 guide and the Regulation on Monitoring of Greenhouse Gas Emissions that was published in 22.07.2014 dated and 29068 numbered Official Gazette. The table shows the related values.

Table 1. Net Calorific Value of Fuels

| Fuel Type | Net Calorific Value (Tj/Gg) |
|-------------------------------|-----------------------------|
| Gasoline | 44,3 |
| Diesel | 43,0 |
| LPG (Liquefied Petroleum Gas) | 47,3 |
| Lignite Coal | 11,9 |
| Natural gas | 48,0 |

$$\text{Energy Consumption (TJ)} = \text{Fuel Consumption (t)} \times \text{Net Calorific Value (TJ/Gg)}$$

At this stage, carbon emission factors in IPCC guide for each of fuel group were selected to calculate the total carbon content in the fuel. Amount of carbon content is found by multiplying carbon emission factor by the energy content value that is computed in the previous step [20].

Table 2. Emission Factor of Fuels

| Fuel Type | Emission Factor (t C/Tj) |
|-------------------------------|--------------------------|
| Gasoline | 18,9 |
| Diesel | 20,2 |
| LPG (Liquefied Petroleum Gas) | 17,2 |
| Lignite Coal | 27,6 |
| Natural gas | 15,3 |

$$\text{Carbon Content (t C)} = \text{Carbon Emission Factor (t C/TJ)} \times \text{Energy Consumption (TJ)}$$

Unoxidized carbon amount is found during firing; carbon value that completely fires is calculated. Following oxidation percentages (combustion efficiency) are specified by IPCC; 0,99 for petroleum products, 0,995 for gaseous fuels; 0,98 for coal products. The amount of oxidized carbon is computed by multiplying the carbon content by these related values.

Table 3. Oxidation Ratio of Fuels

| Fuel Type | Oxidation Rate |
|-------------------------------|----------------|
| Gasoline | 0,99 |
| Diesel | 0,99 |
| LPG (Liquefied Petroleum Gas) | 0,99 |
| Lignite Coal | 0,98 |
| Natural gas | 0,995 |

$$\text{Carbon Emission (Gg C)} = \text{Carbon Content (Gg C)} \times \text{Carbon Oxidation Rate}$$

Net carbon value that is found by the proportion of the molecular weight of CO₂ to the molecular weight of carbon is turned into CO₂ form. At this stage, CO₂ emission value is found by multiplying the previous value by 44/12 that is the proportion of the molecular weight of CO₂ to the molecular weight of carbon [20].

$$\text{CO}_2 \text{ Emission (Gg CO}_2) = \text{Carbon emission (Gg C)} \times (44/12)$$

4. Findings

Data relating to electricity, gasoline, diesel, natural gas, and Fuel Oil consumption were received from university to determine the primary carbon footprint of University for 2017. Calculations were performed in line with IPCC methodology Tier 1 approach that can be seen in Method chapter. Table 4 shows the related calculations.

Table 4. Calculation of Carbon Footprint in Batman University

| Energy Type | Consumption Amount (2017 Year) | Consumption Amount (Ton) | Net Value (Tj / Gg) | Calorie | Carbon Emission Factor (tC / TJ) | Carbon Oxidation Rate | Ton CO ₂ |
|--------------|--------------------------------|--------------------------|---------------------|---------|----------------------------------|-----------------------|---------------------|
| Gasoline | 1091 litre | 0,81 | 44,3 | | 18,9 | 0,99 | 2,461 |
| Diesel | 63845 litre | 53,6 | 43 | | 20,2 | 0,99 | 170,164 |
| Natural gas | 169303 m ³ | 135,44 | 48 | | 15,3 | 0,995 | 361 |
| Fuel Oil | 350260 kg | 350,26 | 40,4 | | 21,1 | 0,99 | 1083,82 |
| Electricity | 5413079 KWh | | | | | | 3161238 |
| Total | | | | | | | 3162855,445 |

Primary carbon footprint value of Batman University was found as 3.162.855,445 ton CO₂ by the help of IPCC Methodology and Tier 1 approach. Electric energy is 3.161.238 ton CO₂. This value is 99% of the total carbon footprint within the campus. Moreover, 0,03% of total carbon footprint results from 361 ton CO₂ natural gas use and 1.256.445 ton CO₂ fuel oil consumption.

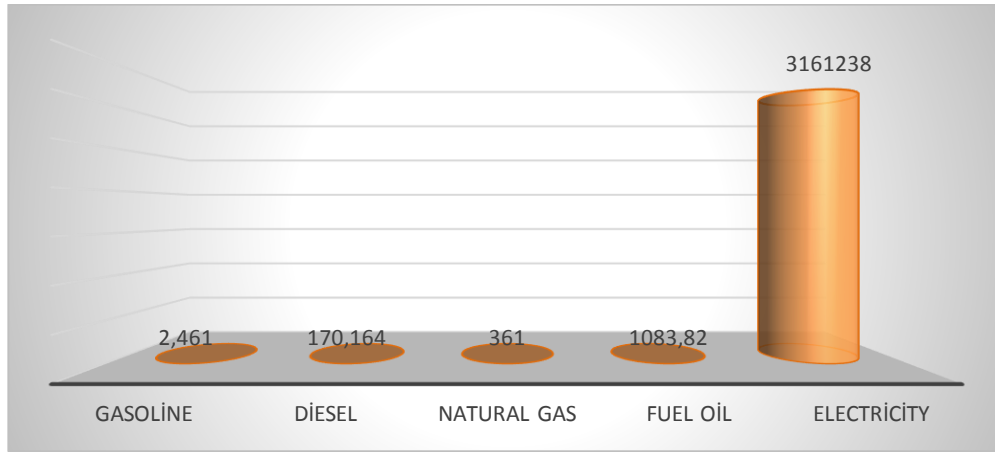


Figure 3. Batman University's Carbon Footprint (Ton CO₂)

5. Conclusion

Need for energy gradually increases by industrialization and increasing the world population. This overconsumption brings along global climate change and increasing health risks. Due to these reasons, countries have started to reevaluate energy models. They should head for renewable energy resources that are non-depletable, clean and confidential. It is seen that renewable energy provides remarkable environmental advantages regarding greenhouse gas emissions and other classical atmosphere pollutants in comparison to classical energy systems. Turkey is extremely lucked in terms of renewable energy potential. Therefore, it is important to be effectively used available clean energy resources to avoid both environmental, social and economic problems. This study was conducted to create awareness in terms of sustainability and ecological. Greenhouse gas emissions based on energy consumption was emphasized. The primary carbon footprint is 3.162.855,445 ton CO₂ by IPCC Methodology and Tier 1 approach for 2017 for Batman University. 99% of this value originates in electric energy consumption. There is a need for establishing renewable power plants, notably solar power plants to meet increasing electric energy need within campus and change available energy with clean energy resource.

References

- [1] Özlem, B., (2013). Seçilen Bir Kağıt Fabrikasında Karbon Ayak İzinin Belirlenmesi, Thesis, İstanbul Teknik University, 149s.
- [2] Toröz, A., (2015). Gemi Kaynaklı Atıkları Alan Bir Atık Kabul Tesisinde Karbon Ayak İzinin Belirlenmesi, Thesis, İstanbul Teknik University, 135s.
- [3] Yaka, İ. et al., (2015). Akdeniz Üniversitesi Sağlık Hizmetleri Meslek Yüksek Okulu Karbon Ayak İzinin Tespiti, Makine Teknolojileri Elektronik Dergisi ss. 37-45, Akdeniz University, Antalya

- [4] Ünalđı, G., (2016). Yeşil Pazarlamada Karbon Ayak İzi Kavramının Deęerlendirilmesi, Thesis, Hitit University, Çorum, 175s
- [5] Tan, H., Chen , S., Shi, Q., ve Wang, L., (2014). Development of green campus in China, Journal of Cleaner Production, 64, 646-653.
- [6] Li, X., Tan, H. ve Rackes, A., (2015). Carbon footprint analysis of student behavior for a sustainable university campus in China, Journal of Cleaner Production, 106, 97-108.
- [7] Sangwan, K. S., Bhakar, V., Arora, V., & Solanki, P. (2018). Measuring Carbon Footprint of an Indian University Using Life Cycle Assessment. Procedia CIRP, 69(1), 475-480.
- [8] Gu, Y., Wang, H., Xu, J., Wang, Y., Wang, X., Robinson, Z. P., & Zhi, X. (2019). Quantification of interlinked environmental footprints on a sustainable university campus: A nexus analysis perspective. Applied Energy, 246, 65-76.
- [9] Ozawa-Meida, L., Brockway, P., Letten, K., Davies, J., & Fleming, P. (2013). Measuring carbon performance in a UK University through a consumption-based carbon footprint: De Montfort University case study. Journal of Cleaner Production, 56, 185-198.
- [10] Bello, M. O., Solarin, S. A., & Yen, Y. Y. (2018). The impact of electricity consumption on CO 2 emission, carbon footprint, water footprint and ecological footprint: the role of hydropower in an emerging economy. Journal of environmental management, 219, 218-230.
- [11] Utaraskul, T. (2015). Carbon footprint of environmental science students in Suan Sunandha Rajabhat University, Thailand. Procedia-Social and Behavioral Sciences, 197, 1156-1160.
- [12] Web 1, Ozon Tabakasını incelten maddelere dair Montreal Protokolü, (1990). Link: <http://iklim.cob.gov.tr/iklim/AnaSayfa/montrealptotokolu.aspx?sflang=tr>, Date of Access: 19.01.2018
- [13] Türkeş, M., İklim Deęişikliğiyle Savaşım, Kyoto Protokolü ve Türkiye, Mülkiye Dergisi, 32, 101-131, (2014).
- [14] Web 2, Engagement and the communication spectrum, (2017), Link: <http://www.stepstosustainability.com>, Date of Access: 20.01.2018.
- [15] Özsoy Erden, C. (2015). Düşük Karbon Ekonomisi ve Türkiye'nin Karbon Ayak İzi. Emek ve Toplum, 4, 199-215.
- [16] World Wide Fund for Nature(WWF)., 2012. Türkiye'nin Ekolojik Ayak İzi Raporu. 89s.
- [17] Bıyık Y, (2018) Isparta İlinde Karayolu Kaynaklı Karbon Ayak İzinin Hesaplanması, Süleyman Demirel University, Thesis.
- [18] Global Carbon Atlas, 2018. CO₂ Emissions. Date of Access: 10.04.2018. <http://www.globalcarbonatlas.org/en/content/welcome-carbon-atlas>
- [19] Çevre ve Şehircilik Bakanlığı (ÇŞB), 2011. Türkiye Cumhuriyeti İklim Deęişikliği Eylem Planı 2011-2020. Ankara.
- [20] Binboęa, G., and Aylin, Ü. N. A. L. (2018). Sürdürülebilirlik Ekseninde Manisa Celal Bayar Üniversitesi'nin Karbon Ayak İzinin Hesaplanmasına Yönelik Bir Araştırma. Uluslararası İktisadi ve İdari İncelemeler Dergisi, (21), 187-202.
- [21] Turanlı, A.M. (2015). Estimation of Carbon Footprint: A Case Study for Middle East Technical University, Master of Science. (Yayımlanmamış Yüksek Lisans Tezi). Natural and Applied Sciences of Middle East Technical University, Ankara.